UNIVERSIDADE D
COIMBRA

Giorgio Caliman Canezin

A nRPC-4D Neutron Detector Concept with Timing and Three-Dimensional Position Readout Capability

Dissertação no âmbito do Mestrado em Física, ramo Física Nuclear e de Partículas orientada pelo Doutor Luís Margato, Doutor Andrey Morozov e Professor Doutor Ricardo Gonçalo apresentada ao Departamento de Física da Faculdade de Ciências e Tecnologia da Universidade de Coimbra.

Setembro de 2023

UNIVERSIDADE D
COIMBRA

A nRPC-4D Neutron Detector Concept With Timing and Three-Dimensional Position Readout Capability

Supervised by:

PhD Luís Margato

PhD Andrey Morozov

PhD Ricardo Gonçalo

Dissertation submitted in fulfillment for the degree of Master of Science in Physics.

Acknowledgments

I would like to thank my supervisors, Doctor Luís Margato, Doctor Andrey Morozov and Doctor Ricardo Gonçalo, for their guidance throughout my thesis, for their friendliness, for their availability and for the opportunities and incentives that they have passed my way.

I would like to thank LIP - Laboratory of Instrumentation and Experimental Particle Physics for providing me with the working conditions necessary to carry out this dissertation.

I am thankful to FCT for the Research Student Fellowship through the project EXPL/FIS-NUC/0538/2021 supported by Portuguese national funds OE and FCT-Portugal.

The remarkable support and efforts of Professor Florian PIEGSA, from the University of Bern, Switzerland, who made it possible to perform the neutron tests reported in this thesis are kindly acknowledged. I also would like to acknowledge the Swiss spallation neutron source SINQ, Paul Scherrer Institute, Villigen, Switzerland, for providing neutron beam time for testing the detector prototype.

I am thankful to all the great friends I made throughout these years living in Portugal, nothing would be the same without their kind hospitality.

I would like to thank my parents, Margareth and Jorge, who have always believed in my potential, motivated me and wished for my success. I would also like to thank my girlfriend Maria Inês for the company and support she gave me.

Abstract

Neutron scattering techniques play a critical role in advancing scientific knowledge in physics, chemistry and biology as well as boosting technological innovations across medical and material research, homeland security and cultural heritage conservation. One common need for all neutron scattering science applications is a detector capable of detecting the neutrons that are transmitted through, reflected by or scattered in the sample. For a long period of time, ^{3}He-based detectors were the gold standard in neutron scattering science. However, with the ^{3}He supply crisis starting in 2001 due to the United States' vast use of neutron detectors in homeland security, the demand for ^{3}He quickly rose, until surpassing the supply in 2009. The resulting high cost of ^{3}He made the construction of large-area detectors based on this isotope economically not feasible. To reduce the dependency on ^{3}He in neutron scattering science, attention was redirected to finding alternative detection technologies.

A novel concept of a thermal/cold neutron detector based on the ^{10}B-RPC technology, called the nRPC-4D, is presented in this dissertation thesis. The big goal of the project ongoing in LIP is to demonstrate that an nRPC-4D detector can provide a four-dimension readout capability (XYZ and time) of the neutron events with submillimetre positional and ns-scale timing resolution, making it a competitive alternative compared with the performance of the current state-of-the-art neutron detectors. Aligned with this goal, the main objectives of the work on this thesis were to construct such a detector prototype and perform its characterisation with thermal neutrons. My main efforts during this work consisted in the assembly of an nRPC-4D detector prototype, the development of data processing tools, and the subsequent data analysis of the experimental results.

A detector prototype was assembled, tested and shipped to the Paul Scherrer Institute (PSI) for characterisation at the neutron beamline. The counting rates measured from each module matched well the Monte Carlo simulation results, demonstrating a good prediction power of the developed simulation model. The detector was able to accurately identify the XY (across the beam) and Z (along the beam) position of the neutron events. The precision of the Z coordinate determination is significantly improved compared to the previous generation of the ^{10}B-RPC

detectors. It was also demonstrated that the detector is capable to reliably measure the neutron time of flight by recording the neutron wavelength spectrum at the beamline and comparing it with the known data. These experimental results demonstrate that the developed detector concept is a strong candidate to be applied in designing the next generation instruments for TOF neutron diffraction, macromolecular neutron crystallography, and energy-resolved neutron imaging.

Keywords

- Thermal Neutron Detectors, Resistive Plate Chambers, Boron-10 converters, Neutron Scattering Science, European Spallation Source

Resumo

As técnicas de dispersão de neutrões desempenham um papel fundamental no avanço do conhecimento científico em áreas tão diversas como a física, química e biologia, bem como, no impulsionar a inovação tecnológica na medicina, no desenvolvimento de novos materiais, na segurança interna e na conservação do património cultural. A viabilidade destas técnicas, acessíveis apenas em instalações de neutrões de grande escala, só é possível através da utilização de detectores capazes de detectar os neutrões transmitidos, refletidos ou dispersos pelas amostras. Durante um longo período de tempo, os detectores usados para aplicações na ciência de dispersão de nêutrons eram baseados na tecnologia de detecção do Hélio-3. Com a crise de fornecimento de Hélio-3 iniciada em 2001, e motivada pelo uso massivo deste isótopo na construção de detectores de neutrões para fins de segurança interna, nos Estados Unidos da América, a procura ultrapassa a oferta por volta de 2009. O elevado custo do Hélio-3 tornou economicamente inviável a construção de detectores de grandes áreas baseados neste isótopo. De modo a reduzir a dependência do Hélio-3 em aplicações na ciência da dispersão de neutrões, têm vindo a ser envidados esforços no sentido de desenvolver tecnologias de detecção alternativas tendo em vista a sua substituição.

Nesta dissertação é apresentado um novo conceito de detetor de neutrões térmicos/frios baseado na tecnologia ^{10}B-RPC, e denominado de nRPC-4D. O principal objetivo do projeto em curso no LIP, é demonstrar que um detetor nRPC-4D tem capacidade de detectar e realizar a leitura de eventos de neutrões a quatro dimensões (XYZ e tempo), e com resolução posicional submilimétrica e temporal da ordem do ns, fazendo deste tipo de detector uma alternativa com um desempenho competitivo em comparação aos actuais detectores de neutrões de última geração. Integrado neste projecto, os principais objectivos do trabalho desta tese de dissertação foram, o desenvolvimento e construção de um protótipo de detetor e a sua caracterização em feixe de neutrões com vista à prova de conceito. A minha principal contribuição para este projecto consistiu na participação da construção de um protótipo de um detector nRPC-4D, no desenvolvimento de ferramentas de processamento de dados e na subsequente análise dos resultados experimentais obtidos nos testes em feixe de neutrões.

Depois de construído, e testado, enviou-se o protótipo para o Paul Scherrer Institute para

caracterização em feixe de neutrões. Resultados experimentais dos testes demonstram que, as taxas de contagem em cada módulo de detecção que constituem o detector nRPC-4D, exibem boa concordância com os resultados da simulação de Monte Carlo, demonstrando a boa capacidade de previsão do modelo de simulação desenvolvido. É ainda demonstrada a capacidade do detector para identificar com precisão a posição XY e Z (direção do feixe) dos eventos de neutrões. A precisão com que é determinada a coordenada Z foi significativamente melhorada relativamente à anterior geração de detectores baseados nas ^{10}B-RPCs. Também é demonstrada a capacidade do detector para medir, de forma fiável, o tempo de voo dos neutrões, e com isso, determinar o seu espectro de comprimento de onda do feixe. Estes resultados experimentais demonstram que o conceito de detector desenvolvido se apresenta como um forte candidato a ser aplicado na concepção de detectores para a próxima geração de instrumentos para difração de neutrões em TOF, cristalografia macromolecular com neutrões, e imagiologia de neutrões resolvida em energia.

Palavras-Chave

- Detectores de Neutrões Térmicos, Câmara de Placas Resistivas, Conversor Boron-10, Ciência de Disperção de Neutrões, European Spallation Source

Table of contents

List of Tables

List of Figures

Abreviations

RPC Resistive Plate Chamber

TOF Time-Of-Flight

ESS European Spallation Source

ILL Institut Laue–Langevin

PSI Paul Scherrer Institute

BOA Beamline for Neutron Optics and Other Approaches

LIP Laboratory of Instrumentation and Experimental Particle Physics

HV High Voltage

UV UltraViolet

MIP Minimum Ionising Particle

DAQ Data Acquisition System

FEE Front End Electronics

PCB Printed Circuit Board

FPCB Flexible Printed Circuit Board

ACF Anisotropic Conductive Film

Chapter 1

Introduction

1.1 Overview and Motivation

Due to their unique set of properties, such as being highly penetrating, non-destructive, having a wavelength similar to atomic distances and possessing magnetic moment, neutrons play a fundamental role as probing agents in the study of the structure and properties of matter across a wide range of scientific fields, in what is known as neutron scattering science. Neutron scattering techniques like spectroscopy, diffraction, reflectometry, small angle scattering and imaging allow us to explore and understand the fundamental and applied aspects of matter in its various forms and applications. They play a critical role in advancing scientific knowledge in physics, chemistry and biology as well as boosting technological innovations across medical and material research, homeland security and cultural heritage conservation [1]. One common need for all neutron scattering science applications is a detector capable of detecting the neutrons that are transmitted through, reflected by or scattered in the sample.

Large-scale neutron science facilities, established worldwide, such as the Institut Laue-Langevin (ILL) in France, Neutron and Muon Source (ISIS) in England, Research Neutron Source Heinz Maier-Leibnitz (FRM II) in Germany, Paul Scherr Institut (PSI) in Switzerland and the Spallation Neutron Source (SNS) in the United States of America, provide researchers access to neutron beams and state-of-the-art instruments. Currently, new neutron science facilities, such as the European Spallation Source (ESS) [2] in Sweden, are continuously pushing for improved flux rates, resulting in the need for more advanced instrument performance, such as increased count rate capability, better timing precision. Additionally, the existing facilities, such as the ones referred above, also require a continuous upgrade to their set of instruments [3][4].

As neutron detectors are crucial components in neutron scattering science, researchers strive

to develop more effective and efficient neutron detection methods. However, this is a challenging task. The detection of neutrons presents two primary challenges. The first is that neutrons do not produce direct ionisation or generation of light, which are essential processes in most radiation detectors. The second challenge arises from the fact that thermal or cold neutrons do not generate observable collisional recoil. As a result, neutrons must be detected indirectly via a nuclear reaction that can generate ionising particles. Only a few isotopes have a significant cross section for these reactions, and the ones with the most practical interest for detection applications are ^{3}He, ^{10}B, ^{6}Li and ^{155,157}Gd.

^{3}He has one of the highest neutron absorption cross sections and can operate at high pressure, making it an excellent neutron converter for robust, efficient, and long-lived neutron detectors [4]. For a long period of time, ^{3}He-based detectors were the gold standard in neutron scattering science. However, with the ^{3}He supply crisis starting in 2001 due to the United States vast use of ^{3}He-based neutrons detectors in homeland security, the demand for ^{3}He quickly rose, until surpassing the supply in 2009 [5]. The resulting high cost of ^{3}He made the construction of large-area detectors based on this isotope economically not feasible. To reduce the dependency on ^{3}He in neutron scattering science, attention was redirected to find alternative detection technologies.

During the last decade, the main three development lines were based on BF_3-filled detectors [6], neutron sensitive scintillation technology [7] and gaseous detectors with solid ^{10}B or gadolinium neutron converters [8][9]. BF_3 being in a gaseous form was seen as a direct replacement for ^{3}He. However, due to its toxicity and inability to operate at high pressures, research with BF_3 filled detectors was discontinued and even outlawed in European facilities [4].

Scintillation detectors typically use scintillators loaded with ^{6}Li that are either directly coupled to photosensors or connected through wavelength shifting fibres. Detectors with such scintillators can provide short decay times of about 70 ns and detection efficiencies of more than 50%. However, they have weak neutron/gamma discrimination, are difficult to scale to large areas while maintaining a spatial resolution of less than 1 mm and their cost per unit area is very high [10]. ZnS:Ag/^{6}LiF scintillators are commonly used at neutron facilities, but their long afterglow of around 100 us limits the count rate, and their spatial resolution is usually above 1 mm [7].

The gas-filled detectors use ^{10}B or ^{155,157}Gd solid converters and are implemented either in multi-wire chambers (MWPC) [11], Multi-Blade counters [12] or gas electron multipliers (GEM) [13][14]. MWPCs with B_4C converters can achieve good detection efficiency, however, they are limited in counting rate and the intrinsic spatial resolution is typically above 3 mm.

Multi-Grid detector is made of several layers of counter voxels with B_4C coating on the

inner side. The detection efficiency can reach 50%, however, the spatial resolution is quite low (2.5 cm FWHM), which is limited to the voxel size. GEMs with B_4C converter layers can offer high counting rates but the spatial resolution cannot reach the submillimetre scale [13]. GEMs with a single converter layer of natural Gd can offer a spatial resolution of about 1 mm, but the detection efficiency is low ($< 15\%$), and the sensitivity to gamma rays is extremely high ($> 10^{-3}$).

Although remarkable progress was achieved, the current state-of-the-art neutron detectors are still unable to meet the requirements set for modern instruments in neutron scattering science experiments planned for the European Spallation Source (ESS), the future spallation sources [3], the upgrade programs of the existing facilities and to replace ^{3}He without a loss in performance and a significant increase in costs [4].

Motivated by this, a group from LIP-Coimbra introduced the ^{10}B-RPC neutron detection technology to be an alternative to ^{3}He-filled position-sensitive detectors. The ^{10}B-RPCs combine hybrid double gap resistive plate chambers (RPC) lined with $^{10}B_4C$ neutron converters [15]. It was already experimentally demonstrated that a ^{10}B-RPC based detector can reach a detection efficiency of ≈62.1% for neutrons with λ=4.7 Å and a spatial resolution of ≈0.25 mm FWHM [16].

In order to meet the requirements for experiments that demand both position and timing readout, such as time-resolved neutron imaging [17], our group at LIP-Coimbra proposed a novel concept of a thermal/cold neutron detector based on the ^{10}B-RPC detection technology with four-dimension readout capability (XYZ and time), named nRPC-4D [18]. Based on the previous results with ^{10}B-RPCs and the intrinsic timing capabilities of RPCs, the detector has a potential to reach sub-millimeter spatial resolution, a detection efficiency higher than 50% for thermal neutrons, and time resolution down to the nanosecond scale.

1.2 Objectives

The work reported in this thesis was performed in the frame of the ongoing nRPC-4D project at the LIP laboratory in Coimbra. The main goal of this project is to develop a ^{10}B-RPC based detector concept for cold and thermal neutrons, which can simultaneously offer submillimetre spatial resolution, nanosecond scale time resolution, good detection efficiency ($> 50\%$), high counting rate ($> 10^5$ counts/cm^2/s) and low sensitivity to gamma rays ($< 10^{-5}$). This set of features is a requirement for the next generation time-of-flight (TOF) neutron diffraction/reflectometry and energy- and time-resolved neutron imaging instruments planned for large-scale neutron facilities, and in particular for the European Spallation Source (ESS).

The objectives of this master's thesis were to develop the nRPC-4D detector concept and construct a prototype, develop data processing tools, and the subsequent evaluation and analysis of the results of the experimental tests recently conducted on a neutron beam at the Swiss Spallation Neutron Source (SINQ) at PSI.

1.3 Thesis Structure

This document is structured into eight chapters.

- Chapter 2 (Interaction of Radiation with Matter) discusses the fundamental physics principles of the interaction of radiation (charged particles, gamma-rays and neutrons) with matter.
- Chapter 3 (Resistive Plate Chambers) presents an overview of the standard RPC design and its operational principles.
- Chapter 4 (The ^{10}B-RPC Technology) describes the basic concept of the ^{10}B-RPC thermal neutron detection technology that combines RPCs with $^{10}B_4C$ neutron converters.
- Chapter 5 (The nRPC-4D Detector Concept) presents a novel thermal neutron detector concept based on the ^{10}B-RPC technology with four-dimension readout capability (XYZ and time).
- Chapter 6 (The nRPC-4D Detector Prototype) reports on the construction of the first detector prototype based on the nRPC-4D concept.
- Chapter 7 (Prototype Tests on a Neutron Beamline) gives a detailed description of the experimental setup and the results of the tests performed at the SINQ neutron spallation source at PSI.
- Chapter 8 describes the main conclusions and gives an outlook for the future work.

1.4 My Personal Contribution

In this master thesis, my personal contributions to the project are presented in chapters 6 and 7. I have conducted the following work:

- Construction of the ^{10}B-RPC modules;
- Establishing connections between the pickup strips and cathodes to the front end electronics and the triggering boards and assembly of the detector prototype;

- Development of an algorithm which computes the mapping of the pickup strips depending on the number and positioning of the front-end electronic boards used in a particular experiment. I have also implemented this algorithm in the software framework developed in the group for analysis of the detector output;
- Development of an algorithm which classifies neutron events (neutron or background);
- I was responsible for the analysis of the experimental data acquired on the neutron beamlines at PSI.

The work in the frame of this project has resulted in the following publication in an international peer-reviewed journal:

- Timing resistive plate chambers for thermal neutron detection with 3D position sensitivity. Nuclear Instruments and Methods in Physics Research Section A: Accelerators, Spectrometers, Detectors and Associated Equipment, Volume 1052, 2023, 168267, ISSN 0168-9002, https://doi.org/10.1016/j.nima.2023.168267. L.M.S. Margato, **G. Canezin**, A. Morozov, A. Blanco, J. Saraiva, L. Lopes, P. Fonte.

The results obtained over the course of this thesis were also orally presented by me at the following national conference:

- A novel neutron detection technology based on timing RPCs. 5th Doctoral Congress in Engineering, Symposium on Engineering Physics, 2023. **G. Canezin**, L. Margato, A. Morozov, A. Blanco, J. Saraiva, L. Lopes, P. Fonte.

Chapter 2

Interaction of Radiation With Matter

The operation of any radiation detector is based on how the radiation to be detected interacts with the materials of the detector. Understanding the operation of a specific type of detector must thus rely on the fundamental principles of the interaction of radiation with matter. For neutron detectors, the most relevant interactions are with charged particles, gamma rays, and neutrons.

As a result of the electric charge carried by the particle, charged particles continuously interact through the coulomb force with the electrons present in any medium through which they pass. On the other hand, uncharged particles such as gamma rays and neutrons are not subjected to the coulomb force. These particles must first undergo an interaction that drastically alters their properties in a single encounter, resulting in the full or partial transfer of energy to the electrons/nuclei of the atoms or to the products of the triggered nuclear reaction.

2.1 Charged particles interaction

Energy loss by the particle and the deflection of the particle from its incident direction are two principal effects that influence the passage of charged particles through matter. These effects are mostly the result of the electromagnetic interactions with the atomic electrons of the material and scattering from nuclei. These reactions occur almost continuously in matter, and their cumulative result accounts for the principal effects observed.

2.1.1 Heavy charged particles

The interaction of heavy charged particles such as protons and α particles with matter is principally mediated by coulomb forces between their charge and the charge of the orbital electrons within the absorber atoms. Interactions with the nuclei are also possible, although they are usually negligible regarding the detector's response. Instead, charged particle detectors must rely on the results of interactions with atomic electrons, which are almost solely responsible for the energy loss of heavy charged particles in matter.

As a positively charged heavy particle enters the interacting medium, the electrons are attracted by the electromagnetic force as the incoming particle passes its vicinity. Depending on how close this encounter is, the interaction might be enough to raise the electron to a higher-lying shell of the atom of the medium (excitation) or completely eject the electron from the atom (ionisation). The energy transferred from the incoming particle to the electron results in a decrease in the particle's momentum.

The product of these encounters in the absorber are either excited atoms or electron-ion pairs. Each pair comprises a free electron and the corresponding positive ion of an absorber atom, from which the electron has been totally removed. The electron-ion pairs have a natural tendency to recombine to form neutral atoms, but in the case of gaseous detectors, this recombination is suppressed by applying an electric field so that the ion pairs may be used as the basis of the detector response.

The energy loss per unit length of a charged particle inside the absorbing material depends on the velocity and charge of the incoming particle and the target material's atomic number and electron density. This quantity is known as the stopping power or simply dE/dx, and it was first calculated by Bethe [19] using classical terms and later by Bloch and others using quantum mechanics [20]. The formula obtained is then

$$-\frac{dE}{dx} = \frac{4\pi e^4 z^2}{m_0 v^2} NB \tag{2.1}$$

$$B \equiv Z\left[\ln\frac{2m_0v^2}{I} - \ln\left(1-\frac{v^2}{c^2}\right) - \frac{v^2}{c^2}\right]$$

In these expressions, v and z are the velocity and charge of the primary particle, N and Z are the number density and the atomic number of the absorber atoms, m_0 is the electron rest mass, and e is the electronic charge. The parameter I represents the average excitation and ionisation potential of the absorber and is normally treated as an experimentally determined parameter for each element.

This equation, known as the Bethe formula, describes the energy loss for heavy charged particles such as α particles or other heavier nuclei. The Bethe formula is not applicable at low particle energies where charge exchange between the particle and absorber becomes important. The positively charged particle will then tend to pickup electrons from the atoms, which effectively reduces its charge and, consequently, its stopping power. At the end of its track, the particle becomes a neutral atom.

Figure 2.1 shows the stopping power (dE/dx) for protons of 5 MeV in water as a function of the path length, also known as the Bragg curve. It can be seen that as the proton slows down inside matter, the rate of energy loss (stopping power) varies with its kinetic energy, reaching a maximum near the end of its range. The observed peak is also known in the literature as the Bragg peak [21], playing a fundamental role, e.g., in hadron therapy [22]. Towards the very end of the particle range, the dE/dx falls abruptly, and corrections to the Bethe formula have to take into account the exchange of charge between the particle and the medium [23].

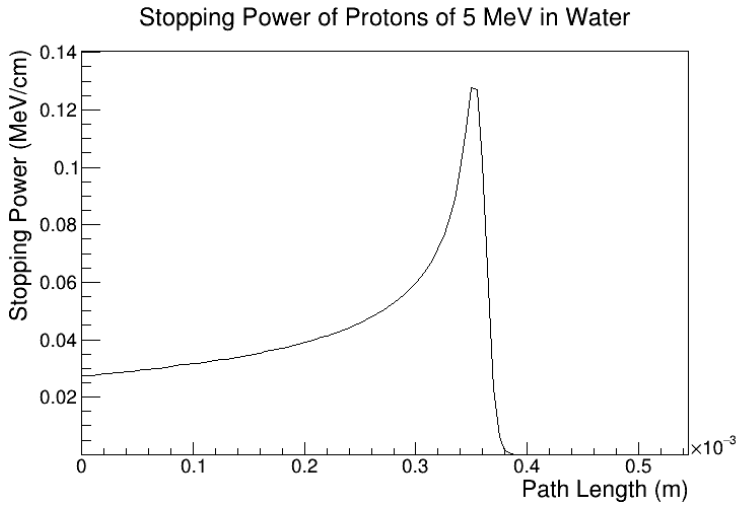

Figure 2.1: Stopping power for protons of 5 MeV in water as a function of the path length.

If we assume the energy loss to be a continuous function, we can define the particle range, which is the average distance a particle can travel inside a material before stopping. The latter depends on the type of material, its density, phase of matter, the kind of particle and its energy. The energy loss is a stochastic process, so, e.g., two identical particles with the same initial energy will suffer different energy losses [24].

2.1.2 Electrons and positrons

In the same way as heavy charged particles, electrons and positrons lose energy by scattering when passing through matter. For the Bethe formula to be applicable, two modifications must be made. First, Due to their small mass, it cannot be assumed that the incident particle

remains undeflected during the collision process. Second, when dealing with interactions between identical particles for electrons or positrons, the quantum-mechanical calculation has to consider them indistinguishable. If the calculations are re-done by taking these two factors into account, the Bethe formula becomes,

$$-\left(\frac{dE}{dx}\right)_c = \frac{2\pi e^4 NZ}{m_0 v^2}\left(\ln\frac{m_0 v^2 E}{2I^2\left(1-\beta^2\right)} - \left(\ln 2\right)\left(2\sqrt{1-\beta^2}-1+\beta^2\right) + \left(1-\beta^2\right) + \frac{1}{8}\left(1-\sqrt{1-\beta^2}\right)^2\right) \tag{2.2}$$

where $\beta = v/c$.

Electrons (or positrons) also differ from heavy charged particles in that energy may be transferred by radiative processes as well as by coulomb interactions. These radiative losses take the form of electromagnetic radiation, known as bremsstrahlung, which can happen from any position along the electron track. In classical terms, this can be understood as radiation arising from the acceleration of the electron (or positron) as it deflects from its straight trajectory by the electrical field of the nucleus. The specific energy loss for this process is given by,

$$-\left(\frac{dE}{dx}\right)_r = \frac{NEZ(Z+1)e^4}{137 m_0^2 c^4}\left(4\ln\frac{2E}{m_0 c^2} - \frac{4}{3}\right) \tag{2.3}$$

The yield from heavy charged particles is negligible as indicated by the presence of the m_0^2 factor in the denominator of the multiplicative term in Equation 2.3. The factors of E and Z^2 in the numerator of Equation 2.3 show that radiative losses are most important for high electron energies and for absorber materials of large atomic numbers.

The total linear stopping power for electrons and positrons is then given by the sum of the collisional and radiative losses,

$$\frac{dE}{dx} = \left(\frac{dE}{dx}\right)_c + \left(\frac{dE}{dx}\right)_r \tag{2.4}$$

2.2 Gamma-Rays

When it comes to interacting with matter, gamma-rays behave differently than charged particles. The main interaction processes of gamma-rays with matter of interest for radiation detectors are: photoelectric absorption, Compton scattering, and pair production.

2.2.1 Photoelectric absorption

A photon can undergo an interaction with an absorber atom, ejecting an energetic photoelectron from one of its bound shells. This process is called photoelectric absorption [25], and the interaction is with the atom as a whole, not with a free electron. The energy of the emitted electron is given by,

$$E_b = h\nu - E_e. \tag{2.5}$$

where E_b is the binding energy of the photoelectron in its original shell and $h\nu$ represents the photon's energy. The photoelectron carries off most of the original photon energy for gamma-ray energies of over a few hundred keV.

The ionised atom returns to the fundamental state through two competitive processes: emission of characteristic X-rays and emission of Auger electrons [26]. In the first case, the vacancy left in the inner shell of the atom is occupied by an electron from an outer shell and the excess energy is released as an X-ray photon; in the second case, there is a rearrangement of electronic shells, resulting in the emission of one of the external electrons.

The absorption cross section at the K shell for gamma-rays can be written as,

$$\sigma^K_{photo} = \left(\frac{32}{\alpha^7}\right)^{1/2} \alpha' Z^5 \sigma_{Th}, \tag{2.6}$$

where α is the photon energy in units of the stationary electron energy, α', is the fine-structure constant, Z is the absorber atomic number, and σ_{Th} is the Thomson scattering cross-section [27].

Due to their low energy, auger electrons typically have a short range in the detection medium and are absorbed. Characteristic X-rays, on the other hand, can travel some distance before they interact again through the photoelectric effect, involving less tightly bound shells, and be reabsorbed, and therefore escaping the detection medium. In the latter case, a smaller energy peak appears in the energy spectrum, the so-called escape peak.

2.2.2 Compton scattering

In Compton scattering [28], the incident gamma-ray photon interacts with an electron of an atom of the detection medium. The incident gamma-ray photon is deflected through an angle with respect to its original direction. A fraction of its energy is transferred to the recoil electron. Although electrons are bound to the atom nucleus, if the gamma-ray energy is significantly higher than the binding energy, this latter energy can be disregarded and the electrons can be

treated as essentially free.

The equation that relates the energy transfer and the scattering angle for any given direction can be derived from the equations for energy and momentum conservation. Considering the scheme of Figure 2.2 in the laboratory reference frame, the following relations can be obtained

$$h\nu' = \frac{h\nu}{1+\gamma(1-cos\phi)},$$

$$T = h\nu - h\nu' = \frac{\gamma(1-cos\phi)}{1+\gamma(1-cos\phi)},$$

$$cos\phi = 1 - \frac{2}{(1+\gamma)^2 tan^2\theta + 1},$$

$$cos\theta = (1+\gamma)tan\frac{\phi}{2},$$

where $\gamma = h\nu/m_e c^2$ and T is the recoil energy.

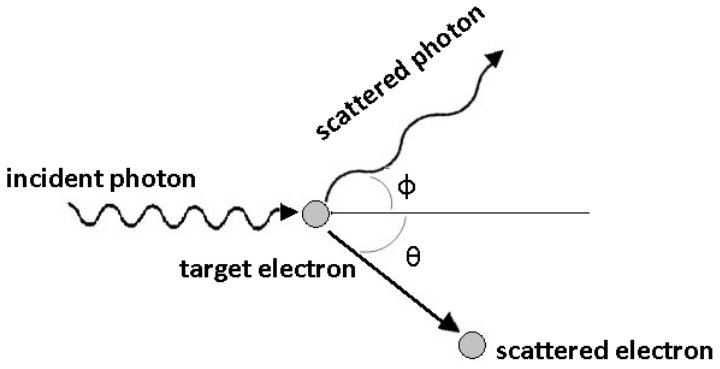

Figure 2.2: Geometry of Compton Scattering showing the directions of the scattered photon and electron with respect to the direction of the incident photon. Taken from [29].

The angular distribution of scattered gamma-rays is predicted by the Klein-Nishina formula for the differential scattering cross section [30],

$$\frac{d\sigma}{d\Omega} = \frac{Zr_e^2}{2}\frac{1}{[1+\gamma(1-cos\phi)]^2}\left[1+cos^2\phi + \frac{\gamma^2(1-cos\phi)^2}{1+\gamma(1-cos\phi)}\right] \tag{2.7}$$

where r_e is the classical electron radius. The probability per electron for a Compton scattering to occur is given by integrating the formula above over $d\Omega$,

$$\sigma_c = 2\pi Zr_e^2\left\{\frac{1+\gamma}{\gamma^2}\left[\frac{2(1+\gamma)}{1+2\gamma} - \frac{1}{\gamma}ln(1+2\gamma)\right]\frac{1}{2\gamma}ln(1+2\gamma) - \frac{1+3\gamma}{(1+2\gamma)^2}\right\}. \tag{2.8}$$

The Compton scattering probability exhibits a dependence with the energy of the incident photon and also with the atomic number of the material. This probability tends to be lower for

low-energy gamma rays since the photon may not have enough energy to dislodge electrons from their bound states within atoms. As photon energy increases, the likelihood of interaction rises, resulting in more prominent scattering phenomena. The probability of Compton scattering is enhanced by materials containing atoms with a higher atomic number due to the higher number of electrons available for the interaction.

2.2.3 Pair production

When an incident gamma-ray has at least 1.022 MeV (twice the rest mass energy of an electron), it is energetically possible that this photon is converted into an electron-positron pair. This interaction can only occur in the presence of a third body so that the momentum can be conserved, usually in the nucleus's Coulomb field.

In general, the effective cross sections for the pair production in the field of a nucleus or an orbital electron have the following form,

$$\sigma_{\text{pair}} = \alpha' r_e^2 Z^2 P(\epsilon, Z) \tag{2.9}$$

where α' is the fine structure constant, r_e is the classical electron radius, Z is the absorber atomic number, and $P(\epsilon, Z)$ is a function that depends on the atomic number and the photon energy divided by the electron rest mass ϵ [27].

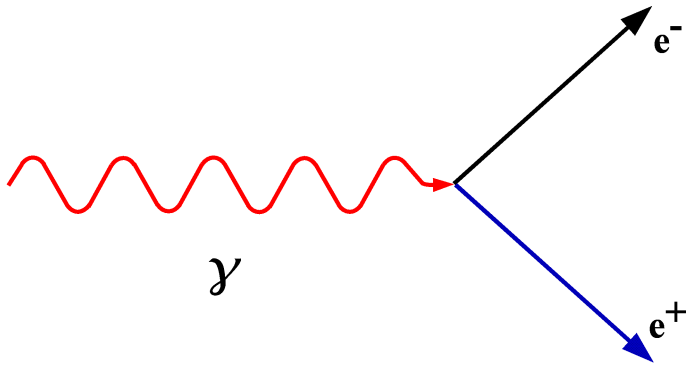

Figure 2.3: Creation of an electron and positron pair via pair production. Taken from [31].

2.2.4 Gamma-ray Attenuation

If we consider a transmission experiment, where monoenergetic gamma rays are collimated into a narrow beam incident on an absorber of a certain thickness, the beam intensity at the exit of the absorber is attenuated by a certain factor due to the interaction of photons in the material through the processes described above. The beam attenuation depends on the energy of the

incident photon, the mass density and the atomic number of the material as described by the Beer-Lambert law [32],

$$I(x) = I_0 \exp(-\mu x)$$

where I_0 is the incident beam intensity, x is the material thickness, and μ is the absorption coefficient.

The total probability for a gamma-ray to interact with matter is the sum of the individual cross-sections of the previously mentioned processes

$$\sigma_{total} = \sigma_{ph.el} + \sigma_{Compt} + \sigma_{pair}$$

The absorption coefficient is then obtained by multiplying the total cross-section by the density of atoms,

$$\mu = N\sigma = \sigma(N_a\rho/A) \tag{2.10}$$

Where Na is Avogadro's number, is the density of the material, and A is the molecular weight. As an example, it is shown in Figure 2.4 the absorption coefficient for each one of the photon interaction processes in lead as a function of the gamma rays energy. The photoelectric effect is dominant at low energies, Compton scattering is the main effect at energies around 1 MeV, and pair production prevails at higher energies.

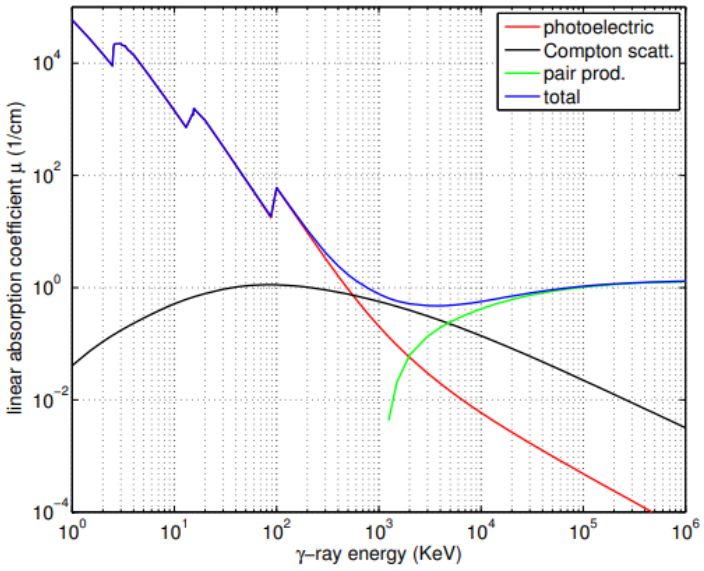

Figure 2.4: Linear absorption coefficient μ in lead as a function of the γ-ray energy for different processes. Taken from [33].

2.3 Neutrons

Neutrons are electrically neutral and, therefore, do not interact with the electrons of the atom, but rather with its nucleus with the interactions being mediated by the strong force. Due to the short range of the interaction, they penetrate much deeper into matter when compared to charged particles. Neutrons are also more sensitive to light atoms like hydrogen and are scattered differently by isotopes of the same element. Additionally, as a result of the magnetic moment of their constituent quarks, they are also sensitive to the magnetic spins of both nuclei and electrons, allowing probing magnetic properties of materials. These unique features of the neutrons make them a powerful probe for studying the properties of condensed matter. On the other hand, this is also the reason why building efficient neutron detectors is not a trivial task as neutrons are unable to ionise the atoms [34].

The energy (E_n) of a neutron in a non-relativistic limit can be described in terms of its wavelength through the de Broglie equation,

$$\lambda = \frac{2\pi\hbar}{m_n v} \quad \Longrightarrow \quad E_n = \frac{1}{2} m_n v^2 = \frac{\pi\hbar^2}{m_n \lambda}, \tag{2.11}$$

where m_n is the mass of the neutron, $\hbar$ is the reduced Planck's constant and v is the neutron velocity.

As neutrons may have different types of interactions with a nucleus depending on their energy, it is useful to classify them according to what is called "neutron temperature" (seen in Table 2.1). The origin of this name comes from comparing their energy $k_B T$ with room temperature (where k_B is the Boltzmann constant, and T is the absolute temperature corresponding to 20 °C or about 25 meV).

Energy classification	Kinetic energy (eV)	Wavelength (Å)
Ultra cold	$E_n < 3 \times 10^{-7}$	$\lambda > 520$
Very cold	$3 \times 10^{-7} < E_n < 5 \times 10^{-7}$	$520 > \lambda > 40$
Cold	$5 \times 10^{-7} < E_n < 0.005$	$40 > \lambda > 4$
Thermal	$0.005 < E_n < 0.5$	$4 > \lambda > 0.4$
Epithermal	$0.5 < E_n < 10^3$	$0.4 > \lambda > 0.01$
Intermediate	$10^3 < E_n < 10^5$	$0.01 > \lambda > 0.001$
Fast	$10^5 < E_n < 10^{10}$	$0.001 > \lambda > 3 \times 10^{-6}$

Table 2.1: Neutron classification by kinetic energy and wavelength.

When the a neutron interact with the nucleus, depending on its energy, they may undergo one of the following nuclear processes:

I. Elastic scattering from the nuclei, i.e., $A(n,n)A$. In elastic scattering, the total kinetic

energy of the neutron and nucleus system is unchanged. This interaction represents the principal mechanism of energy loss for neutrons in the MeV region.

II. Inelastic scattering, e.g., $A(n,n')A^*$. Inelastic scattering occurs when the incident neutron has sufficient energy, usually in the order of 1 MeV, to cause the nucleus to transfer to an excited state from which it eventually de-excites and releases radiation. The total kinetic energy is not preserved as part of it is used to transition the nucleus into an excited state.

III. Neutron capture, such as (n,γ), (n,p), (n,d), (n,α), (n,t), $(n,\alpha p)$, etc. Captured neutrons may cause a rearrangement in the internal structure of the target atom, releasing gamma rays, neutrons, and charged particles. In general, the cross-section for neutron capture scales approximately as $1/v$ with neutron velocity, as a result, cold and thermal neutrons are the most likely to undergo a capture process.

IV. Fission, i.e., (n,f). Fission occurs when a neutron is absorbed by an atom with a large atomic number, forcing it to excite and split into smaller atoms and more neutrons. This process is also most probable for neutrons at thermal energy.

V. High energy hadron shower production. When high-energy neutrons collide with the nuclei of atoms in a material, they can initiate hadronic interactions, leading to the production of secondary particles. These secondary particles, including other neutrons, protons, pions, and other hadrons, then form the cascade of particles that constitutes a hadronic shower. This occurs only for very high-energy neutrons with E>100MeV.

The probability of each one of these processes to occur is described by the respective cross section. For a given nuclide, the total cross section is then given by the sum of the individual cross-sections,

$$\sigma_{total} = \sigma_{elastic} + \sigma_{inelastic} + \sigma_{capture} + ...$$

Multiplying the total cross section of a certain nuclide by its density of atoms (N), it is obtained the macroscopic cross section,

$$\Sigma_{\text{total}} = N\sigma_{\text{total}} = \sigma_{\text{total}}\, N_a\rho/A \tag{2.12}$$

which has dimensions of cm^{-1}. The average distance a neutron travels between interactions is obtained by the reciprocal of this quantity, giving the mean-free-path,

$$\lambda = 1/\Sigma_{total} \tag{2.13}$$

In the context of neutrons, this quantity has the same meaning as the linear absorption coefficient for gamma rays. Thus, in a beam attenuation experiment similar to that of gamma rays, a focused beam of neutrons passing through a material will experience an exponential attenuation described by,

$$\frac{I}{I_0} = \exp(-x/\lambda), \tag{2.14}$$

where x is the thickness of the material. In solid materials, λ for slow neutrons may be of the order of a centimetre or less, whereas for fast neutrons, it usually is tens of centimetres.

Since neutrons do not produce direct ionisation or generation of light, which are essential processes in most radiation detectors, they cannot be directly detected, and an intermediate reaction with the nuclei is needed to produce an ionising particle. From the processes listed above, only the I, III and IV are relevant for the purposes of neutron detection. Fast neutrons can be detected through process I, exploiting the transfer of neutron energy to a recoiling nucleus, which in turn will produce ionisation in the detection medium. The detection of low-energy neutrons (below the epithermal region) can be accomplished through some of the nuclear reactions described by processes III or IV, resulting in the emission of charged particles. From the point of view of detector performance, ideally, a capture reaction should exhibit a high cross-section, high reaction heat, and result in only the emission of charged particles. A more detailed description of the process involving the detection of low-energy neutrons is given in Chapter 4.

Chapter 3

Resistive Plate Chambers

Invented in the eighties of the last century by R. Santonico and R. Cardarelli [35], the Resistive Plate Chamber (RPC) is a type of gaseous detector from the family of the parallel plate avalanche chambers and Pestov spark counters [36], differing by the fact that at least one of their electrodes is made of a material with a high volume electrical resistivity, such as, e.g., soda lime glass or bakelite. This makes this type of detector intrinsically protected against discharges and able to operate with high charge multiplication gains. Only a local spot where a discharge begins to grow is subject to a decrease in the electric field in the gas gap and is blind for a certain time, determined by the relaxation time (τ) of the resistive material, with all the remaining detector area still continuing to be sensitive to particles. The relaxation time is given by,

$$\tau = \rho \epsilon_0 \epsilon_r \tag{3.1}$$

with ρ being the volume resistivity of the material, ϵ_0 the dielectric constant and ϵ_r the relative permittivity of the resistive material. Depending on the type of material, τ can range, e.g., from a few milliseconds for Bakelite ($\rho \approx 10^{10}\ \Omega cm$) to about 1 second for glass ($\rho \approx 10^{12}\ \Omega cm$).

The first RPC to be built was made with copper electrodes covered with a high resistivity phenolic resin separated by a gap of 1.5 mm filled with an Argon/iso-butane gas mixture of 1:1 at atmospheric pressure, and operated in streamer mode, showing a 97% efficiency and a 500 ps time resolution. This early version demonstrated the feasibility of using an RPC for particle detection and timing measurements, becoming an affordable alternative to the use of plastic scintillators, especially in large detection areas due to their simplicity in construction and low cost [37].

In the following years, the RPC design was improved by optimising the gas mixture, the materials for the resistive plates, and the electrode configuration, leading to improved time

resolution, particle detection efficiency and count rate capability [37][38]. The RPCs gained popularity throughout the 90s and 00s, and has been widely used in high-energy physics such as, e.g., in ATLAS and CMS muon trigger detection systems of the Large Hadron Collider (LHC) at CERN [39], and astroparticle physics such as ARGO [40], MONO-LITH [41] at YangBaJing or INO [42]. More recently, RPC applications in biomedical applications are giving promising results, for example, in muon tomography [43] and RPC-PET brain scanners [44].

3.1 Standard RPC Design

The standard configuration of an RPC is shown in Figure 3.1. An anode and a cathode plate made of a high-resistivity material are separated by spacers defining an uniform gas gap width of a few millimetres. These plates are painted on their external surfaces with a material with high surface resistivity (e.g., graphite), with the functionality to distribute the potential uniformly over their area. The electrical potential difference between the anode and cathode results in a uniform electric field inside the gas gap.

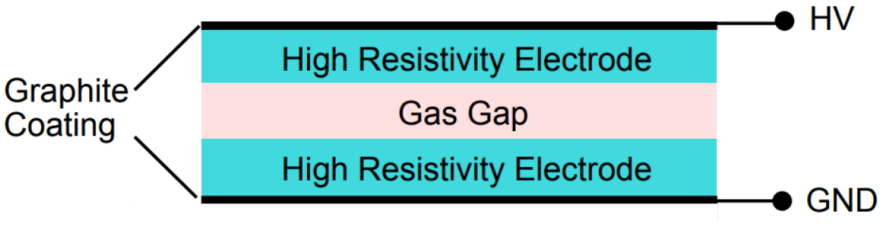

Figure 3.1: General configuration of an RPC. Adapted from [45].

3.2 Principles of Operation

3.2.1 Gas Ionisation

If the energy loss in ionising collisions is negligible compared to the incoming particle energy, we can assume that each ionising collision is independent of its previous one. In that case, for minimum ionising particles (MIPs), the distance between collisions (the distance between primary clusters) is exponentially distributed, and the number of clusters on the distance between the electrode plates d follows a Poisson distribution with an average of $n = d/\lambda$, where λ is the mean free path [46]. Thus, the probability of having n clusters is given by

$$P(n) = \frac{1}{n!}\left(\frac{d}{\lambda}\right)^{n} e^{\left(-\frac{d}{\lambda}\right)} \tag{3.2}$$

The number of clusters per unit length can vary significantly depending on the gas mixture. The count can range from less than one cluster per millimetre to approximately ten clusters, as reported in [45]. Moreover, a cluster distribution can be generated by a single collision, resulting in the ejection of a varying number of electrons. A list of the average number of clusters for a distance of 1 mm for a few common gases used as a detection medium is presented in Table 3.1 taken from [45].

Gas	He	Ar	Xe	$i - C_4H_{10}$
$\bar{n}$ [clusters /mm]	0.42	2.3	4.4	8.4

Table 3.1: Simulated values for the average number of clusters per mm for different gases for a MIP.

3.2.2 Electron Multiplication

Inside the gas gap of the RPC, the free electrons generated by primary ionisation are accelerated by the applied field, and if they achieve kinetic energy greater than the ionisation energy of the gas molecule, it is possible that an additional ion-electron pair is created. This behavior is also applied to the newly generated electrons leading to a charge multiplication process known as a Townsend avalanche [47].

The evolution of the number of electrons or ions within a region where an electric field is applied was shown to follow the equations [48],

$$\frac{\partial n_e(x,y,z,t)}{\partial t} = \alpha n_e \left|v_e\right| - \nabla\left(n_e v_e\right) + D_e \nabla^2 n_e \tag{3.3}$$

$$\frac{\partial n_i(x,y,z,t)}{\partial t} = \alpha n_e \left|v_e\right| - \nabla\left(n_i v_i\right) + D_i \nabla^2 n_i \tag{3.4}$$

where n_e and n_i are respectively the number of electrons and ions, D_e and D_i are respectively the electron and ion diffusion coefficients, v_e and v_i are respectively the electron and ion drift velocity, and α is the number of ionising collisions per unit length of electron trajectory (first Townsend coefficient). The first term on the right refers to the electron multiplication process, while the other two describe charge carriers' drift and spatial diffusion.

In the simplest case where n_0 electrons are released at an instant $t = 0$ at a point taken as zero position, and making simplifying assumptions that the longitudinal and transversal diffusion coefficients are equal, and the electron velocity v_e, and Townsend coefficient α remains constant during propagation, the solution for the equation 3.3 is [48],

$$n_e(x,y,z,t) = N_0 e^{\alpha v_e t} \frac{1}{(4\pi D_e t)^{3/2}} \exp\left(-\frac{x^2+y^2+(z-v_e t)^2}{4D_e t}\right) \tag{3.5}$$

In this case, the avalanche can be described by an exponential growth of charges, diffusing in space with an average radius that increases with $\sqrt{D_e t}$.

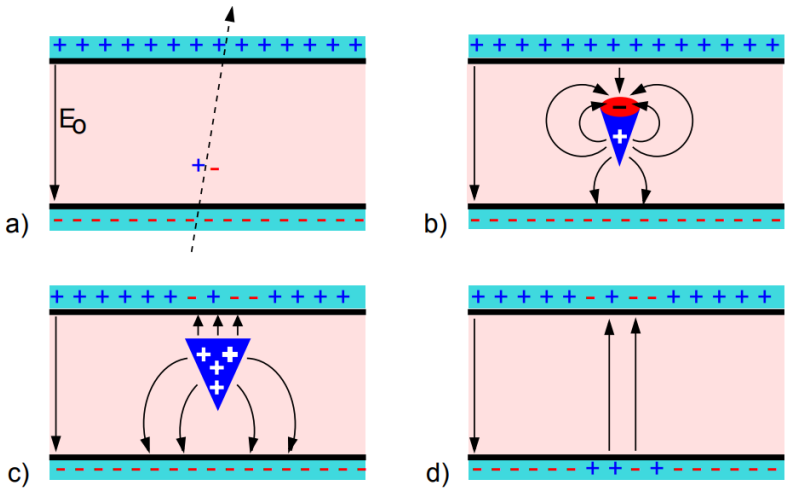

Figure 3.2: Schematic drawing of the development of an electron avalanche in an RPC and the electric field change caused by the avalanche charges at a large gain (E_0 is the applied electric field): (a) the passage of a charged particle ionises some gas atoms, and an avalanche is started; (b) the avalanche size is sufficiently large to influence the electric field in the gas gap; (c) the electrons reach the anode; (d) later, the ions that drift much slower reach the cathode. The charge depletion in the resistive plates influences the field in a small area around the position where the avalanche developed. Taken from [45].

3.2.3 Space Charge Effect

The avalanche, which grows exponentially, consists of two parts, a tip of fast-moving electrons and a tail of slow-moving positive ions. At some point, when the number of charges (electrons and ions) grows large enough, the own field created by the avalanche charges is comparable to the applied one, resulting in a reduction of the effective field in a large region of the centre of the avalanche and an increase in the tip and tail, affecting the charge carriers drift velocity and the Townsend coefficient. Under these circumstances, the avalanche propagation and multiplication characteristics are strongly modified. At the centre of the avalanche, where the field is weaker, the multiplication is reduced, and the number of electrons subject to attachment increases, with a consequent increase of negative ions. This mechanism is illustrated in Figure 3.3 and is known as the space charge effect and is considered a critical factor in understanding the functioning of RPCs [49].

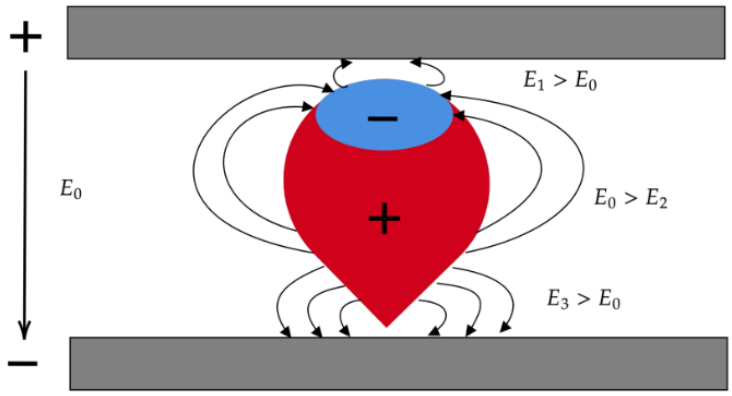

Figure 3.3: Schematic of an avalanche and its effect on the electrical field strength. The electric field is reduced between the electron cloud head and the positive ions and increased in front of the anode. Taken from [50].

At very high electric fields, UV photons emitted during the avalanche development may start to ionise gas molecules surrounding the avalanche, changing the dynamics of its propagation, which results in a fast increase of the charge growth. At a later stage, a conductive channel can be formed between the two electrodes, thereby discharging the local surfaces of the electrodes. This phenomenon is referred to as a streamer, and generally, it is accepted that the conditions for its generation are associated with the space charge effect [49].

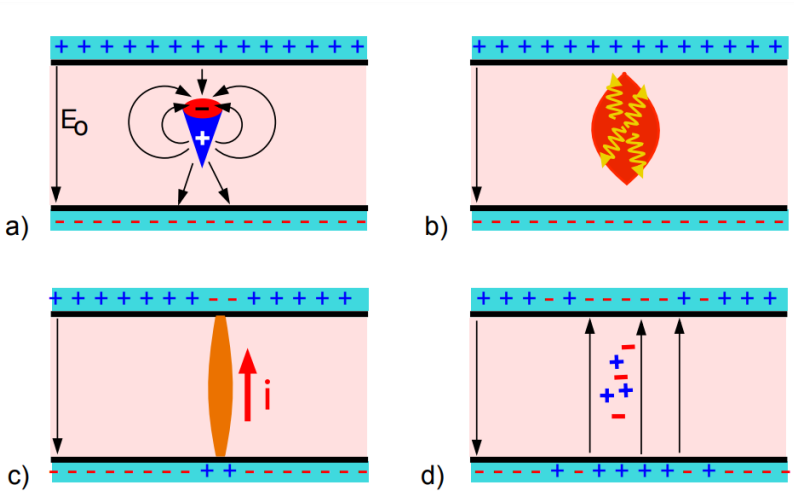

Figure 3.4: Schematic drawing depicting the steps leading to the generation of a streamer in an RPC: (a) an avalanche is developing as in Fig. 3.2; (b) the electric field created by the avalanche charge is comparable to the applied one, resulting in a reduction of the effective field, and UV photons may start contributing to the avalanche's growth causing it to spread quickly and a streamer evolves; (c) A conductive channel between the two electrodes may develop, discharging the surface of the electrode locally; (d) The magnitude of the electric field strongly decreases around the avalanche spot. Taken from [49].

3.2.4 RPC Operation Modes

RPCs can be operated in avalanche or streamer mode. In avalanche mode, the RPC is operated with a lower charge multiplication gain, typically with an average charge produced per event below 10 pC. When compared with the streamer mode, the avalanche mode allows operating the RPC at a higher count rate before saturation, however, it requires more sensitive and low noise amplification electronics [51].

In streamer mode, there is a large charge growth (tens of pC to a few nC) compared to the avalanche mode. This mode takes advantage of the large current pulses induced by the streamers, which simplifies the electronic readout, not needing pre-amplification. Due to the large amount of charge generated per event, the counting rate capability of RPCs operated in the streamer mode is limited to a few hundred Hz/cm^2 [52].

3.3 Signal Induction

In gaseous detectors, the signal is induced by the charge carriers when they start their drift and not just when they are collected on the respective electrodes. Once all the charge carriers have been collected, the induction process ends, and the signal is fully developed.

The Shockley–Ramo Theorem [53] gives us the equation for the current I induced in one electrode by the drift of a particle with charge Q moving along a trajectory $\vec{x}(t)$ inside a detector. According to this theorem, the induced charge in one electrode is given by,

$$I(t) = Q\vec{E}_w(\vec{x}(t)) \cdot \dot{\vec{x}}(t) \tag{3.6}$$

Where $\dot{\vec{x}}(t)$ is the velocity of the particle, and E_w is the weighing field, which is a function that characterises the spatial sensitivity of the detector to the charge's motion. In practice, Ramo's theorem translates the current resulting from the temporal variation of the surface charge density induced on an electrode when a charge Q moves near it.

As mentioned above, gaseous detectors are based on the principle of ionisation of the gas along the path of a charged particle interacting in the detector's active volume, with the signal induction in the collection electrodes being due to the drift of the charge in the applied electric field. If the detector elements are essentially insulators, and the electrodes have infinite conductivity, the induced signal can be determined by Ramo's theorem. In the case of RPCs, which consist of resistive electrodes, the time dependence of the signals is not only a function of the movement of charges but also of the relaxation time characteristic of the resistive material [54].

A formalism proposed by W. Riegler [55] considers a quasi-static approximation of Maxwell's

equations that allows the induced signals to be determined for materials whose weighting field depends on time. This approach gives important conclusions: for a time T of the order of 3 ns, equivalent to the time development of the electronic component of the induced signal, the time constant ($\tau = RC \approx \rho$) of the RC circuit formed by the resistive electrodes (of the order of tens of milliseconds for bakelite electrodes and of a second for glass) is such that $\tau >> T$. Under these conditions, the conductivity of the resistive electrodes does not affect the induced signal, as they behave like perfect dielectrics ($R = \infty$) and are practically transparent to induced signals.

In the case of an RPC, which has a parallel geometry, if we set one electrode to a voltage of 1 V and the other to 0 V, the weighting field takes the form of $E_w = \hat{z}/d$, where d is the gap between the electrodes. If n_e electrons drift simultaneously from the cathode in the field $E_0 = V_0/d$, with a constant drift velocity v_e, a current is formed in the direction of the anode during the transit time of the electrons, $T_e = d/v_e$, which is given by,

$$I_e(t) = en_e\vec{v}_e \cdot \vec{E}_w = \frac{en_e(t)}{T_e} \quad 0 \leq t \leq T_e \tag{3.7}$$

As the number of electrons grows exponentially according to the Townsend multiplication, if the diffusion term from Equation 3.3 is neglected, the electron component of the induced current becomes,

$$I_e(t) = \frac{en_0}{T_e}\exp(\alpha v_e t) \quad 0 \leq t \leq T_e \tag{3.8}$$

$$I_e(t) = 0 \quad t > T_e \tag{3.9}$$

This corresponds to the fast component of the induced signal in a RPC. This fast signal generated by the rapid drift of electrons is typically used for the timing measurement

Similarly, the positive ions resulting from avalanche multiplication drift towards the cathode plate, inducing a current given by [56],

$$I_+(t) = \frac{en_0}{T_+}\{\exp(\alpha v_e t) - \exp(\alpha v^* t)\} \quad 0 \leq t \leq T_e \tag{3.10}$$

$$I_+(t) = \frac{en_0}{T_+}\{\exp(\alpha d) - \exp(\alpha v^* t)\} \quad T_e \leq t \leq T_+ + T_e \tag{3.11}$$

$$\frac{1}{v^*} = \frac{1}{v_+} + \frac{1}{v_e}$$

Where v_+ is the drift velocity of the positive ions and T_+ is it's transit time. Since v_e is typically 3 orders of magnitude larger than v_+ [56], we can approximate $v^* \approx v_+$,

$$I_+(t) = \frac{en_0}{T_+}\{\exp(\alpha d) - \exp(\alpha v_+ t)\} \quad T_e \leq t \leq T_+ + T_e \tag{3.12}$$

Figure 3.5 illustrates the induced currents during an avalanche if electron attachment does not take place. The blue curve shows the fast current created by the electron, which stops abruptly at the time T_e when it reaches the anode. The yellow curve shows the current created by the positive ions. Because of their slower drift velocity compared to the electrons, the induced current is much smaller.

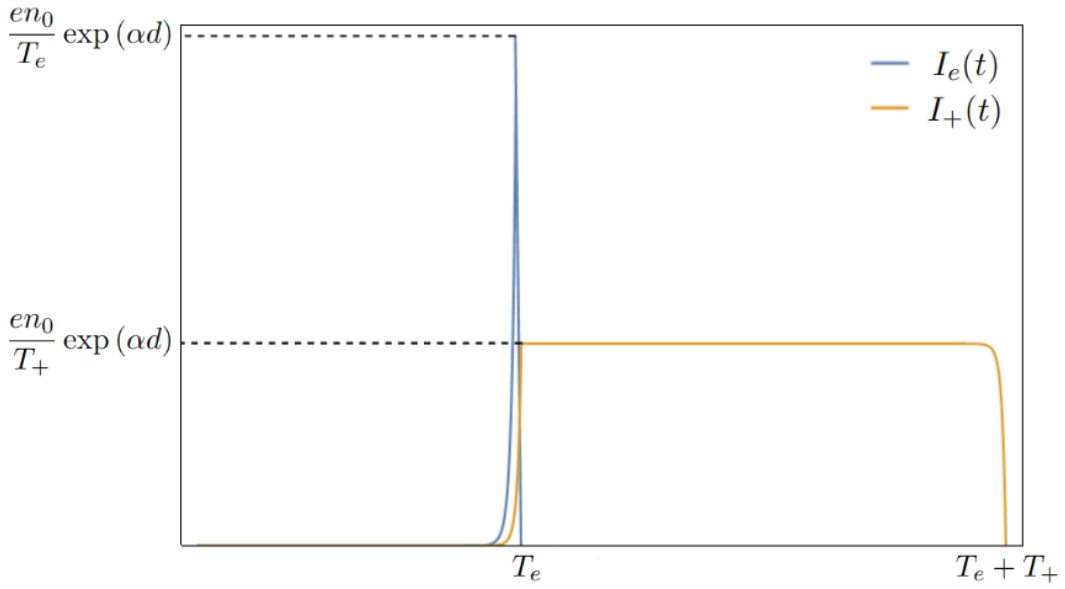

Figure 3.5: Induced currents by the electrons (blue) and positive ions (yellow) during an avalanche if electron attachment does not take place. Y axis is not to scale.

3.4 Position Readout

In RPCs, the location of the point of interaction of a particle is obtained by readout the signals induced in a structure of electrodes with a suitable geometry, e.g., arrays of parallel signal pickup strips, or pads, engraved on a printed circuit board (PCB) are usually used for this purpose. The distribution of the amplitudes of the induced signals in each electrode (strips or pads), is correlated with the location where an ionising particle interacted. The spatial distribution of the induced charge, resulting from the detection process initiated by an ionising particle in the RPC, depends on several factors: spatial distribution of the primary ionisation in the gas gap, electron diffusion, spread of the avalanche during its development and on the electrical resistivity of the RPC plates and resistive layer used for the distribution of potential across the RPC plates.

The most used and simpler geometry for the signal pickup electrodes consists of arrays of

parallel strips, with one array facing the anode plate, and the other, with the strips oriented normally to the previous one, facing the cathode plate, as shown in Figure 3.6.

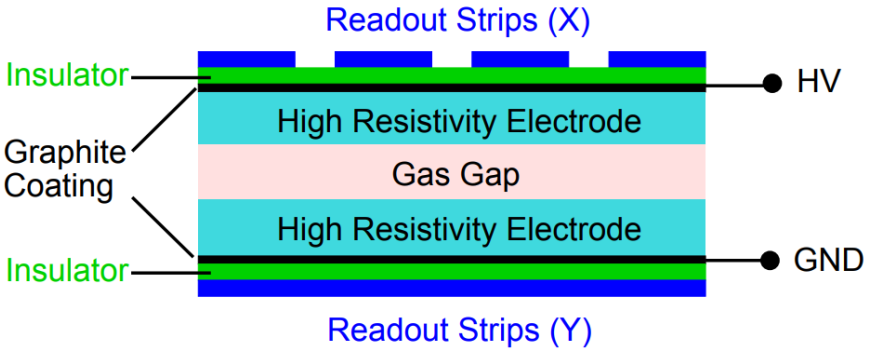

Figure 3.6: General schematic of an RPC with readout strips placed on the outer surfaces of the electrodes. The strips are separated from the electrode by an insulator material. Taken from [45]

Large area RPC detectors typically used centimetre-wide strips to provide avalanche localisation capability) More recent RPC applications, e.g., in muon tomography and cosmic ray tracking, require the measurement of both X and Y coordinates with a higher accuracy. In order to achieve this involves sensing the induced charges with arrays of strips with dimensions (pitch and strip width) in the millimetre range and the use of more advanced position reconstruction methods, such as, e.g., the centre of gravity (COG) technique. Submillimetre resolution has already been successfully demonstrated for RPCs in both high-energy physics and biomedical applications using this approach [57][58].

Chapter 4

The ^{10}B-RPC Technology

A novel technology for thermal neutron detection, combining RPCs with solid-state neutron converters, was recently introduced by the Neutron Detector Group [15] at LIP-Coimbra. The basic feasibility of such technology was already demonstrated in the framework of the SINE2020-H2020 project [59]. The results of first tests on a neutron beamline at ILL, with a detector prototype built using this technology, showed that it was capable of sub-millimetre spatial resolution and a detection efficiency $> 50\%$ for neutrons with a wavelength of 4.7 Å [16]. Taking advantage of the adaptable modular designs, scalability, and cost-effectiveness per unit area offered by RPCs, this neutron detection technology can be a cost-effective alternative to the ^{3}He for the construction of position-sensitive thermal neutron detectors capable of state-of-the-art performance.

RPCs are not sensitive to thermal neutrons by themselves. To detect thermal neutrons, a solid-state neutron converter must be lined, at least, onto one of the inner surfaces of the RPC plates facing the gas gap. This converter must be loaded with an isotope showing a high cross section for neutron capture and a suitable reaction. The neutron capture reaction must result in the emission of charged particles, which can enter the RPC gas gap and thus generate ionisation, initiating the neutron detection process. Only a limited set of isotopes can effectively play this role, such as ^{3}He, ^{6}Li, ^{10}B, and ^{157}Gd. As nowadays, ^{3}He is scarce and expensive, alternatives have been sought, with ^{10}B in solid-state materials, like B_4C [8] emerging as the most promising candidate for the job.

In this chapter, the basic principles of thermal neutron detection are presented, and the concept of an RPC-based position-sensitive neutron detector (PSND), developed at LIP-Coimbra, for high neutron detection efficiency ($> 50\%$) and sub-millimeter spatial resolution is introduced.

4.1 Thermal Neutron Detection Principles

The significant interactions for cold and thermal neutrons include elastic scattering with absorber nuclei and a set of neutron-induced nuclear reactions, as described in Chapter 2. Although elastic collisions are very likely, this is not an interaction on which cold and thermal neutron detectors are based due to the small energy transfer to the nucleus, which results in no observable recoil. Elastic collisions often serve to bring the neutrons into thermal equilibrium with the medium before a different type of interaction occurs.

In view of neutron detection, the interactions of cold and thermal neutrons of real importance are neutron-induced reactions that can originate secondary particles of sufficient energy to be detected directly. Because of the low energy of the incident neutron, all such reactions must have a positive Q-value to be energetically possible. In most materials, the radiative capture reaction or the (n, γ) reaction, is the most probable, playing a critical role in the absorption of neutrons. However, because the secondary radiation takes the form of gamma rays, this reaction is not widely used since gammas are also difficult to detect or be detected far from the capture location, losing position information. In contrast, reactions such as (n, α), (n, p) and $(n, fission)$ are better suited for the detection process since they have charged particles as reaction products. When searching for nuclear reactions that might be useful in neutron detection, several factors must be taken into account. First, the neutron capture cross-section must be as large as possible so that detectors with high detection efficiency can also be built in small dimensions. Following the logic of a scalable detector, the target nuclide should either be of high isotopic abundance in the natural element or an economically viable supply of artificially enriched samples should be available for detector production. The energy liberated in the reaction (Q-value) is most important after the neutron capture. The higher the Q-value, the greater the energy transferred to the reaction products, easing the discrimination against γ-ray and other radiation backgrounds.

The isotopes which provide a suitable nuclear reaction are ^{3}He, ^{6}Li, ^{10}B and Gadolinium (see Table 4.1).

Isotope	State	Reaction	Cross section ($barn$)	Product energies (keV)
^{3}He	Gaseous	$^{3}\mathrm{He}(n,p)t$	5333	$p : 573,^{3}\mathrm{He} : 191$
^{6}Li	Solid	$^{6}\mathrm{Li}(n,\alpha)t$	940	$^{3}\mathrm{He} : 2727, \alpha : 2055$
^{10}B	Solid	$^{10}\mathrm{B}(n,\alpha)^{7}\mathrm{Li}$	3836	$\alpha : 1472,^{7}\mathrm{Li} : 480(93\%)$
				$\alpha : 1780,^{7}\mathrm{Li} : 1020(7\%)$
$^{10}BF_3$	Gaseous	$^{10}\mathrm{B}(n,\alpha)^{7}\mathrm{Li}$	3838	$\alpha : 1472,^{7}\mathrm{Li} : 480(93\%)$
				$\alpha : 1780,^{7}\mathrm{Li} : 1020(7\%)$
^{nat}Gd	Solid	$^{nat}\mathrm{Gd}(n,\gamma)$	49122	$Ce : 29 - 182$

Table 4.1: Isotopes cross sections for thermal neutron absorption and their product energies.

A generic neutron detector system can be divided into three main components: the neutron converter which is a material made with one of the isotopes listed in Table 4.1 that gives the detector its sensitivity to neutrons; the detector system that can efficiently detect the particles produced by the neutron interaction with the converter material; and the signal processing electronics that amplify, shape, and digitise the signals generated by the detector system. A representation of a generic neutron detector as a system is depicted in Figure 4.1.

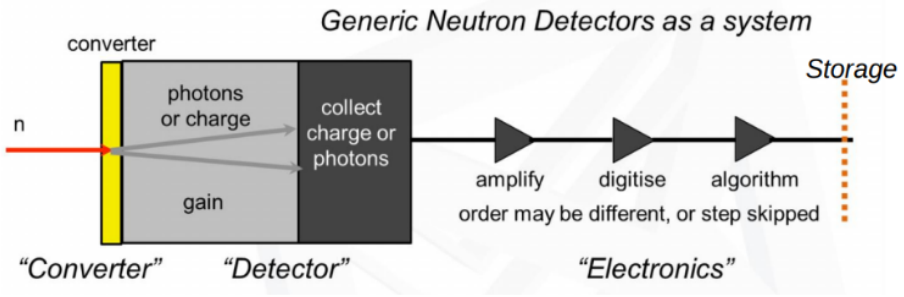

Figure 4.1: Schematic drawing of a generic neutron detector as a system. The system is divided into three main components: the neutron converter, the detection system and the signal processing electronics. Taken from [60]

Neutron detectors are classified into two main categories: gaseous detectors and solid-state detectors. In gaseous detectors, the converter can take the form of a gas (such as ^{3}He and BF_3), which serves as both a converting and detection medium or a solid material integrated into the detector architecture but separated from the detection medium. Solid-state detectors, on the other hand, use neutron-sensitive scintillators containing isotopes that react to neutrons and generate scintillation. There are also semiconductor detectors interfaced with neutron converters, but this type of technology is much more expensive compared to the previous ones, and are only used for small area detectors. They are also prone to radiation damage, which reduces their performance over time, and are therefore not commonly used in neutron scattering science.

4.1.1 Neutron Gaseous Detectors

Gaseous neutron detectors operate on the principle of capturing and detecting neutrons through interactions with gas atoms. When a neutron enters the gas-filled detector, it may undergo a capture process with the gas atoms, resulting in the emission of charged particles that can generate primary ionisation. For example, in a ^{3}He-filled detector (Figure 4.2), the tritium and the proton resulting from neutron capture in ^{3}He will generate ionisation gas. In the presence of an electric field, the electron-ion pairs drift toward a certain structure of electrodes (e.g., proportional tubes, multiwire chambers, microstrip plates, gas electron multipliers) where they are subject to a gas amplification process.

The ^{3}He high neutron capture cross section (5333 barns), in combination with high-pressure operation, allows the design of robust, highly efficient and long-lived neutron detectors, providing neutron/gamma separation in the order of approximately 10^{-7} [4]. As a result, ^{3}He-filled proportional counters became the golden standard for cold/thermal neutron detection.

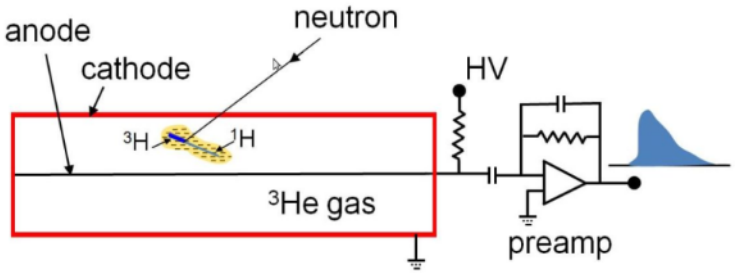

Figure 4.2: Schematics of a neutron detection in a ^{3}He proportional counter.

However, as the availability of ^{3}He became scarce, alternatives like ^{10}B and ^{6}Li became more popular. Their respective capture cross-sections are 71.9% and 17.6% of the cross-section of ^{3}He. Both can be found on Earth with an average abundance of ^{10}B occurring at 20% of natural boron and ^{6}Li at approximately 7% of natural lithium, respectively. Boron trifluoride was seen as a direct replacement for ^{3}He, but due to its toxicity and inability to perform at high pressures, research with BF_3 filled detectors was discontinued and even outlawed in European facilities.

4.1.2 Neutron-Sensitive Scintillator Detectors

A neutron-sensitive scintillator detector relies on scintillating materials that are typically loaded with ^{6}Li, ^{10}B or ^{157}Gd isotopes. In this case, the neutron capture reaction products are stopped inside the scintillator, with their energy being transferred to the generation of scintillation. The neutron detection is accomplished by readout the emitted photons with photosensors. These scintillators can be coupled directly or via optical fibre to a photo sensor such as a Photomultiplier (PMT), Multianode Photomultiplier (MaPMT) or a Silicon Photomultiplier (SiPMT).

The most commonly used scintillators are ^{6}Li-loaded cerium glass and ^{6}Li/ZnS. Both have distinctive characteristics. ^{6}Li glass has a short decay time, making it a high-efficiency scintillator, however, they have weak neutron/gamma discrimination due to its low ratio of light yield photons per neutron and per gamma-rays. In contrast, Zn/S has a high light generation per neutron but a long decay time, resulting in low gamma sensitivity but a limited counting rate. Zn/S scintillator is also opaque to its own light and suffers from afterglow.

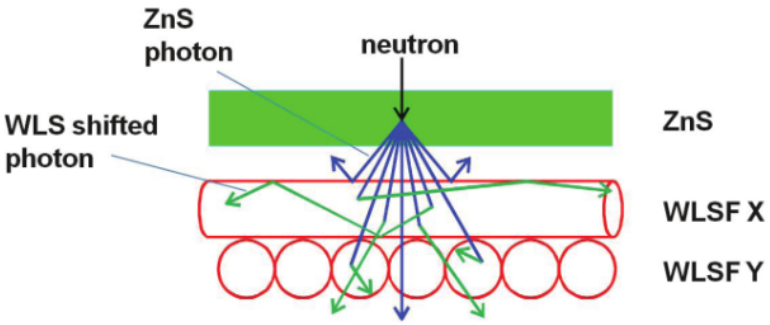

Figure 4.3: Schematics of a neutron detection in a neutron-sensitive scintillator detector with ^{6}Li/ZnS coupled via Wavelength Shifthing Fibres (WLS) to a PMT. Taken from [7].

4.1.3 Neutron Gaseous Detectors With Solid Converters

The working principle of a gaseous neutron detector with a solid neutron converter is similar to the one with a gas converter. In this case, a solid-state neutron converter material (usually ^{10}B or ^{157}Gd) is attached to a substrate inside the detector close to the gas medium, thus, the converter and the detection medium are separated. When a neutron interacts with the solid-state converter, it emits ionising particles. In the case of a ^{10}B converter, it emits an α particle and ^{7}Li (see Figure 4.4). One of these products might escape to the gas medium and ionise the detection medium. Similarly to the gaseous detectors with a gas converter, in the presence of an electric field, the electrons and ions drifting towards a certain structure of electrodes are subject to a gas amplification process.

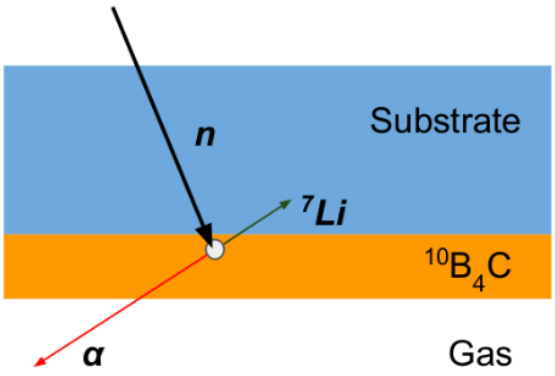

Figure 4.4: Schematic drawing of a neutron capture process inside the B_4C layer, which is deposited onto a substrate. After the neutron is captured by a boron atom, one of the resulting particles can escape to the gas medium and ionise it.

$^{10}B_4C$ proves to be a promising substitute to ^{3}He due to its natural abundance, chemical and practical features [8], and is the preferred choice for the future most advanced detectors at the ESS [61]. Several $^{10}B_4C$-based detectors for large ($\approx$ 10 to 50 m^2) [62], and medium ($\approx$ 0.2 to 2 m^2) [63] size areas have already been developed. They show good detection efficiency, but their

spatial resolution is limited to a few millimetres, which is still too far from the high resolution domain.

4.2 The ^{10}B-RPC

A ^{10}B-RPC is an RPC where a thin layer of an ^{10}B-based neutron converter is deposited on the inner surface of the cathode plate facing the gas gap, as shown in Figure 4.5. The construction is identical to that of a standard RPC (see Figure 3.4), except that the cathode electrode in glass is replaced by an aluminium plate. The pairing of a resistive plate with a metallic one leads to a hybrid configuration that keeps all the functionalities of the RPCs since at least one of the electrodes is resistive. The Aluminium plate is coated with a thin film of $^{10}B_4C$ on the surface facing the gas gap. It is this converter layer that makes the detector sensitive to neutrons, via the following neutron capture reaction $^{10}B(n,\alpha)^7Li$ capture reaction (see Table 4.1). If the converter layer is thin enough, one of the reaction products (α and ^{7}Li), that are emitted isotropically in opposite directions, can escape into the gas gap and generate primary ionisation (a certain number of electron-ion pairs). Then, the drift of the electrons towards the RPC anode under a high-strength electric field undergoes to a Townsend avalanche process. The electron avalanche is accompanied by the induction of charge signals in the pickup electrodes, signalling the detection of a captured neutron.

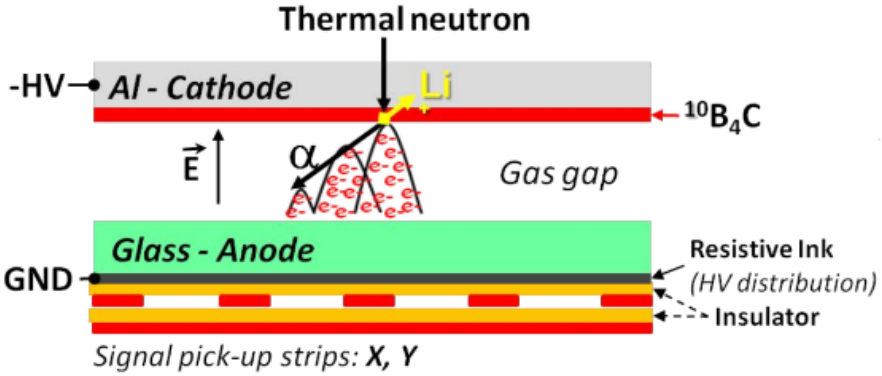

Figure 4.5: Conceptual design of a ^{10}B-lined hybrid RPC. The metallic cathode, made of, e.g., aluminium, is coated on the side facing the gas gap with the neutron converter layer.

The aluminium was chosen by three main reasons: the coating of aluminium with high quality $^{10}B_4C$ thin films has already been established [8]; aluminium can be used in relatively thin sheets (up to 0.3 mm) while maintaining good flatness; neutron absorption and scattering by the aluminium can be kept at acceptable levels.

Since the cathode is metallic, one of the challenges of a hybrid ^{10}B-RPC is the fact that the

both XY coordinates have to be read from the anode side, and this is contrary to what happens for the simpler case of the standard RPC, in which one of the XY coordinates is read from the anode side and the other from the cathode side. To solve this, it is adopted for the 2D readout, signal pickup electrodes consisting of two adjacent arrays of parallel and mutually orthogonal Copper pickup strips engraved on a thin double-layered PCB. The geometry of both X and Y arrays of strips (pitch and width) has to be optimised in order to achieve fair signal sharing between both strip-arrays.

A more attractive design for a ^{10}B-RPC is the one shown in Figure 4.6, which mirrors the single gap ^{10}B-RPC of Figure 4.5, in the plane of the cathode. In this arrangement, the metallic cathode is shared by the two adjacent resistive anode plates, creating two gas gaps. This configuration is called the ^{10}B double-gap RPC, and requires lining the cathode with a neutron converter on both sides.

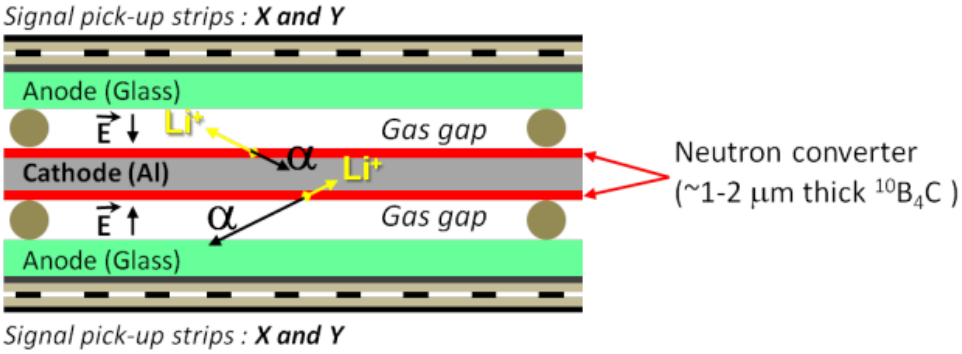

Figure 4.6: Double-gap RPC configuration: a single metallic cathode, shared by two anodes, is lined on both sides with a ^{10}B neutron converter.

The thickness of the $^{10}B_4C$ neutron converter layer is restricted. It cannot be too thick, otherwise, the resulting charged particles escape to the gas medium due to their small range inside the converter ($\approx$ 1.8 μm for ^{7}Li at 0.84 MeV and $\approx$ 3.5 μm for α at 1.47 MeV [64]). However, it cannot be too thin since to achieve a capture probability greater than 80%, the $^{10}B_4C$ path should be larger than $40\mu m$ for neutrons with $\lambda = 1.8$ Å. This restriction sets a trade-off between the probability of the neutron being captured and the probability of the products escaping to the gas, limiting a single layer of $^{10}B_4C$ neutron converter layer to a thickness of around 1-2 μm and detection efficiency in the range between 2% and 10%.

4.3 Multilayer Architecture

One approach to solving the detection efficiency challenge is by stacking several RPCs on top of each other, which is known as a multilayer. In this configuration, the total detection efficiency

is the sum of the contributions of all ^{10}B-RPCs individual modules, significantly improving the detection efficiency achieved. Stacking ^{10}B double-gap RPCs provides certain benefits over stacking single-gap ones. This configuration reduces the amount of material in the neutron path and simplifies electrical insulation by applying high voltage (HV) to the cathodes and keeping the anodes that face the signal pickup electrodes grounded.

The cathode signals are used to identify the neutron capture along the beam direction, and for timing proposes, allowing to determine the neutron TOF. Another advantage of a multilayer detector is that the counting rate capability increases with the number of RPCs in the stack.

The multilayer architecture also enables the construction of detectors with a modular design, by employing two types of independent building blocks: the double-gap RPC blocks and signal pickup electrode blocks. This feature is very advantageous for the mass production and maintenance of the detectors.

Like other types of detectors based on multilayer configurations have a common disadvantage: they are more sensitive to gamma rays and neutron scattering than single-layer ones due to the increased material budget.

Chapter 5

The nRPRC-4D Detector Concept

RPCs are well-known for their unprecedented fast timing capabilities (sub-ns scale). Therefore, the next significant stride in the development of the thermal neutron detection technology involving RPCs is to explore their three-dimensional readout and timing capabilities in a neutron detector. Once demonstrated, ^{10}B-RPCs would be suited for applications such as, e.g., TOF neutron diffraction and reflectometry, and energy-resolved neutron imaging, requiring submillimetre spatial resolution and sub-μs time resolution.

Based on the ^{10}B-RPC detection technology, a new position-sensitive neutron detector concept with four-dimensional readout capability (XYZ and time), named nRPC-4D, is presented. The nRPC-4D detector concept consists of a stack of RPCs with cathode plates lined on both sides with a $^{10}B_4C$ thin film, organised in a multilayer architecture (described in section 4.3).

The nRPC-4D concept is conceived in such a way that makes the construction and maintenance of a detector very straightforward. Its basic building block consists of a standalone and versatile detection module formed by a double gap hybrid ^{10}B-RPC. High detection efficiency for thermal neutrons with normal incidence to the planes of $^{10}B_4C$ layers is achieved by the several RPCs stacked. The needed number of ^{10}B-RPCs in the stack will depend on the specific detection efficiency requirements and on the range of neutron wavelengths considered for a given application. For a stack of ten ^{10}B-RPCs, it is expected to reach a detection efficiency of about 50% for neutrons with a wavelength of 4.7 Å.

Due to the high timing resolution of the RPCs [65] (below 100 ps for minimum ionising particles, MIPs) and the short neutron flight time through a layer of $^{10}B_4C$ of around 1 μm thick is approximately 1 ns, it is expected that an nRPC-4D detector can achieve an intrinsic timing resolution on the order of nanoseconds in measuring the neutron time-of-flight.

5.1 The Standalone ^{10}B-RPC Detection Module

A ^{10}B-RPC detection module consists of a double gap hybrid RPC composed of two float glass anode plates and an aluminium cathode in between them. As it can be seen in Figure 5.1, showing a schematic drawing of a detection module, all plates are parallel to each other and kept separated by monofilament spacers, defining gas gaps with a uniform width. The cathode plates are coated on both sides with a $^{10}B_4C$ layer of approximately 1 μm (^{10}B enrichment level $> 97\%$). The $^{10}B_4C$ coatings are done using the magnetron sputtering technique, proven to provide stable adhesion and good radiation hardness for $^{10}B_4C$ thin films [8].

Facing both anode plates is a flexible PCB (FPCB) with a thickness of 25 μm that holds two sets of parallel copper strips (18 μm thick, 0.3 mm wide, with a 1 mm pitch) on either side, with the two sets of strips oriented orthogonally to each other. These arrays of signal pickup strips are used to read the X and Y coordinates of the neutron capture event position in the detector. The Z coordinate and the timing are given by the signals induced on the cathode. It should be noted here that the induced signals are formed by two components: a fast one induced by the fast drift of electrons in the ^{10}B-RPC gas gap and a slower one induced by the drift of the ions. For timing purposes, the former is used.

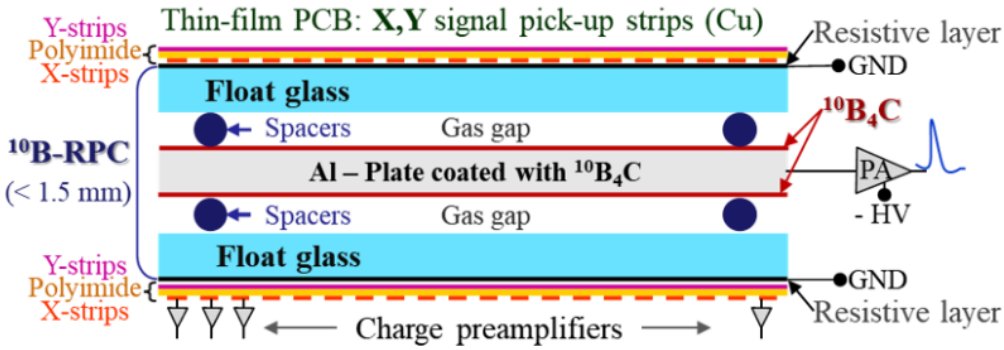

Figure 5.1: Schematic drawing (dimensions are not to scale) illustrating the standalone ^{10}B-RPC design.

5.2 The nRPC-4D Multilayer Detector

In Figure 5.2 it is shown a schematic drawing of the layout of the nRPC-4D detector. There are ten ^{10}B-RPC detection modules stacked on top of each other with signal readout FPCBs inserted in between them, another one on the top side of the first module and another on the bottom side of the last module.

In this arrangement, adjacent gas gaps of neighbouring ^{10}B-RPC modules share the same

XY arrays of signal pickup strips in the FPCBs used to read the x- and y-coordinates of the neutron events.

The cathodes of the ten ^{10}B- RPC modules are read individually by fast amplifiers. This allows us to identify the position where a detected neutron capture occurred along the stack (z-coordinate) and provides the timing signal (fast component of the induced signal) to trigger the data acquisition system (DAQ) and determine the neutron TOF.

As the number of ^{10}B-RPC modules is large, the number of signal pickup strips and consequently, the number of electronic channels necessary to individually read all the strips is not manageable. For instance, considering a pitch of 1 mm for the strips, and an detector active area of about 200 mm x 200 mm, 400 channels are needed per FPCB (200 for each of the X and Y coordinates). Therefore, considering a detector with ten ^{10}B-RPC modules (see Figure 5.2), 4400 (11 x 400) electronic channels would be needed to readout the entire detector.

To address this, the individual strips of each coordinate array, with the same index, are interconnected and readout using the same electronic channel. By using this approach, the number of electronic channels is decreased by a factor of N+1, where N is the number of double-gap RPCs in the stack.

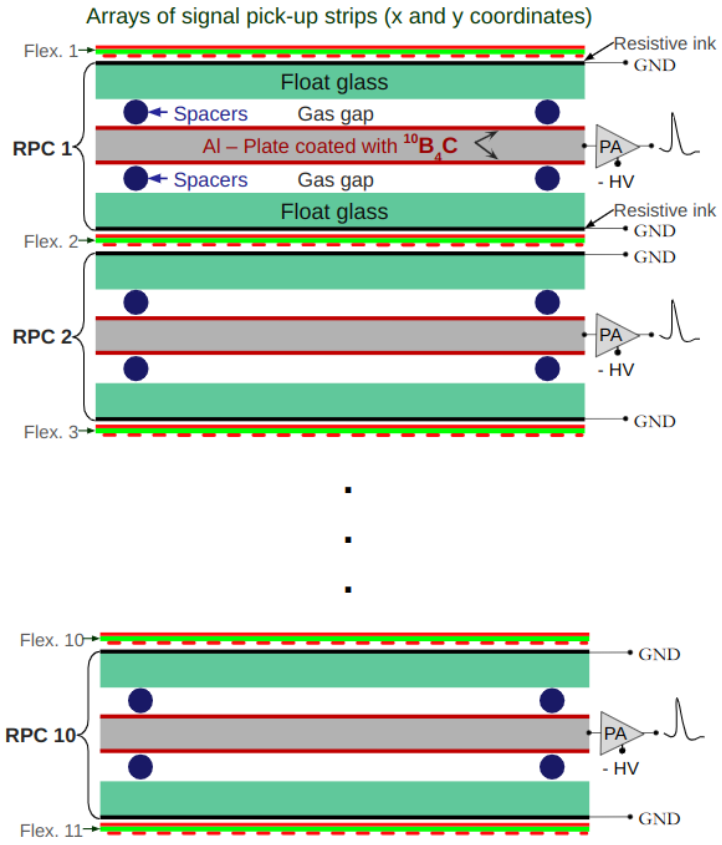

Figure 5.2: Schematic drawing of the nRPC-4D detector showing how the stack is formed, with ten ^{10}B-RPC modules being displayed.

As a neutron event produces ionisation only in one gas gap, the triggered ^{10}B-RPC module in the stack is known once the cathode with a signal is identified. However, this still leads to an uncertainty in the Z coordinate measurement since the side of the cathode of the respective ^{10}B-RPC where the neutron was captured cannot be directly identified.

This ambiguity, in principle, can be solved by using FPCBs with strips of suitable geometry and installed as it is shown in Figure 5.2. The FPCB is oriented with the y-strips facing up and the x-strips facing down. In this way, for the upper gas gap, the x-strips are facing the anode plate, so they are closer, and the y-strips are further away from it. For the lower gas gap, the opposite occurs, and in this case, we have the y-strips closest to it. Therefore, when an event happens in the upper gas gap of any ^{10}B-RPC module, the y-strips are partially screened by the x-strips. As a result, the sum of the induced signals in the x-strips will be larger than for the y-strips. As explained before, the opposite occurs for the lower gas gap, where the sum of the signals induced in the y-strips will be greater than for the x-strips.

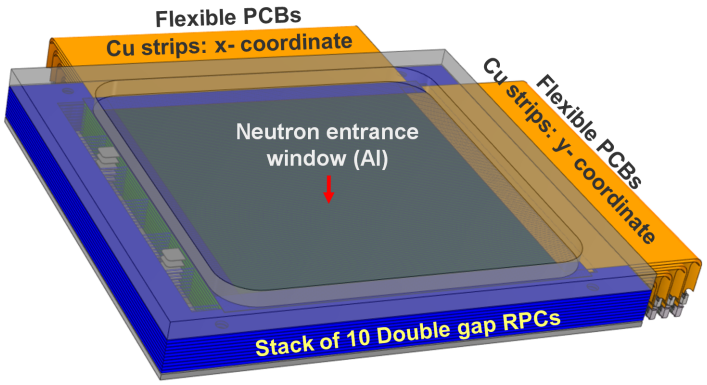

Figure 5.3: 3D view of the nRPC-4D detector prototype design, with a stack of ten $^{10}B_4C$-RPC modules.

5.3 Simulation-Based Optimisation of the Detector Design

One main objective of the simulation-based optimisation of the detector design is to define the optimal configuration of the detector aiming at the ns-scale timing resolution, spatial resolution of 0.1 mm, >50% detection efficiency, low gamma sensitivity ($< 10^{-6}$) and minimal background from neutron elastic scattering. The simulations were carried out using the Geant4 toolkit v10.7.2 [66] with ANTS2 v4.36 [67] as the front-end.

For the initial optimisation simulation, it was assumed a detector design similar to Figure 5.2, with ten ^{10}B-RPC detection modules (20 layers of $^{10}B_4C$) and11 sets of XY signal pickup units. This number of RPCs was chosen to achieve detection efficiencies of about 50% for thermal

neutrons. It was also assumed the same thickness for all o $^{10}B_4C$ layers, each with a 1.15 μm .

The ^{10}B-RPCs components have the following properties:

- 0.33 mm thick soda lime glass anodes;
- 0.3 mm thick cathodes made of 5754 aluminium alloy;
- $^{10}B_4C$ converters (^{10}B enrichment level of$\approx$ 97%) of 1.15 μm thicknesses;
- 0.28 mm wide gas gaps filled with R134a gas at atmospheric pressure;
- 25 μm thick flexible PCBs made of polyimide film with 18 μm thick copper layers on each side.

The primary neutrons were generated as a monochromatic pencil beam with a wavelength of 4.7 Å and normal incidence at the detector's centre. Typically, simulations were performed using 10^6 primary neutrons. A neutron was considered detected if the capture reaction products deposited at least 100 keV in the gas. This threshold value was selected to match the simulated and experimentally observed detection efficiency [68]. Figure 5.4 displays the respective simulated contributions of every ^{10}B-RPC modules to the detector's detection efficiency.

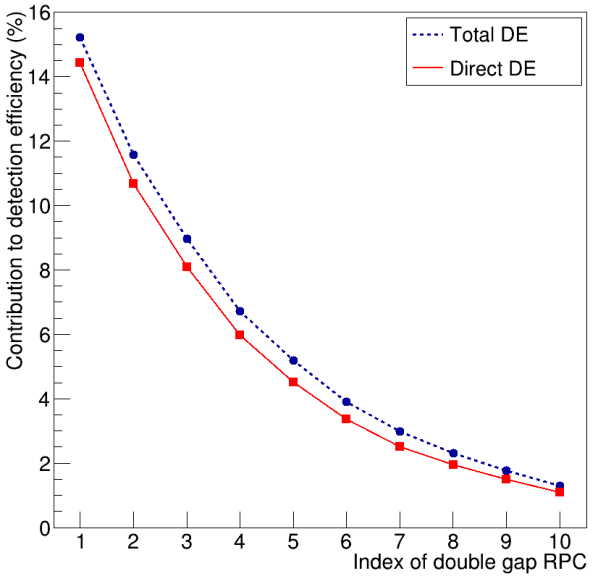

Figure 5.4: Contribution to the overall detection efficiency of each double gap RPC in the stack, with $^{10}B_4C$ layers of the same thicknesses (1.15 μm). The sum of all contributions adds up to a detection efficiency of 60.4%. The "direct DE" data show the detection efficiency excluding those neutrons which had prior elastic scattering.The lines are an eye-guide connecting the data points.

The "Direct DE" curve only accounts for the neutrons that were not scattered before detection, while the "Total DE" considers all neutrons, regardless of their prior interactions. By

summing up the contributions from each ^{10}B-RPC, the overall detection efficiency of the detector is 60.4%. It should be noted that each ^{10}B-RPC module attenuates the neutron beam intensity by the same amount along the stack, resulting in the ^{10}B-RPC further in the stack detecting less neutrons. This reduction of the neutron flux throughout the stack results in an unequal contribution of each ^{10}B-RPC to the total detection efficiency. The first ^{10}B-RPC seeing the neutrons has the highest contribution to the detection efficiency, which means it will reach its maximum counting rate limit earlier than the other ^{10}B-RPC.

Based on the above considerations, it is recommended to optimise the detector design using a procedure that not only maximises the direct detection efficiency, but also ensures an equal contribution to the counting rate from all ^{10}B-RPCs. As already mentioned before, the parameter that mainly affects the detection efficiency of each individual ^{10}B-RPC is the thickness of the neutron converter layer, so, an approach to equalise the contributions to the counting rate of each ^{10}B-RPC was to consider all with of $^{10}B_4C$ layers with different thicknesses. However, due to the practical considerations related to the deposition processes of the $^{10}B_4C$, it was decided to divide the RPCs into three groups of different thicknesses: RPCs indexes 1 to 3, RPCs indexes 4 to 7 and RPCs indexes 8 to 10.

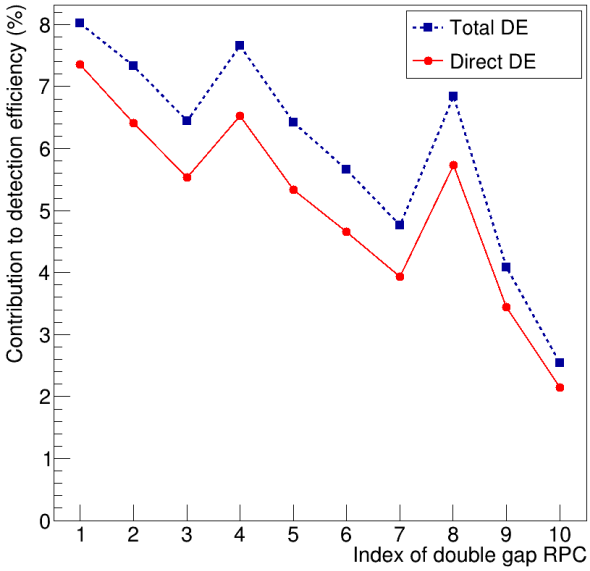

Figure 5.5: Contribution to the detection efficiency of each ^{10}B-RPC in the stack for the configuration with optimised thicknesses. The sum of all contributions adds up to 59.8% total detection efficiency. The "direct DE" data show the detection efficiency excluding those neutrons which had prior elastic scattering. The lines are an eye-guide connecting the data points.

This conditional optimisation was performed using the procedure described in [68] to find the three optimal thickness values. The determined optimal thickness values are: 0.4 μm to

RPC 1 to 3, 0.6 μm to RPC 4 to 7, and 2.2 μm to RPC 8 to 10. A second simulation of the detector was performed using the optimised thicknesses, all the other considerations remained the same from the previous simulation. The individual simulated contributions of each ^{10}B-RPC module to the detection efficiency computed using the optimised thicknesses are presented in Figure 5.5.

The overall detection efficiency is 59.8%, while the direct detection efficiency is 51.1%. It is observed a much more equal distribution of the contributions of each individual RPC for the overall neutron detection efficiency, and this in comparison to the detector configuration in which the thickness of the $^{10}B_4C$ layers are equal in all RPCs. The results of this study have already been published, for more details see [18].

Chapter 6

The nRPC-4D Detector Prototype

In the previous chapter, the nRPC-4D detector concept and the main results from the simulation-based optimisation procedure were discussed. This chapter reports on the next phase, the design and construction of a prototype for the proof of concept. The main objective is to experimentally demonstrate its feasibility and specifically to show that this new type of detector is capable of simultaneously providing the XYZ coordinates of the detected neutrons and of measuring their TOF.

The assembly procedures, as well as the details on the selected data acquisition system, waveform processing methods, and the algorithm for the discrimination between neutron events and background ones are discussed.

6.1 ^{10}B-RPC Detection Modules Construction

The most demanding aspects in assembling a ^{10}B-RPC module are: (1) establish a method to maintain a uniform gas gap width between the cathode and anode plates and hold them in a standalone module; (2) coat the aluminium cathode plates with the $^{10}B_4C$ converter; (3) ensure the distribution of the electrical potential across the entire external active area of the glass anode plates; (4) install the external signal pickup electrodes. At the same time, the design must result in a mechanically stable and easy-to-assemble detection module.

The first aspect was addressed by designing a frame in fibreglass (FR4) with a geometry that allows to fix monofilament spacers (PEEK), the cathode and anode plates (see Figure 6.1). Four holes are also provided in the corners of the frame to align the module in the stack by using pillars.

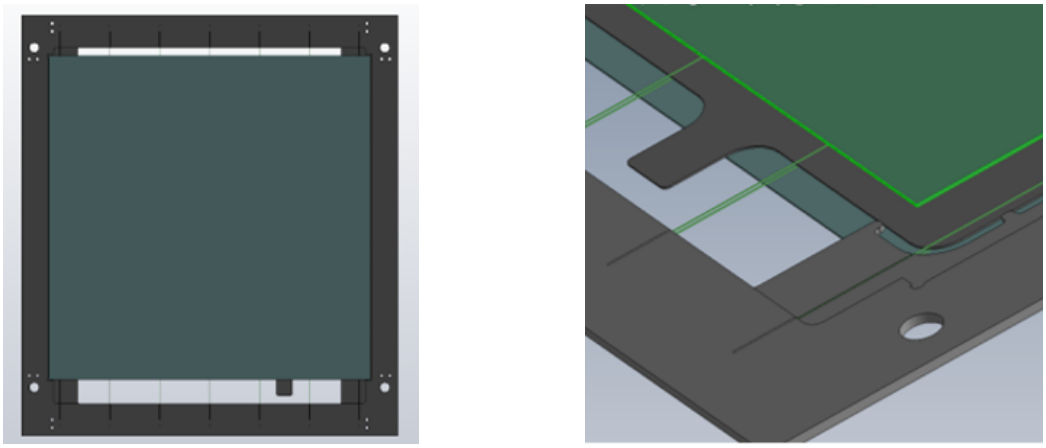

(a) (b)

Figure 6.1: (a) Top view of the design of the frame which holds the monofilament spacers (0.28 mm diameter), as well as the cathode and anode plates of the ^{10}B-RPC module. (b) A closer view, showing in detail the tip at the cathode (grey colour) used to apply the high voltage and the monofilament spacers (green colour). The recess in the frame that keeps the glass plates aligned is also visible.

The cathode plates of 0.3 mm thick aluminium (alloy 5754) were coated on both sides with high quality $^{10}B_4C$ thin films using DC magnetron sputtering at the ESS detector coatings workshop (see Figure 6.2). A set of plates necessary to assemble a detector with 10 detection modules was ordered. The thicknesses of the $^{10}B_4C$ layers on each plate were defined according to the results from the simulation (see section 5.3).

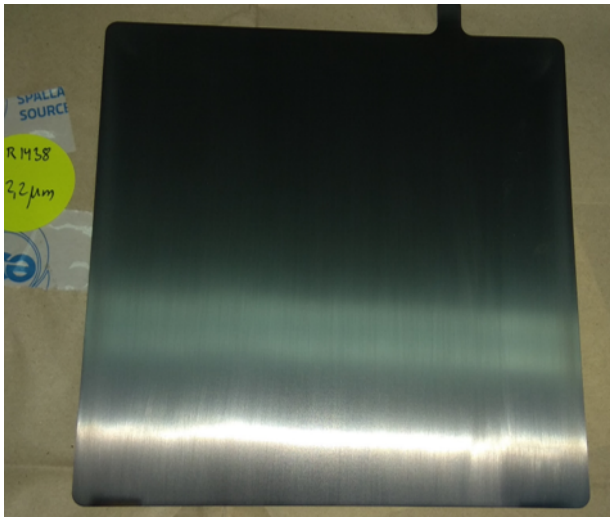

Figure 6.2: 0.3 mm thick aluminium plate (alloy 5754) with an area of 190 mm × 190 mm, coated with a 2.2 μm thick layer of $^{10}B_4C$ on both sides.

Due to the high electrical resistivity of the float glass ($\approx 10^{12}$ Ωcm) used for the anodes, a layer of material with lower resistivity needs to be deposited on top of the glass to ensure a uniform potential across the entire surface. For this purpose, a 0.1 mm thick layer of ink

(composition not disclosed by the manufacturer) with a surface resistivity of $\approx 10^8\ \Omega/\square$ was lined to the external surface of the glass defining the active area (see Figure 6.3).

Figure 6.3: 0.3 mm thick float glass plate with an area of 200 mm $\times$ 200 mm, lined with a $\approx$ 0.1 mm thick layer of resistive ink. The ink layer is on the back side of the plate (as evidenced by the reflection of light). To match the area of the aluminium cathode plate, the lined area is only 190 mm $\times$ 190 mm. The white area in the top-right corner is a reflection of the lamp.

The XY position of a detected neutron is inferred from the charge signals induced in the ^{10}B-RPC. To read these signals, it was opted for arrays of copper strips parallel to each other to be installed on the external surface of the anodes: one array for reading the x-coordinate and another orthogonal to the first for reading the y-coordinate. As the objective was to have a structure with signal pickup strips independent of the detection module, we chose to implement the XY strip arrays on a very thin flexible polyimide PCB (FPCB) of 25 μm thick, with an array on each face. The layout used to order the manufacturing of FPCBs is shown in Figure 6.4 (1 mm pitch, 0.3 mm wide copper strips).

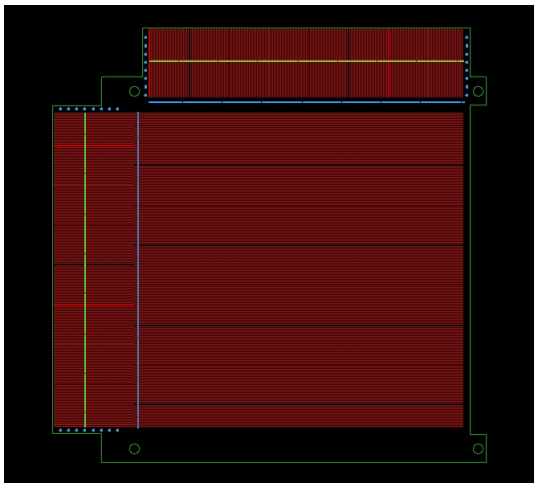

Figure 6.4: Schematics of the FPCB with the XY strip arrays: one on each side of polyamide film (25 μm thick) and orthogonal to each other.

The initial step in the detector assembly is the construction of the individual ^{10}B-RPC modules and the interconnection of the signal pickup strips of each coordinate array with the same index.

The assembly of the detection ^{10}B-RPC modules starts by inserting the 0.28 mm diameter PEEK spacers into the FR4 frames (see Figure 6.5a). Next, the aluminium cathode plates are placed in between the spacer as shown in Figure 6.5b. Then, an anode plate of float glass is placed on the top and another on the bottom of the cathode, with the spacers defining the gas gap (see Figure 6.5c). Both plates are held to the 1.5 mm thick FR4 frame with an adhesive film.

To build the prototype, ten ^{10}B-RPC modules were assembled: modules 1 to 3 have a $^{10}B_4C$ layer thickness of 0.4 μm, modules 4 to 7 have a $^{10}B_4C$ layer thickness of 0.6 μm and modules 8 to 10 have a $^{10}B_4C$ layer thickness of 2.2 μm.

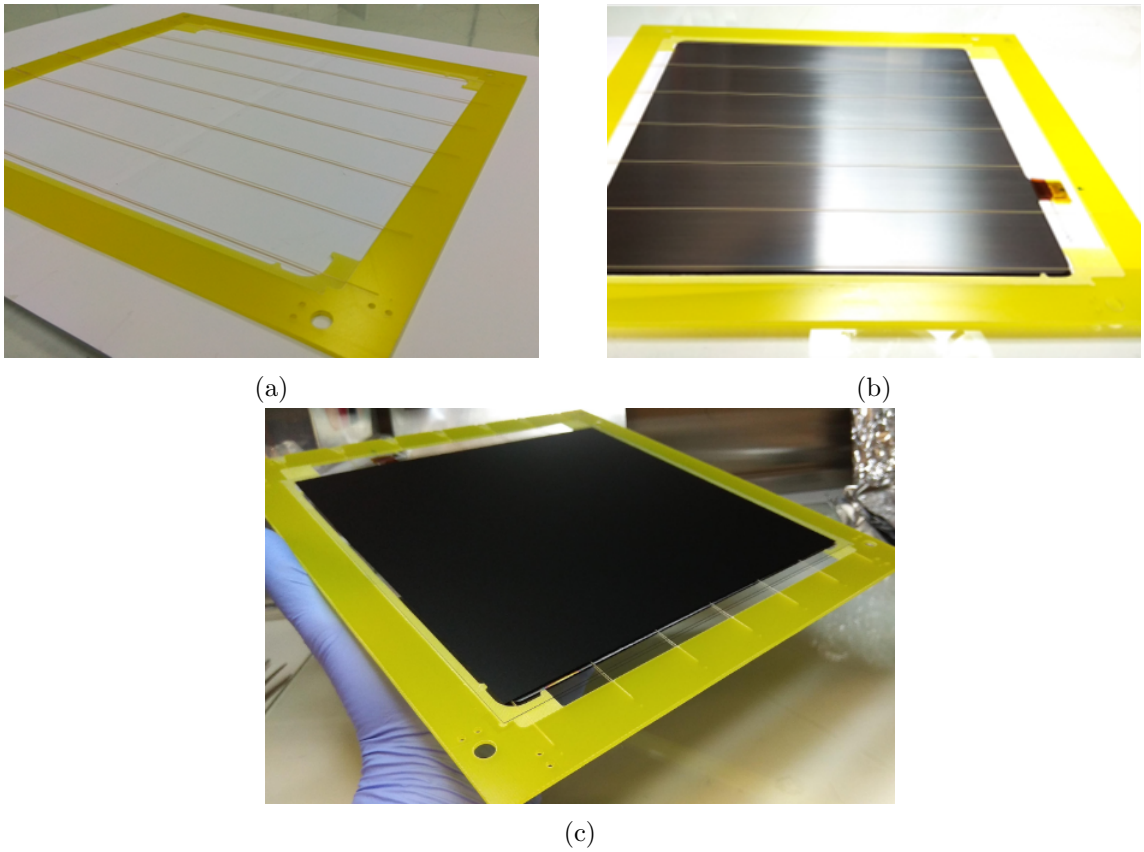

(a) (b)

(c)

Figure 6.5: (a) 1.5 mm thick FR4 frame. (b) Aluminium cathode plates (0.3 mm thick) coated with $^{10}B_4C$. (c) ^{10}B-RPC module. We can see the ink layer lined on the external side of the glass plates (black colour) for the HV distribution.

As described above, the FPCBs feature two arrays of parallel 25 μm thick and 0.3 mm wide copper strips with a pitch of 1 mm, separated by 25 μm thick polyamide film (see Figure 6.6a and 6.6b). The array of strips on the bottom of the FPCB, designed to readout the X coordinate, are

oriented orthogonally to the array strips located on the top, used to readout the Y coordinate of the event. As in Chapter 5.2, the individual strips of each coordinate array with the same index are designed to be interconnected and readout using the same electronic channel. To do this interconnection, an Anisotropic Electrically Adhesive Transfer Tape Type 9703 from 3M (ACF) [69] was used so we could keep planarity and avoid the need to solder thousands of strips (see Figure 6.6c and 6.6d).

The FPCBs function as an independent structure, which, for example, allows their geometric parameters to be changed and to be replaced without having to disassemble the ^{10}B-RPCs. The FPCBs are assembled in direct contact with the resistive ink that covers the outer surface of each float glass anode plate, and in between each pair of the neighbouring ^{10}B-RPCs modules, as well as before the first and after the last ^{10}B-RPC module of the stack (see Figure 5.2).

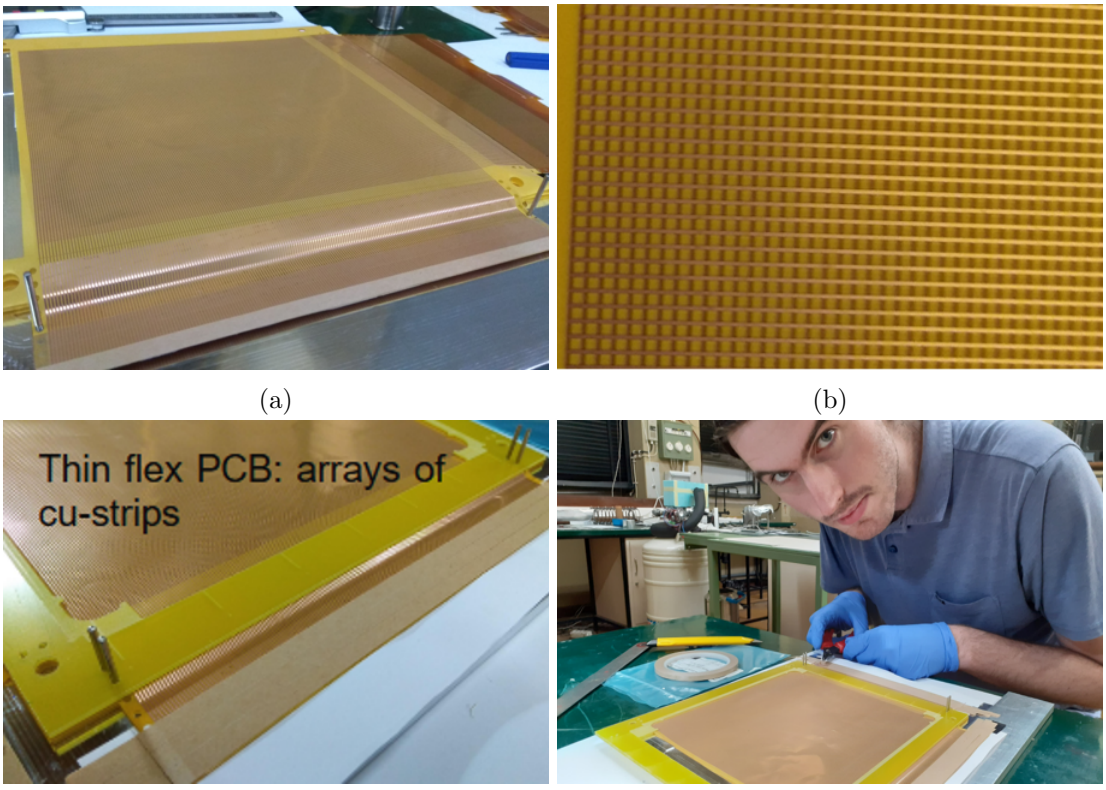

(a) (b)

(c) (d)

Figure 6.6: (a) Thin Flex PCB with the arrays of XY signal pickup strips. (b) Zoom of the photo showing the copper strips. (c) ACF applied on the PCB. (d) Electrical contact with strips being made with an ACF.

6.2 Detector Prototype Assembly

The detector's enclosure (see Figure 6.7b) consists of an aluminium frame, 450 mm long, 450 mm width, and 50 mm high, with one side faced by an aluminium neutron entry window. To

minimise the neutron scattering, the window is only 0.2 mm thick in the area overlapping the detector active area. Both the frame and the window were manufactured at the LIP-Coimbra mechanical workshop.

The frame has on one of the sides two ports for the gas inlet and outlet and on the opposite side the feedthroughs for electric connections (SHV and MMCX connectors). The gas tightness of the enclosure is achieved by two neoprene O-rings, placed in the machined grooves on both top and bottom sides of the aluminium frame (see Figure 6.8a).

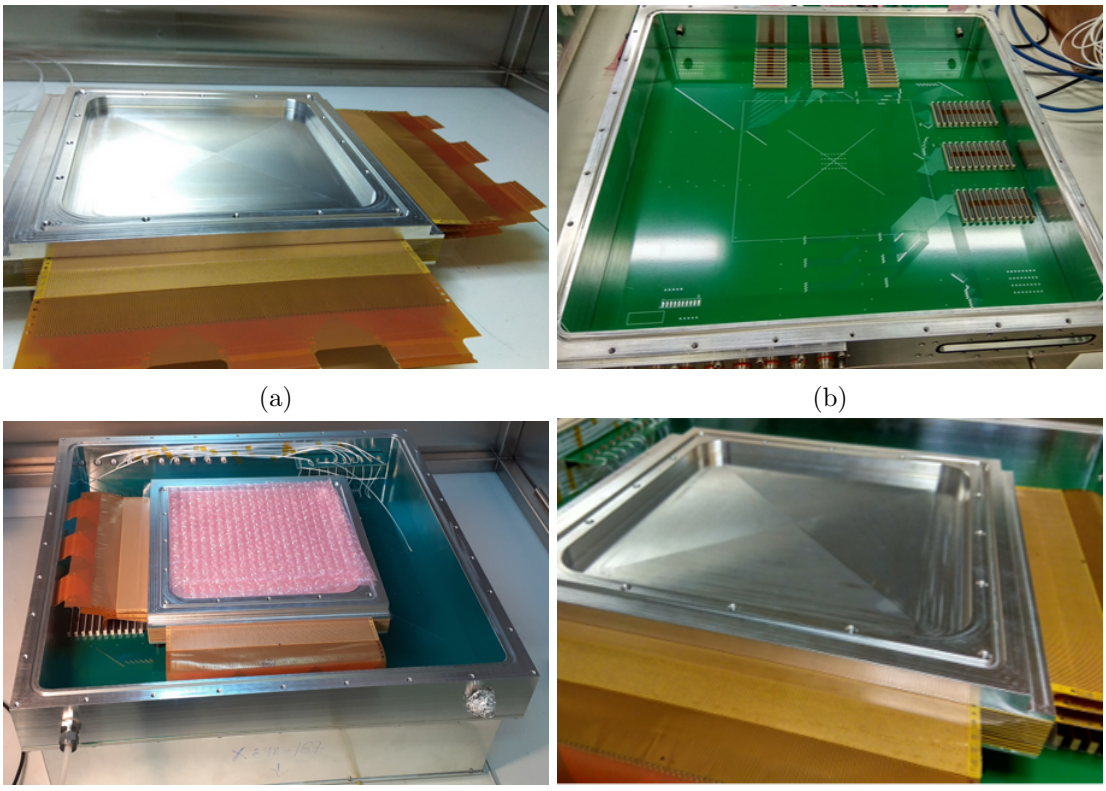

(a) (b)

(c) (d)

Figure 6.7: (a) The stack of ten ^{10}B-RPCs modules. (b) Inside view of the detector aluminium gas chamber before the ^{10}B-RPC stack is installed. (c) Inside view of the detector aluminium gas chamber during installation of the ^{10}B-RPC stack. (d) Stack of the ^{10}B-RPCs already installed inside the detector chamber with the FPCBs plugged into the ZIF connectors.

The back side of the gas-tight chamber consists of a 5-layer signal extraction PCB (Figure 6.7b) with copper tracks to drive the signals from the 2 x 192 signal pickup strips to the front end charge sensitive preamplifiers. A set of ZIF connectors from Amphenol [70] is installed on the PCB surface inside the chamber in order to plug the Flex PCBs that make the electrical contact with the x- and y-pickup strips.

On the outside of the detector chamber, the signal extraction PCB is equipped with a set of header-type connectors to plug the front end electronics boards (see Figure 6.8b). Both the signal extraction PCB and the flexible PCBs were designed by us at LIP-Coimbra, and

manufactured by the Multi-CB company [71].

Each RPC module is 1.56 mm thick, and together with the spacers and the FPCBs, the total thickness of the stack containing ten ^{10}B-RPC modules is ≈16 mm. The stack (Figure 6.8b) is mounted inside the detector gas chamber directly under the neutron entrance window and is kept aligned by 4 pillars. The ^{10}B-RPCs are numbered from 1 to 10, with the ^{10}B-RPC number one (^{10}B-RPC1) facing the neutron entrance window on the front face of the detector enclosure. Inside the detector chamber, the interconnected FPCBs are inserted into ZIF connectors that make contact with the front-end electronic boards (see Figure 6.7c and 6.7d). All strips are grounded through 10 MΩ resistors.

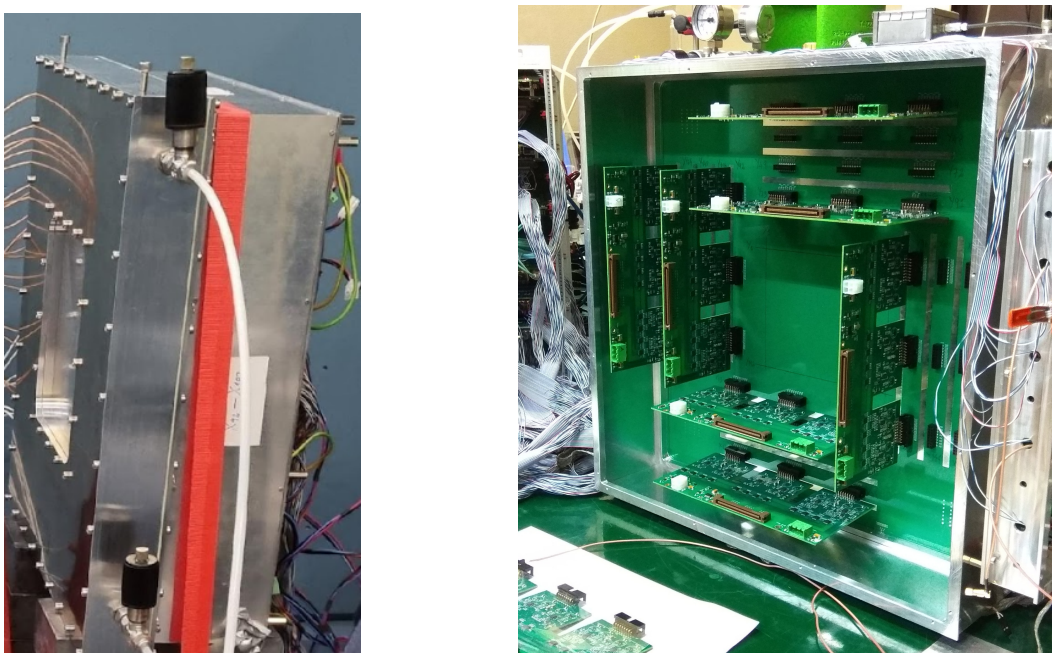

(a) (b)

Figure 6.8: (a) Side view of the detector with an aluminium entrance window and the gas inlet. (b) The back side of the detector shows the external side of the signal extraction PCB, where the set of header type connectors for connecting the front end electronics boards can be seen.

During the tests, the detector is operated in the avalanche mode, with the working gas R134a ($C_2H_2F_4$) at atmospheric pressure and room temperature (≈ 25º C), and maintaining a flow rate of approximately 2 cc/min. The detector is polarised with a negative voltage applied to the cathodes using a HV power supply (model N471A from CAEN).

6.3 Electronic readout

To readout the nRPC-4D detector prototype it was chosen to use the front end electronics developed by the LIP RPC group [44] and a data acquisition system (DAQ) based on the

Triggered-Readout-Board (TRB) family from GSI [72] which contains a versatile FPGA-platform based on TDC-in-FPGA technology with 10 ps precision, front-end electronics and a complete system of data acquisition and control software.

The front end electronics consists of two components. First, the timing/trigger amplifier card (2 channels) is used to read the fast component of the cathode signal (see Figure 6.9a). It generates the trigger signal for the DAQ. The DAQ registers the cathode trigger states, which are used to identify the RPC module where the neutron event has occurred. The threshold of each channel can be individually adjusted. The second component is formed by eight 24-channel custom charge amplifier cards with an integration time constant of 20 μs and a gain of 250 mV/pC (see Figure 6.9b). They are used to read both the slow component of the cathode signal and the x- and y-pickup strips signals, which are then recorded by the DAQ.

(a)

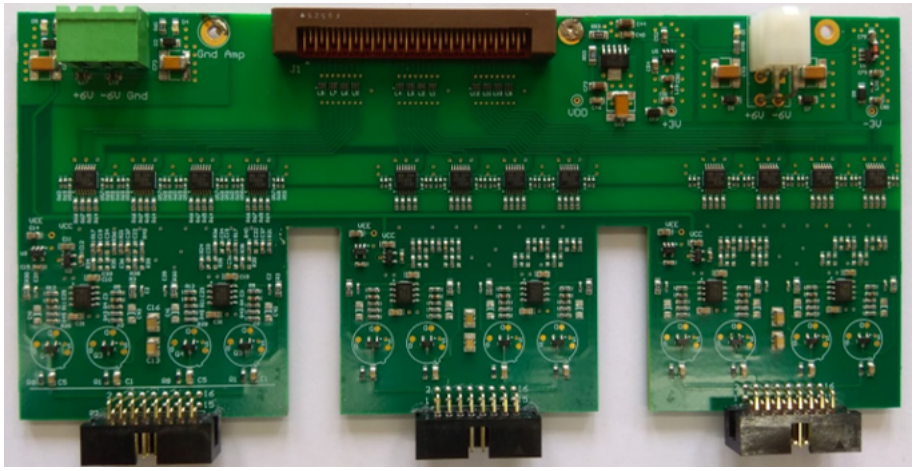

(b)

Figure 6.9: (a) Timing/trigger amplifier cards [44], assembled in a metal case to shield against electromagnetic noise. When the electronic component of the signal from the cathodes exceeds the threshold, a digital LVDS signal is generated. (b) Front end electronics card with charge amplifiers [44].

The DAQ is equipped with ADC AddOns comprising four 48-channel 12-bit streaming ADCs with 40 MHz sampling rate and in-board digital pulse processing (Figure 6.10). In total, only 4 ADC AddOn cards were used, corresponding to 192 DAQ channels available for the prototype

readout. Figure 6.11 shows a general view of the entire detection system already assembled.

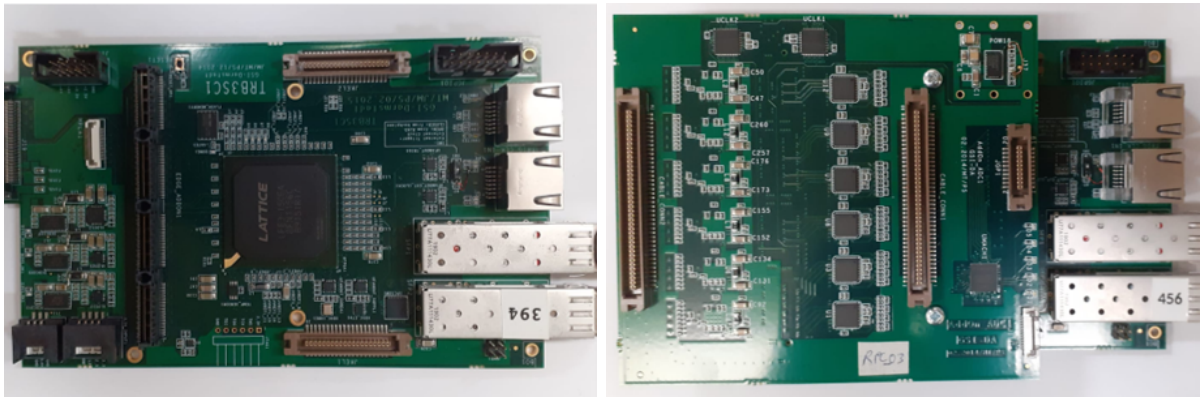

(a) (b)

Figure 6.10: (a) TRB3 board. (b) ADC addon installed on the TRB3 board [72].

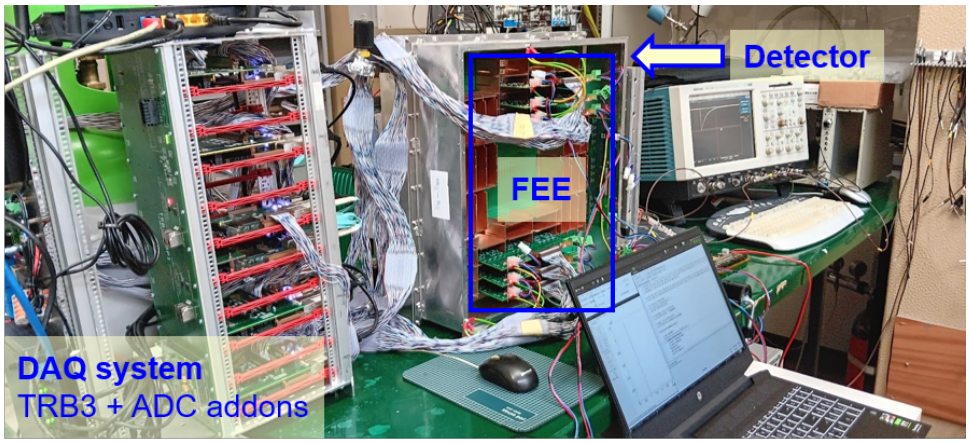

Figure 6.11: Detector prototype already assembled and connected to the DAQ system.

Ten channels are used for the cathodes readout, the remaining 182 channels are allocated for the readout of the signal pickup strips: 86 for the X coordinate and 86 for the Y coordinate. The pickup strips cover a total area of 187 mm x 187 mm. However, due to the limited number of available front end electronic cards and, consequently, the limited number of DAQ channels, the resulting maximum readout area is only 86 mm x 86 mm. Since we want to be able to access the entire active area of the detector for its characterisation, the front end cards can be moved in between different connectors for both X and Y coordinates, changing the area to be readout. To establish the correspondence between the front-end electronic card positions and the detector area to be readout, I created a mapping algorithm. The algorithm associates each array of strips in its corresponding connector with a unique index value. It also does the same for each array of DAQ channels in its corresponding front end electronics card. Therefore, by giving an input that corresponds to a given index of a card inserted into a connector with a certain index, it is possible to establish the connection between the array of DAQ channels and

the array of pickup strip positions, giving, as an output, the corresponding detector area being readout. The algorithm also provides the user with warnings if the front end cards are inserted incorrectly (e.g., if there are no cards connected to the cathode channels). The algorithm was implemented in the frame of the data analysis software used by the group and it is written in the JavaScript programming language. The developed code is listed in Appendix A.

6.4 Data Acquisition and Processing

6.4.1 Waveform processing

The DAQ system has been configured to record waveforms of the induced charge signals on the strips and cathodes with a duration of 4 μs and 20 samples (sampling time of 200 ns). It should be noted that the DAQ allows recording waveforms with a sampling time of 25 ns, however, in our case we chose to use a downsampling of 8 to reduce the data size. A typical example of the waveforms registered for a neutron event is shown for both the x- and y-strips as well as the cathodes in Figure 6.12. The recorded data is saved into binary files.

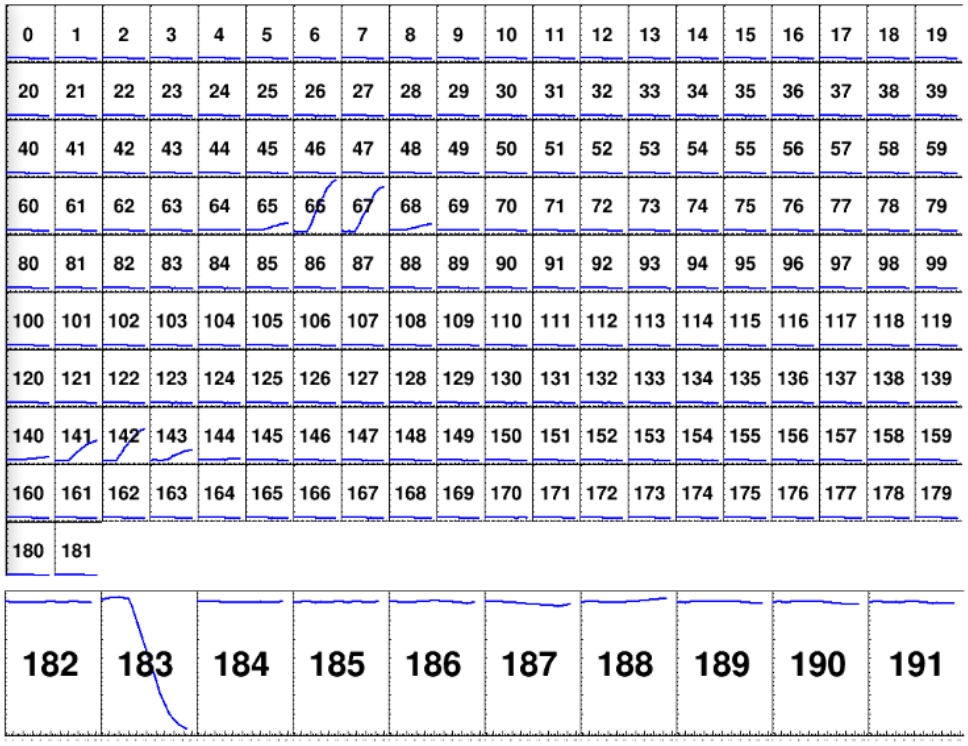

Figure 6.12: Waveforms of a neutron event for the x-strips (index 0 to 90) and y-strips (index 91 to 181) and also for the cathode channels (index 182 to 191).

The first step in the data analysis of a registered event is to link each strip and cathode with a signal value: the amplitude of the corresponding waveform. This information is then used to

discriminate between neutron events and background noise, position reconstruction.

There are three steps in the procedure used to obtain the amplitude of each waveform. Firstly, the waveform is smoothed using the adjacent averaging method, which uses three data points around a value to calculate its average. Secondly, the baseline, which corresponds to the logical zero of the sampled data, is calculated by averaging the first 5 samples of the waveform. Lastly, the baseline value is subtracted from the signal value for each strip at the time of the largest maximum amplitude signal. Figure 6.13 shows an example of a raw waveform on the left and the same waveform on the right after smoothing with adjacent averaging.

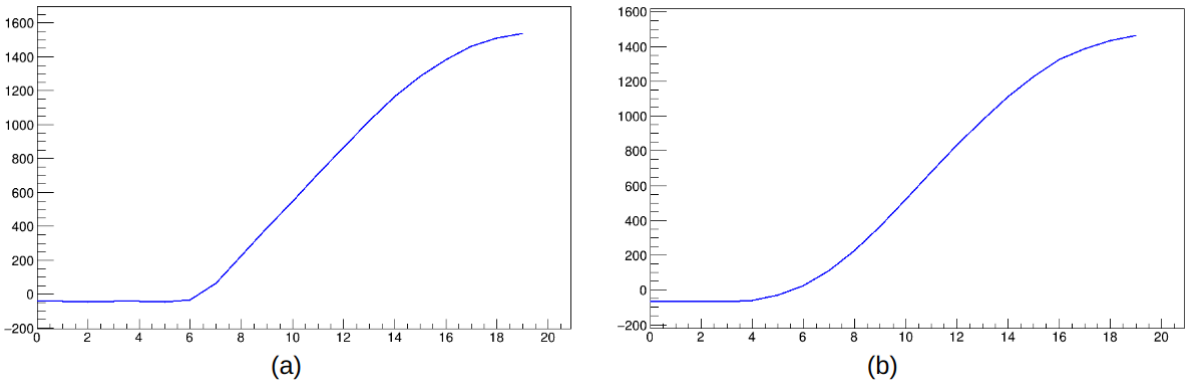

Figure 6.13: Example of the waveforms for one of the strips: (a) raw data; (b) processed waveform.

6.4.2 Neutron Event Selection

In order to discriminate the neutron events from the background ones, I have developed an algorithm that applies a set of criteria to the processed experimental signals, which have to be fulfilled for an event to be recognised as a valid neutron event. Those criteria are:

1. A neutron event should simultaneously induce signals above a defined threshold on a specific number of x- and y-pickup strips and in only one of the cathodes;

2. The induced signals above the threshold should be present in more than one consecutive pickup strip, in a group by their index. Such groups are named clusters: for instance, in Figure 6.12, the indexes from 65 to 68 and from 141 to 143 form two clusters, respectively for the X and the other for Y coordinates. Only clusters having at least two strips with signal above the threshold are validated as being neutron events;

3. Events with more than one cluster in X or Y direction are excluded, as it is not possible to establish a correspondence between the clusters in the two coordinates in order to reconstruct the neutron event position;

4. Only clusters that present a distribution for signal amplitude with just one peak are considered valid for neutron events.

The algorithm was also implemented in the frame of the data analysis software used by our group, and it is written in the JavaScript programming language. The developed code is listed in Appendix B.

Chapter 7

Prototype Tests on a Neutron Beam

After being assembled, preliminary tests of the prototype on a neutron beam were performed at the SINQ neutron spallation source at PSI. It marked the first time that both the nRPC-4D prototype was exposed to neutrons and the timing capabilities of a ^{10}B-RPC were put to the test. Due to limitations of beam time availability, the experimental tests described in this chapter were performed during a very short time interval of two and half days. This fact limited the number of experimental tests we were able to perform.

In the first two days the experiments were conducted at the beamline of the NARZISS reflectometer. The beamline provides a monochromatic beam with a 4.94 Å wavelength at low intensity. The experiments aimed to characterise the detector's response of the ^{10}B-RPCs modules to thermal neutrons and verify the shape and consistency of the charge spectra, obtained from the signals induced on the cathodes, for different irradiated locations of the detector active area.

In the last half day, the experiments were performed at the Beamline for Neutron Optics and Other Approaches (BOA), which provides a high-intensity quasi-continuous white beam, covering a wide range of neutron wavelengths. The tests at BOA had two objectives: firstly, to evaluate the timing capabilities of the detector for TOF experiments by measuring the neutron time of flight and calculate its wavelength spectrum and secondly, to validate the novel method described in Chapter 5 for identifying the $^{10}B_4C$ layer where the detected neutron was captured.

7.1 Experimental Setup at NARZISS Beamline

In the neutron beamline of the NARZISS reflectometer, two tests were conducted in order to do a preliminary characterisation of the detector response to thermal neutrons. For these tests, two different experimental setups were assembled.

The first experimental setup is illustrated in Figure 7.1. The neutron beam was collimated by three slits placed along the beamline, all having an aperture area of 1 mm x 10 mm (width x height). The slits S1, S2 and S3 were placed at the distance of 210 cm, 146.5 cm, and 14 cm, respectively, from the detector. The detector window was oriented normally to the beam.

Throughout these measurements, the detector was not connected to the DAQ system described in chapter 6. Instead, the cathode signal was fed to an ORTEC preamplifier 142AH (sensitivity of ≈ 0.7 V/pC). After amplification the signal was shaped using a linear amplifier and recorded using a multichannel analyser (Amptek's MCA-8000D).

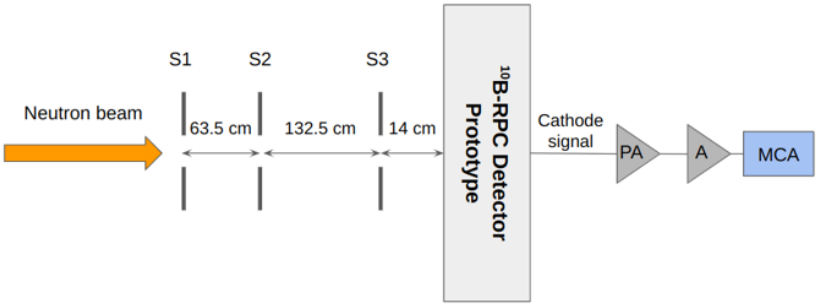

Figure 7.1: Schematic view of the first experimental setup in the beamline of the NARZISS reflectometer.

For the second experimental setup (Figure 7.2), the neutron beam was collimated only by slit S1 with an aperture of 1 mm x 50 mm and slit S2 with an aperture of 1 mm x 25 mm. The distance of both slits from the detector remained the same as for the previous setup. The detector was mounted on a mechanised table, enabling horizontal movement across the beam in regular steps. This allowed us to check the uniformity of the detector spatial response using the same irradiation conditions. In this experimental setup, the detector was connected to the DAQ system to record the signals from the strips and cathode.

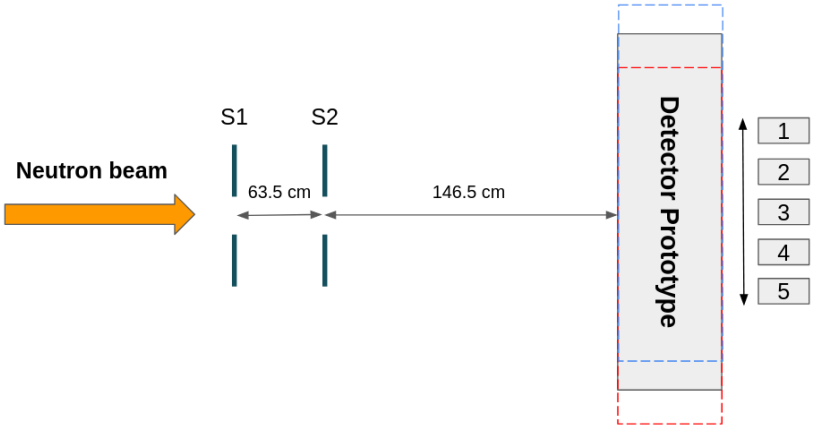

Figure 7.2: Schematic view of the second experimental setup in the beamline of the NARZISS reflectometer.

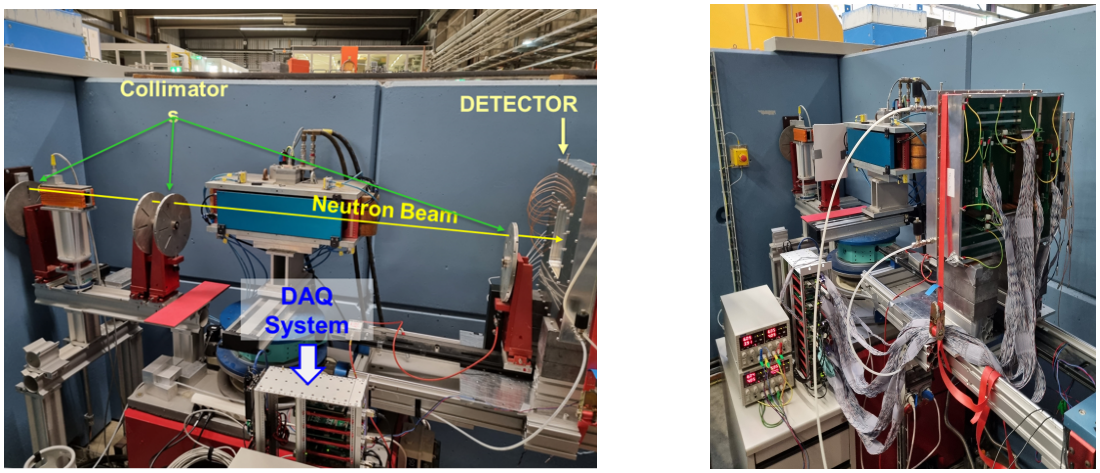

(a) (b)

Figure 7.3: (a) Assembly of the experimental setup, detector mounted on the mechanised table. (b) Back view of the detector (back lid is not yet installed), showing the connections between the front end electronic boards and the DAQ.

7.2 Test Results at NARZISS

7.2.1 Plateau Measurement Results

The results presented in this sub-section are from the measurements realised with the first experimental setup (Figure 7.1).

The thermal neutron plateau (counting rate vs. applied voltage on the cathode of the ^{10}B-RPC) was measured using the multichannel analyser by recording the number of events in an interval of 100 s for each ^{10}B-RPC module as a function of the HV applied to their cathodes. While taking measurements, it was observed that the ^{10}B-RPC modules 1, 4, and 7 were not operational. As a result, the three non-functional RPCs were unable to be operated and tested. Upon further investigation after the detector was disassembled at LIP, it was found that the soldering between the cathode and the SHV connector had become disconnected, most likely during the detector transportation. Figure 7.4 shows the plateau measured for the seven operational ^{10}B-RPC. It can be seen that for most ^{10}B-RPC modules, the plateau extends over a range of 200V, and the knee appears at around 1800V. The only exception is for the ^{10}B-RPC 8, where the plateau extends over a range of about 100V, and the knee appears at around 1900V. The relative neutron detection efficiency of the ^{10}B-RPC modules was calculated by considering the count rates measured with an applied voltage on the ^{10}B-RPCs cathodes of 1900 V.

These counting rates were then compared with the contribution of each ^{10}B-RPCs to the detection efficiency obtained from a Monte Carlo simulation of the detector (see Chapter 5.3), using a neutron wavelength of 4.94 Å(Narzis beamline). Comparing the simulated contributions

to detection efficiency with the scaled relative counting rates revealed a good match between the two results (see Figure 7.5).

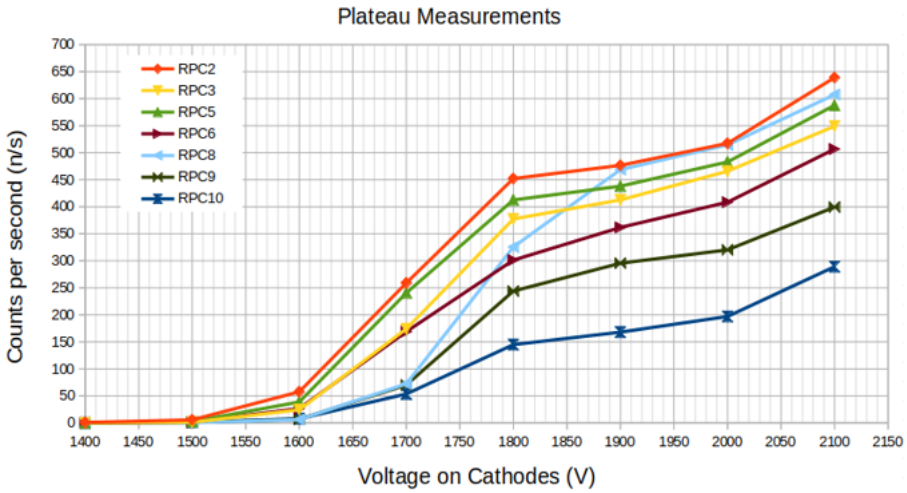

Figure 7.4: Counts per second as a function of the voltage applied to the cathodes for each ^{10}B-RPC module.

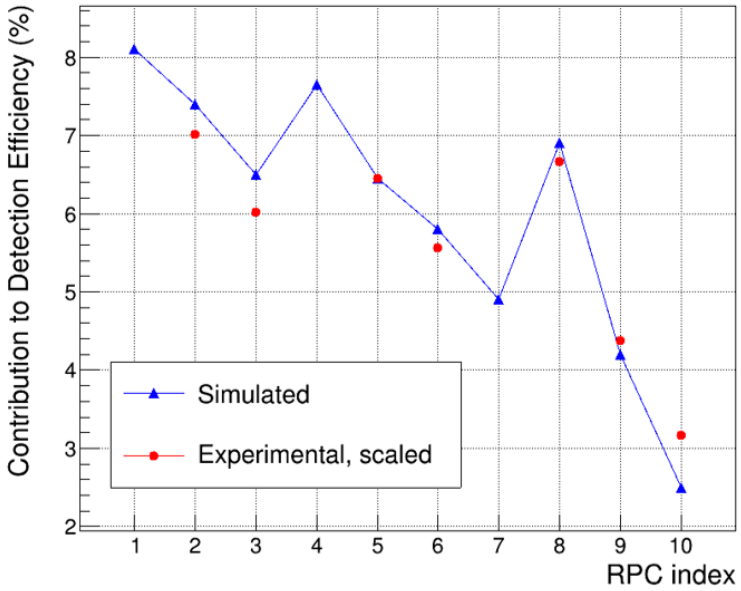

Figure 7.5: Simulated contributions to the detection efficiency of each ^{10}B-RPC (blue) and the respective measured counting rates, scaled (red). The scaling of the experimental data was performed by multiplying the count rate values with a factor such that both curves have the same value for RPC index 5.

Figure 7.6 shows the charge spectra measured in three different conditions: The blue curve was measured when the beam shutter was open, allowing the passage of neutrons; the green curve was measured by placing an absorber composed of Boron Carbide in front of the detector window, so that the neutrons would be absorbed before reaching the detector, and only the gamma-rays, originated from neutron-induced processes in the surrounding materials, hit the

detector. The red curve is the environment background, and to record it, the beam shutter was closed, and the detector was counting only the environmental radiation and its own dark-count background. As the response for all operational ^{10}B-RPC modules was similar, only the results for module number 2 are shown in Figure 7.6.

As expected from previous results [73], the charge spectrum for the neutron events (blue curve in Figure 7.6) exhibits two distinct regions: a narrow peak in the smaller induced charge region and a broader one at larger charges. Based on the experimental results, the shape of the distribution also indicates that the detector is correctly operating in avalanche mode, without the presence of streamers.

The part of the charge spectrum originating from the detection of gamma rays and background exhibits only a narrow peak within the small induced charge region, similar to the one seen in the spectrum registered with the beam shutter open. This suggests that the events in this region can be attributed to mostly gamma rays and background radiation. As a result, the suppression threshold can be established in the middle of the valley of the blue curve (neutron events), near channel 12. This threshold can be considered an effective criteria for the discrimination of the gamma rays and background events, with a small fraction of neutron events rejected.

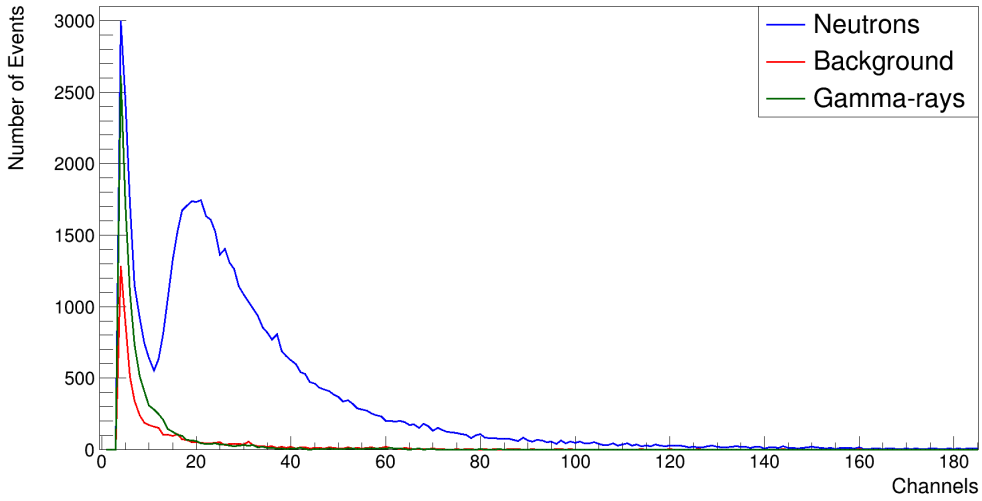

Figure 7.6: Measured charge spectra for: (blue) beam shutter open; (green) beam shutter open but with a $^{10}B_4C$ neutron absorber in front of the detector window; (red) beam shutter closed (detector's dark counts and environmental background).

7.2.2 Charge Spectrum Uniformity Over The Active Area

The results presented in this sub-section are from the measurements taken in the second experimental setup (Figure 7.2).

During attempts to operate all ^{10}B-RPC modules simultaneously (except modules 1, 4 and 7), it was noticed a significant electromagnetic noise in the triggering system originating from the machinery of the experimental hall. This noise caused a high triggering rate that exceeded the capacity of the DAQ system and resulted in it becoming overloaded. Due to the time constraints already mentioned before and the fact that the DAQ was not prepared to operate in such a high-noise environment, it was decided to proceed with the planned tests using only one ^{10}B-RPC, specifically module 2.

Figure 7.7 shows five charge spectra of the cathode signals recorded by the DAQ with the detector area irradiated in five different positions. All spectra are normalised to the highest event count. The events below the suppression threshold are not shown. The measured charge spectrum for all positions displays a similar profile except for position 5. The peak for position 5 (magenta curve in Figure 7.7) is observed at around ADC channel 850, while for the remaining positions, the peak appears at around ADC channel 1000. After conducting a thorough inspection, I observed that the time interval between the position 4 and position 5 acquisitions was significantly longer compared to the time interval between the first four acquisitions. This difference in time, combined with the movement of the detector, may have led to a change in the gas conditions inside the gas-tight chamber, affecting the gas amplification and resulting in a different charge spectrum for the fifth position. Although the conditions in position 5 were different from the conditions in the other four, the difference observed in the charge spectrum is minor, suggesting a uniform response of the detector across the active area. This behaviour indicates the absence of major variations in the gas gap width and no fluctuations of the electric field throughout the active area.

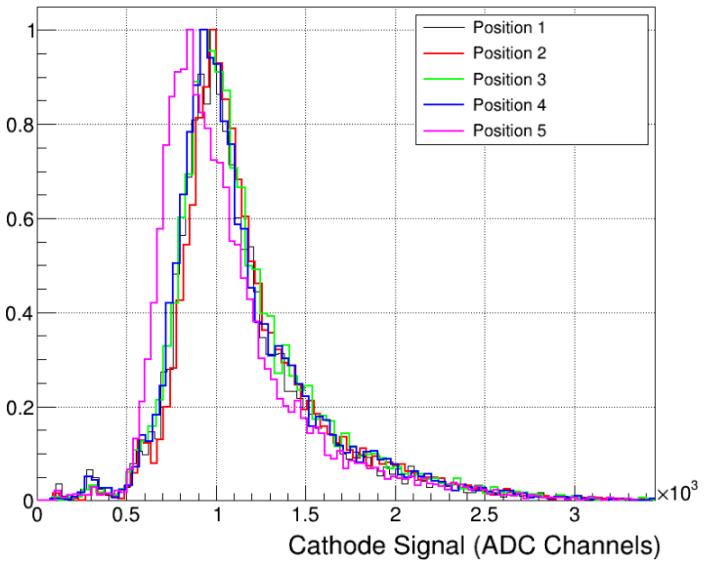

Figure 7.7: The distribution of the cathode signals for each irradiated position.

While the data sets for the acquisitions were very small (limited to approximately 8000 events each), I decided it was still useful to reconstruct the images of the 2D position for the neutron events. This would not just provide information about the capabilities of the detector to resolve the XY position but also to analyse if there was any problem with the connection of the pickup strips to the ZIF connectors or any dead channels in the front end electronic boards.

Since the front end electronic cards were moved to cover different areas of the detector sensitive area (as mentioned in Chapter 6.3), I needed to establish the correspondence between the position of the front end electronics boards with their corresponding x- and y-pickup strips by using my mapping algorithm (see Appendix A). Next, I utilised the neutron event selection algorithm (see Appendix B) to separate the good neutron events from the background ones. The minimum threshold for the cathode value was set to ADC channel 400, which is a value in the valley region of the charge spectra shown in Figure 7.7, that had the best trade-off between the number of rejected background events and the number of neutron events. To determine the XY coordinates of an event, I applied the centre of gravity algorithm [74]. The reconstructed positions are presented in Figure 7.8. It is observed a similar profile of the reconstructed images throughout all irradiated areas, with an image on the detector of about 5 mm width and 70 mm height. Since the position reconstructions have a similar profile and the charge spectra had minor observed differences, this fact suggests a uniform response of the detector over the active area.

Another important remark is that both algorithms (see Appendix A and B) worked successfully in the mapping of the electronic channels with the correspondent x- and y-pickup strips and by separating background events from neutron events.

In the images of the reconstructed events position, several gaps appear in the same region for the different detector positions. After analysing other reconstruction images which were made for the different readout areas of the detector, it was possible to verify that the gaps located at Y positions of 3mm and -24 mm remained, indicating that they are caused by malfunctioning channels in the front-end electronics cards. After the disassembly of the detector at our laboratory, it was concluded that the gap at the Y position -5 mm is due to a non-functional pickup strip. The gap at the Y position of -55 mm only appears when the detector is irradiated in position 3, suggesting a malfunction of the front-end electronics or the DAQ only during this acquisition.

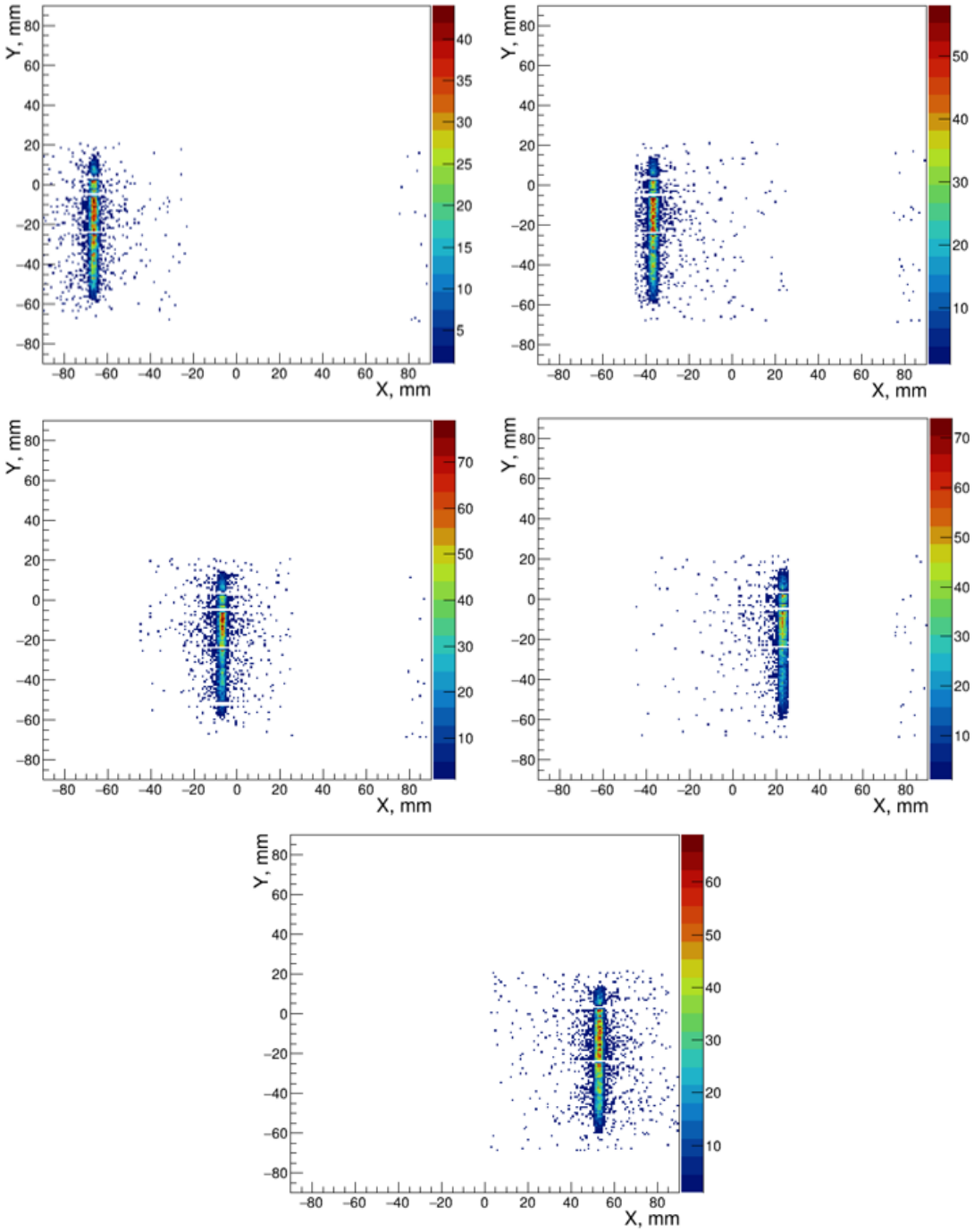

Figure 7.8: Images of the reconstructed neutron events positions from region 1 to 5.

7.3 Experimental Setup at BOA Beamline

The measurements on the BOA beamline were conducted only with the ^{10}B-RPC module 2 due to the same electromagnetic noise issues faced at the NARZISS beamline. At the BOA neutron beamline, a high-intensity quasi-continuous white beam is available, which covers a wide range of neutron wavelengths.

An experimental setup to measure the neutron time-of-flight was assembled, as illustrated in Figure 7.9. The neutron beam is collimated by a cadmium slit with a 10 mm x 10 mm aperture.

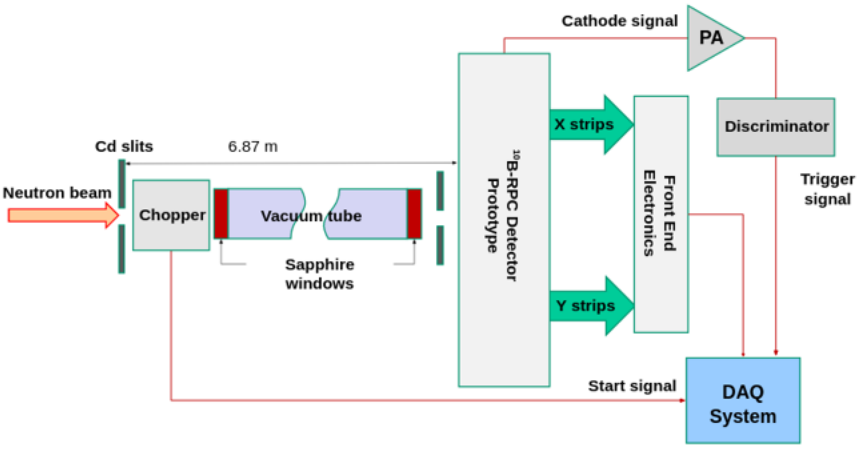

Figure 7.9: Schematics of the experimental setup at the BOA beamline.

A chopper is installed after the slit. It is a device that consists of $^{10}B_4C$ blades that rotate at a frequency of 9.5 Hz and block the beam during part of its motion, allowing the neutrons to pass when the blades are in a narrow acceptance angle with the beam direction. The chopper transforms the quasi-continuous neutron beam into a pulsed beam. It also provides a timestamp (T_0) corresponding to the time instant when a bunch of neutrons exit the chopper (Figure 7.10). The neutrons travel 6.87 m before reaching the detector, and the fast ones arrive at the detector earlier than the slow ones, allowing to differentiate them by measuring the time of flight. In order to minimise the neutron scattering in air, a vacuum tube with sapphire windows on both sides is placed between the chopper and the detector. When a neutron reaches the detector, if the detection happens, the induced signals from the strips and cathode are recorded by the DAQ. The fast component of the cathode signal is used to define a timestamp (T_f) for the end of the neutron flight.

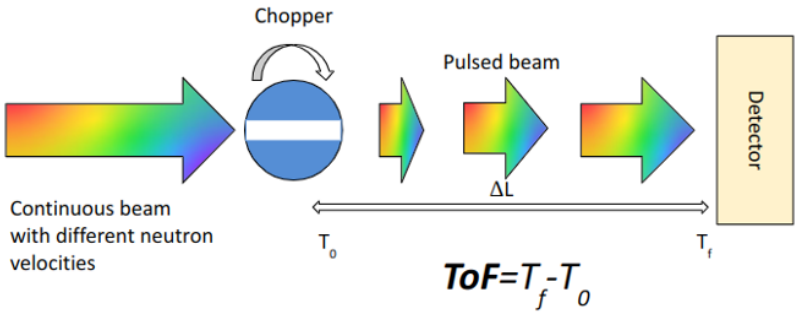

Figure 7.10: Diagram of the chopper working principle. The chopper transforms the quasi-continuous neutron beam into a pulsed beam. It also provides a timestamp (T_0) corresponding to the start moment of the neutron flight.

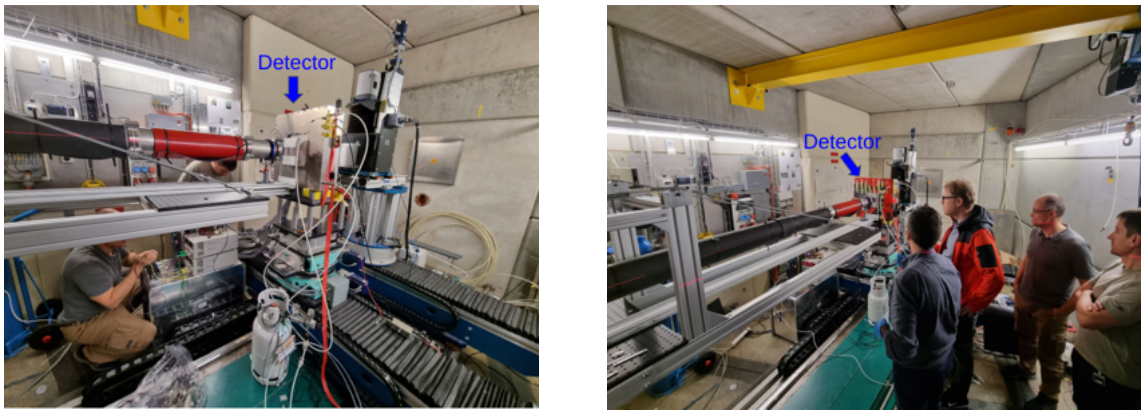

(a) (b)

Figure 7.11: (a) Experimental setup at the BOA beamline. Left: Assembly of the experimental setup. (b) Setup already assembled, detector protected with sheets of $^{10}B_4C$ to absorb scattered and divergent neutrons.

7.4 Results from BOA

7.4.1 Measurement of the Neutron TOF

As a first step, it is mandatory to verify if the time difference from neighbouring chopper timestamps corresponds to the configured frequency for the chopper rotation, which was 9.5 Hz ($T \approx 52$ ms). The distributions of the time between the neighbouring chopper timestamps (see Figure 7.12) show that the frequency recorded by the DAQ was not stable, presenting false triggers before the chopper configured frequency. The further analysis was performed ignoring those trigger pulses which had < 51 ms from the previous one.

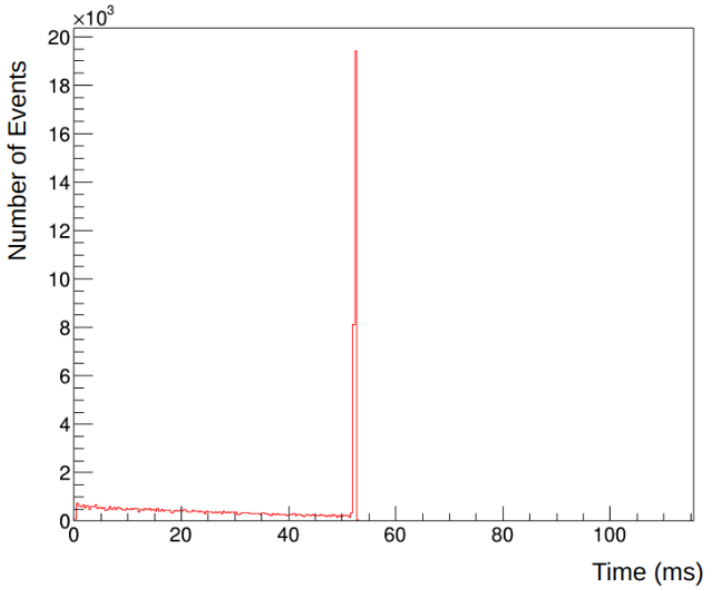

Figure 7.12: Histogram of the chopper trigger pulses.

For each detected neutron, the neutron TOF is determined by calculating the time difference between the timestamp provided by the cathode and the chopper. Figure 7.13 shows the measured number of neutron events as a function of the neutron TOF.

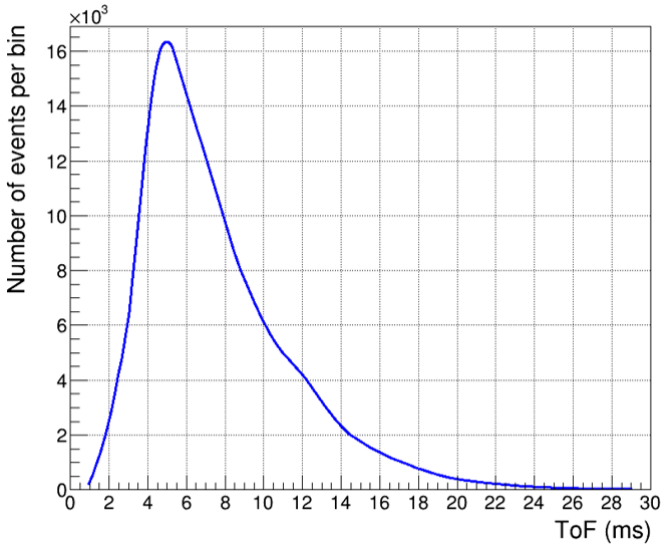

Figure 7.13: Measured number of neutron events as a function of the time of flight.

In order to compare the obtained result with the actual data from the BOA beamline [75], It was needed to compute the neutron wavelength spectrum, which is the number of neutrons impacting on the detector as a function of the neutron wavelength. By calculating the neutron velocity from the neutron TOF and using de Broglie's momentum wavelength equation (Equation 2.11), it is possible to calculate the neutron wavelength. The number of detected neutrons is not equal to the number of neutrons impacting on the detector. This is due to the neutron capture cross section dependence on the wavelength of the neutron, which results in a different number of detected neutrons for each wavelength. So, to obtain the number of neutrons impacting on the detector, we need to divide the number of the detected neutrons for a certain wavelength by its corresponding detection efficiency. These values are obtained first by performing 20 Monte Carlo simulations of the detector (see Chapter 5.3), each using different neutron wavelengths across a range of 0.1 to 20 Å. The simulated detection efficiency as a function of the neutron wavelength is presented in Figure 7.14. The detection efficiency in between the simulated points is estimated by performing linear interpolation. The neutron wavelength spectrum is shown in Figure 7.15a.

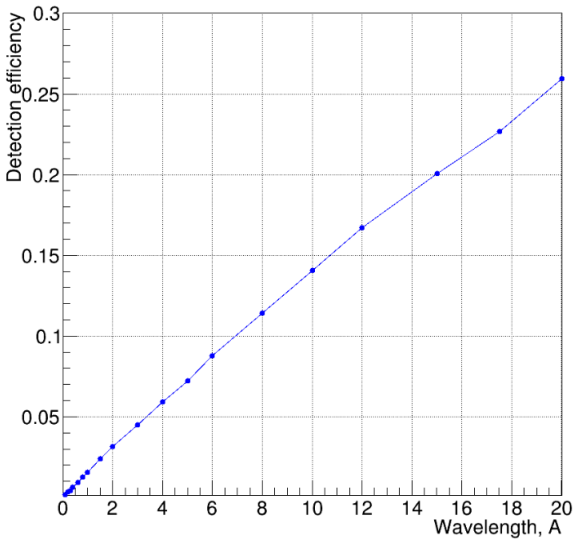

Figure 7.14: Simulated detector's detection efficiency as a function of the neutron wavelength.

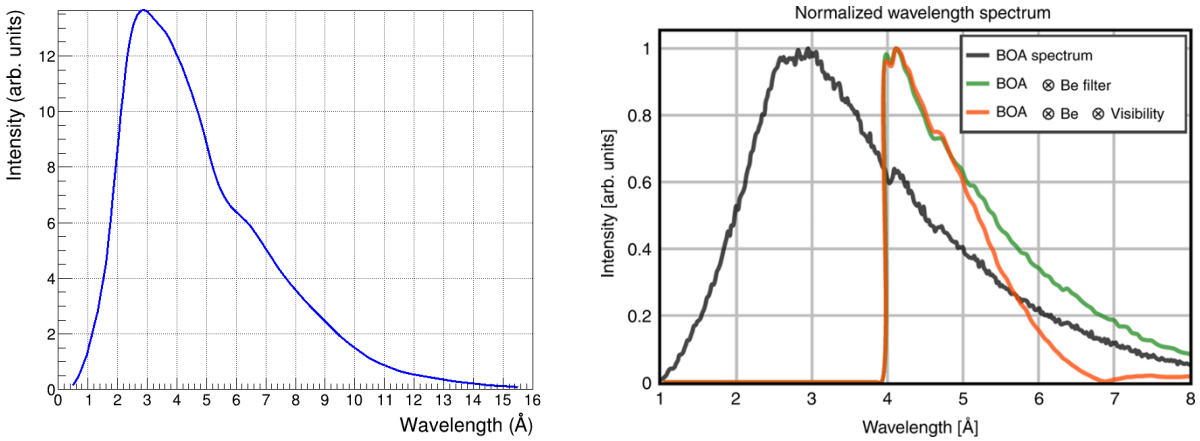

(a) (b)

Figure 7.15: (a) Measured neutron wavelength spectrum for the BOA beamline. (b) Neutron wavelength spectrum for BOA beamline (black curve). The second graph is taken from [75]

There is a good agreement between the measured neutron spectrum and the one for the BOA beamline presented in Figure 7.15b, with the peak for the measured spectrum and the one in literature both being around 3 Å.

7.4.2 Identification of the $^{10}B_4C$ Layer Where Neutron is Captured

Benefiting from the strong intensity of the neutron beam at the BOA beamline that allowed us to quickly acquire large datasets, we can verify that the sum of the induced signals for the x- and y- pickup strips follow the predictions made in Chapter 5 for the events that happen in the upper or lower gap of a ^{10}B-RPC.

The distributions for the sum of the amplitudes of the x- and y-strip signals are shown

in Figure 7.16. Both distributions exhibit two distinguishable peaks, the first being higher and somewhat narrower than the second one. As discussed in Chapter 5, these peaks can be explained by the presence of two types of events corresponding to the neutron captures in the upper or lower $^{10}B_4C$ layer of the cathode. As the upper gas gap is faced by the x-strips, the y-strips are partially screened by the x-ones, and therefore, the sum of the x-signals is larger. On the contrary, the lower gas gap is faced by the y-strips, so the sum signal of y-strips is larger than that for x-strips.

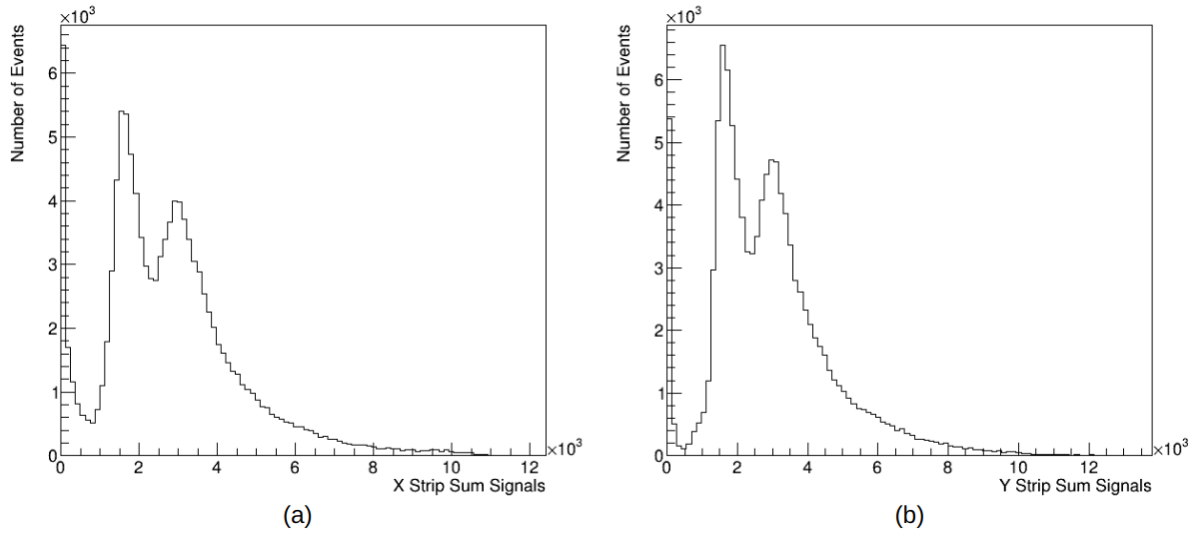

Figure 7.16: Histograms of the sum of the amplitudes of the x- and y-strip signals, (a) and (b), respectively.

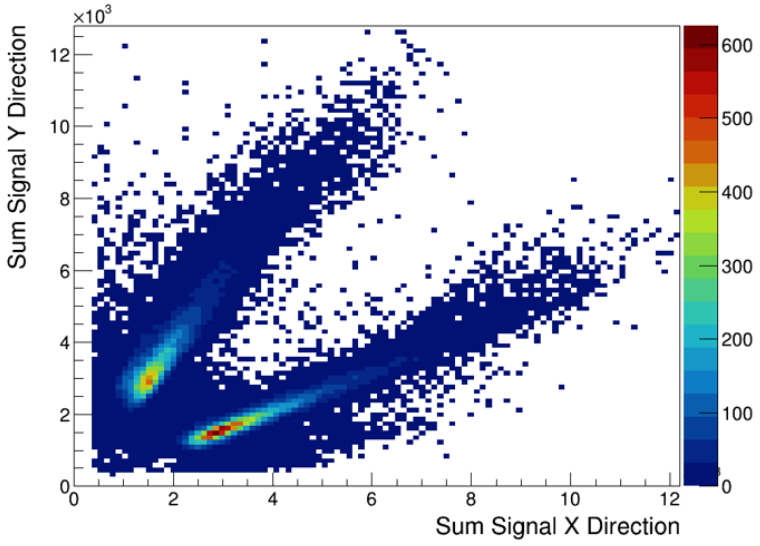

Figure 7.17: Density plot of the sum signal in the Y direction versus the sum signal in the X direction.

The presence of two types of events is more clear when making a density plot of the sum signal in the Y direction versus the sum signal in the X direction, where we can see two well-

separated regions (see Figure 7.17). Computing the ratio between the number of events that are attributed to the upper gap by the lower gap ones, we get a value of about 1.007, which is an expected difference due to the attenuation of the beam crossing the cathode with two layers of $^{10}B_4C$.

Taking into account the good separation of the two peaks shown in Figure 7.17 and the ratio of the number of events in the upper and the lower gaps being consistent with the neutron attenuation by crossing the cathode plate, we can conclude that the selected design of the pickup strips for the nRPC-4D detector is adequate for the identification of the $^{10}B_4C$ layer where the detected neutron was captured. This solves the ambiguity inherent in the use of the cathode signal for the determination of the Z coordinate and TOF measurements when the individual strips of each coordinate array with the same index are interconnected and readout using the same electronic channel.

Chapter 8

Conclusions and Outlook

The current state-of-the-art neutron detectors are still unable to meet the requirements set for modern instruments in neutron scattering science experiments planned for the European Spallation Source (ESS), the future spallation sources, the upgrade programs of the existing facilities and to replace 3He without a loss in performance and a significant increase in costs. Motivated by this, a novel concept of a thermal/cold neutron detector based on the ^{10}B-RPC technology has recently been introduced, called the nRPC-4D. The big goal of the project ongoing in LIP is to demonstrate that an nRPC-4D detector can provide a four-dimension readout capability (XYZ and time) of the neutron events with submillimetre positional and ns-scale timing resolution, making it a competitive alternative compared with the performance of the current state-of-the-art neutron detectors.

Aligned with this goal, the main objectives of the work on this thesis were to construct such a detector prototype and perform its characterisation with thermal neutrons. My main efforts during this work consisted in the assembly of a detector prototype implementing the nRPC-4D detector concept, the development of data processing tools, and the subsequent data analysis of the experimental results.

The prototype was assembled, tested in our lab and shipped to PSI for the characterisation at a neutron beamline. The measured continuing rates from the individual modules have shown a good match with the predictions of the Monte Carlo simulations, demonstrating good predictive power of the developed simulation model.

The capability of the prototype to precisely identify the XY as well as Z position of the neutron events was demonstrated. An improvement in comparison with the previous generation ^{10}B-RPC detector was achieved as the new prototype is capable of precisely identifying the converter layer of the triggered RPC unit where the neutron is captured.

Also, for the first time for this detection technology, the capabilities of a ^{10}B-RPC unit to

measure the neutron time of flight were shown. The detector was able to record the neutron wavelength spectrum of the BOA beamline, and the results show a close resemblance to the actual data known for this beamline.

The experimental results showcased the capabilities of the detector to simultaneously resolve the neutron event XYZ position and measure the neutron TOF. It can concluded that the proposed detector is indeed a promising technology for cold/thermal neutron detection, being a strong candidate for emerging neutron scattering science techniques such as TOF neutron diffraction, macromolecular neutron crystallography and energy-resolved neutron imaging.

Based on the demonstrated predictive power of the simulations, our group plans to continue the optimisation process of the detector design in terms of detection efficiency, the level of elastic scattering inside the detector and gamma background sensitivity. New low-resistivity glass will be used to construct the detector anode plates, allowing to significantly increase the detector counting rate.

The issues identified during this experimental campaign will also be addressed. The front-end electronics will be upgraded to be more robust and less sensitive to the environmental noise. The DAQ system will also be upgraded so as to be able to readout the entire sensitive area of the detector. A series of tests with the intent of further understanding the detector capabilities are currently being planned for different neutron facilities, beginning from a beamline at ILL, already in the early 2024.

Appendix A

DAQ Channels and Pick-up Strips Mapping Script

```
/*
// top-right
var boards_slots_x = [0, 0, 0, 0,    11, 12, 21, 22] //cathode index [7]
var boards_slots_y = [31, 32, 41, 42,   0,0, 0, 0] //cathode index [3]
// top-left
var boards_slots_x = [11, 12, 21, 0,    0, 0, 0, 22] //cathode index [7]
var boards_slots_y = [31, 32, 41, 42,   0,0, 0, 0] //cathode index [3]
// bottom-right
var boards_slots_x = [0, 0, 0, 0, 11, 12, 21, 22] //cathode index [7]
var boards_slots_y = [0, 0, 0, 42, 0, 31, 32, 41] //cathode index [3]
*/
// bottom-left
//var boards_slots_x = [11, 12, 21, 0, 0, 0, 0, 22] //cathode index [7]
//var boards_slots_y = [0, 0, 0, 42, 0, 31, 32, 41] //cathode index [3]

//middle
//var boards_slots_x = [0, 0, 11,12, 21, 0, 0, 22] //cathode index [7]
//var boards_slots_y = [0, 0, 31, 42, 32, 41, 0, 0] //cathode index [3]

//var boards_slots_y = [0, 0, 0 , 42, 31, 32, 41, 0]  // Y for uniform measure
//var boards_slots_x =  [ 0, 0, 0, 0,11,12, 21, 22] //right
//var boards_slots_x =  [11,12, 21, 0, 0, 0, 0, 22] //left
//var boards_slots_x = [0, 0, 11,12, 21, 0, 0, 22] //Xmid  ///////////////

//var boards_slots_y = [31, 32, 41, 42,   0,0, 0, 0] // top

/*
```

```
28 // BOA - 2dec
29 var boards_slots_x = [0, 0, 0, 11,12, 21, 0, 22] //Xmid
30 var boards_slots_y = [0, 0, 0, 42, 31, 32, 41, 0] // top
31 */
32
33 //NARZIS_RUN7
34
35 //var boards_slots_x = [11, 12, 21,0, 0, 0, 0, 22]
36 //var boards_slots_y = [0, 0, 0, 42, 31, 32, 41, 0]
37 //NARZIS_RUN8_9
38 //var boards_slots_x = [0, 0, 0, 0, 11, 12, 21, 22]
39 //var boards_slots_y = [0, 0, 0, 42, 31, 32, 41, 0]
40 //NARZIS_RUN10
41 var boards_slots_x = [0, 0, 11, 12, 21, 0, 0, 22]
42 var boards_slots_y = [31, 32, 41, 42, 0, 0, 0, 0]
43 //NARZIS_RUN4_5_6
44 //var boards_slots_x = [0, 0, 11, 12, 21, 0, 0, 22]
45 //var boards_slots_y = [0, 0, 0, 42, 31, 32, 41, 0]
46
47
48 //Pins
49 var pins = []
50 for (var i = 0; i < 16; i++) pins.push([])
51
52 for (var i = 0; i < 187; i++){
53         //Xpins
54         if (i < 24){ pins[0].push(i)}
55         if (i>=24 && i<48) pins[1].push(i)
56         if (i>=48 && i<72) pins[2].push(i)
57         if (i>=72 &&i<96) pins[3].push(i)
58         if (i>= 96 && i<120){ pins[4].push(i)}
59         if (i>=120 && i<144) pins[5].push(i)
60         if (i>=144 && i<168) pins[6].push(i)
61         if (i>=168 && i<187) pins[7].push(i)
62         //Ypins
63         if (i < 24){ pins[8].push(i)}
64         if (i>=24 && i<48) pins[9].push(i)
65         if (i>=48 && i<72) pins[10].push(i)
66         if (i>=72 &&i<91) pins[11].push(i)
67         if (i>= 91 && i<115){ pins[12].push(i)}
68         if (i>=115 && i<139) pins[13].push(i)
69         if (i>=139 && i<163) pins[14].push(i)
```

```
70          if (i>=163 && i<187) pins[15].push(i)
71
72  }
73
74  //Boards
75  var board = [[], [], [], [], [], [], [], []]
76
77  for (var i = 0; i < 192; i++){
78
79          if (i < 24){ board[0].push(i)}
80          if (i>=24 && i<48) board[1].push(i)
81          if (i>=48 && i<72) board[2].push(i)
82          if (i>=72 &&i<96) board[3].push(i)
83          if (i>= 96 && i<120){ board[4].push(i)}
84          if (i>=120 && i<144) board[5].push(i)
85          if (i>=144 && i<168) board[6].push(i)
86          if (i>=168 &&i<192) board[7].push(i)
87
88  }
89
90
91
92  var boards = [11,12,21,22,31,32,41,42]
93
94  var dict = {11: 'n' , 12: 'n' , 21:  'n', 22: 'n' , 31: 'n' , 32:  'n', 41: 'n'
        , 42: 'n' }
95
96  var checkx = 0
97  var checky = 0
98
99
100
101 //check for duplicates
102 for (var i=0;i<8;i++){
103         number=boards[i]
104         var count = 0
105         for (var j = 0; j<8;j++){
106                 if (number==boards_slots_x[j] || number==boards_slots_y[j]) count
                        ++
107                 if (count>1) core.abort('Error: Duplicates in Boards slots')
108         }
109
```

```
110 }
111
112 if (boards_slots_x[7]!=22) core.print('Are you sure the x cathodes are connected
      in the right way? ')
113 if (boards_slots_y[3]!=42) core.print('Are you sure the y cathodes are connected
      in the right way? ')
114
115 for (var i = 0; i<boards_slots_x.length; i++)
116 {
117    if (boards_slots_x.length+boards_slots_y.length==16)
118    {
119       if (boards_slots_x[i]!=0)
120       {
121              if (checkx >= boards_slots_x[i]) core.print('Warning: Strange order
                    of connector in X')
122
123              if (boards.indexOf(boards_slots_x[i]) != -1)
124              {
125                     dict[boards_slots_x[i]]= i
126                     //position[0].push(i);
127                     checkx = boards_slots_x[i];
128              }
129              else core.abort('Error: not valid board in boards_slots_x')
130       }
131
132       if (boards_slots_y[i]!=0){
133
134             if (checky >= boards_slots_y[i] ) { if (boards_slots_y[3]!=42) core.
                  print('Warning: Strange order of connector in Y')}
135
136             // if (i==3) last=i
137              if (boards.indexOf(boards_slots_y[i]) != -1)
138              {
139                     dict[boards_slots_y[i]]= i + boards_slots_x.length
140                     //position[1].push(i);
141                     checky = boards_slots_y[i];
142              }
143              else {core.abort('Error: not valid board in boards_slots_y')}
144       }
145    }
146    else
147    {
```

```
148             core.abort('ERROR: Wrong number os slots.')
149     }
150 }
151
152
153 //core.print(dict)
154 var xLUT = []
155 var yLUT = []
156
157 var c = 93
158 var offset = 0
159
160
161 for (var i = 0; i<boards.length;i++){
162         b = boards[i]
163         location = dict[b]
164         if (location<8 && location!='n' ){
165                 //core.print(location)
166                 boardxn = board[i]
167                 if (location==7){boardxn.splice(0,5)}
168                 offset = pins[location][0]-c-boardxn[0]
169                 for (var l=0;l<boardxn.length;l++){
170                         var xi = offset + boardxn[l]
171                         xLUT.push(xi)
172                 }
173
174         }
175         else if (location == 'n')continue
176         else{
177                 boardyn = board[i]
178                 if (location==3+8){boardyn.splice(boardyn.length-5,5)}
179                 offset = pins[location][0]-c-boardyn[0]
180                 for (var l=0;l<boardyn.length;l++){
181                         var yi = offset + boardyn[l]
182                         yi = -yi
183                         yLUT.push(yi)
184                 }
185
186
187
188         }
189 }
```

```
190
191 core.print(xLUT)
192 core.print(xLUT.length)
193 core.print(yLUT)
194 core.print(yLUT.length)
```

Appendix B

Neutron Event Selection Script

```
1  //Using logical channels (cathodes are in the end!)
2  var logicalXs = [0, 1, 2, 3, 4, 5, 6, 7, 8, 9, 10, 11, 12, 13, 14, 15, 16, 17,
       18, 19, 20, 21, 22, 23, 24, 25, 26, 27, 28, 29, 30, 31, 32, 33, 34, 35, 36,
       37, 38, 39, 40, 41, 42, 43, 44, 45, 46, 47, 48, 49, 50, 51, 52, 53, 54, 55,
       56, 57, 58, 59, 60, 61, 62, 63, 64, 65, 66, 67, 68, 69, 70, 71, 72, 73, 74,
       75, 76, 77, 78, 79, 80, 81, 82, 83, 84, 85, 86, 87, 88, 89, 90]
3  var logicalYs = [91, 92, 93, 94, 95, 96, 97, 98, 99, 100, 101, 102, 103, 104,
       105, 106, 107, 108, 109, 110, 111, 112, 113, 114, 115, 116, 117, 118, 119,
       120, 121, 122, 123, 124, 125, 126, 127, 128, 129, 130, 131, 132, 133, 134,
       135, 136, 137, 138, 139, 140, 141, 142, 143, 144, 145, 146, 147, 148, 149,
       150, 151, 152, 153, 154, 155, 156, 157, 158, 159, 160, 161, 162, 163, 164,
       165, 166, 167, 168, 169, 170, 171, 172, 173, 174, 175, 176, 177, 178, 179,
       180, 181]
4  var cathodeLUT = [182, 183, 184, 185, 186, 187, 188, 189, 190, 191]
5
6  var Xpos =[-45, -44, -43, -42, -41, -40, -39, -38, -37, -36, -35, -34, -33, -32,
        -31, -30, -29, -28, -27, -26, -25, -24, -23, -22, -21, -20, -19, -18, -17,
       -16, -15, -14, -13, -12, -11, -10, -9, -8, -7, -6, -5, -4, -3, -2, -1, 0, 1,
        2, 3, 4, 5, 6, 7, 8, 9, 10, 11, 12, 13, 14, 15, 16, 17, 18, 19, 20, 21, 22,
        23, 24, 25, 26, 75, 76, 77, 78, 79, 80, 81, 82, 83, 84, 85, 86, 87, 88, 89,
        90, 91, 92, 93]
7  var Ypos =[93, 92, 91, 90, 89, 88, 87, 86, 85, 84, 83, 82, 81, 80, 79, 78, 77,
       76, 75, 74, 73, 72, 71, 70, 69, 68, 67, 66, 65, 64, 63, 62, 61, 60, 59, 58,
       57, 56, 55, 54, 53, 52, 51, 50, 49, 48, 47, 46, 45, 44, 43, 42, 41, 40, 39,
       38, 37, 36, 35, 34, 33, 32, 31, 30, 29, 28, 27, 26, 25, 24, 23, 22, 21, 20,
       19, 18, 17, 16, 15, 14, 13, 12, 11, 10, 9, 8, 7, 6, 5, 4, 3]
8
9
10
11
```

```
12
13 var numEvents = events.countEvents()
14 var sigAr = events.GetPMsignals()
15 events.SetReconstructedAllEventsGood(true)
16 var eventcount = 0
17 var minsig = 50 //minimum th for the strip
18 var catmin = 400 //minimum th for the strip
19 var pickmin = 200 //minimum th for the cluster peak
20
21
22 //diagnotics
23 var cathevent = 0 //no signal on the cathode
24 var xmultievent = 0 //no signal on the xstrips
25 var ymultievent = 0 //no signal on the ystrips
26 var blwthevent = 0 //peak below th
27 var xnoevent = 0 //no clusters in x
28 var ynoevent = 0 //no clusters in x
29 var doublepick = 0 //multiple peak in cluster
30 var thsumsig = catmin //th to check how many sum signals in the strips are above
       the catmin
31
32
33 var gap1 = 0
34 var gap2 = 0
35
36
37
38 hist.NewHist("Mx",100,0,20)
39 hist.NewHist("My",100,0,20)
40 hist.SetTitles("Mx", "Multiplicity X Direction","")
41 hist.SetTitles("My", "Multiplicity Y Direction","")
42
43
44
45 hist.NewHist("time",16,0,0)
46 hist.SetTitles("time", "Time (ms)","")
47
48 hist.NewHist("lambda",16,0,0)
49 hist.SetTitles("lambda", "Wavelength (#AA)","Number of events per bin")
50 hist.NewHist("SumX",100,0,0)
51 hist.SetTitles("SumX", "Sum Signal X Direction","Number of events per bin")
52 hist.NewHist("SumY",100,0,0)
```

```
53 hist.SetTitles("SumY","Sum SignalY Direction","Number of events per bin")
54
55 hist.NewHist2D( "2DSumsignal",  100,  0,  0,  100,  0,  0 )
56 hist.SetTitles("2DSumsignal","Sum Signal X Direction","Sum Signal Y Direction")
57
58 for(iEv = 0; iEv<numEvents; iEv++){
59
60    var findx = 0
61    var findy = 0
62    var sig = sigAr[iEv]
63    var catcount = 0
64    if(sigAr[iEv][202]>tchopper){tchopper = sigAr[iEv][202]}
65    if(sigAr[iEv][202]<tchopper && sigAr[iEv][202]!=0){tchopper = sigAr[iEv
          ][202]}
66
67    for(icat=0; icat<cathodeLUT.length;icat++){
68
69   var cathlogical = cathodeLUT[icat]
70   var sigcat = sig[cathlogical]
71   if(sigcat>catmin){
72   catcount++
73   var catodo = cathlogical -181
74
75   }
76  }
77    if(catcount==0){
78   cathevent++ //diagnostics
79   var xevent = []
80   var Xallevents = [] //list in this way [[[list of strips in event], center]]
81   var yevent = []
82   var Yallevents = []
83   var xcenter = 0
84   var ycenter = 0
85   var maxsig = 0
86   var countmax = 0
87
88   //vou processar os clusters a seguir, considerando sempre o de maior amplitude
         e com um th de 400. verificar tamb m os duplos picos
89   //analize x signals
90   for(ixsig = 0; ixsig<logicalXs.length; ixsig++){
91  var xlogical = logicalXs[ixsig]
92  //if (xlogical==8 || xlogical==9 || xlogical==10 || xlogical==11)continue
```

```
93
94  var xsig = sig[xlogical]
95  if(xsig > minsig){
96 xevent.push(ixsig)
97 if(maxsig<xsig){
98    maxsig = xsig
99    xcenter = xevent.length-1
100 }
101   }
102
103  else if(xsig<minsig && xevent.length<2){
104 //no event
105  xevent = []
106  xcenter = 0
107  maxsig = 0
108   }
109
110  else if(xsig<minsig && xevent.length>=2){
111 //possible event
112 if(sig[logicalXs[xevent[xcenter]]]>pickmin){
113    //event in x!
114    Xallevents.push([xevent, xcenter])
115    xevent = []
116    xcenter = 0
117    maxsig = 0
118
119
120 }
121 else{
122    xevent = []
123    xcenter = 0
124    maxsig = 0
125
126
127 }
128  }
129
130  else if(ixsig==(logicalXs.length -1)){ //last strip
131 if(sig[logicalXs[xevent[xcenter]]]>pickmin){
132    //event in x!
133    Xallevents.push([xevent, xcenter])
134    xevent = []
```

```
135     xcenter = 0
136     maxsig = 0
137 }
138 else{
139     xevent = []
140     xcenter = 0
141     maxsig = 0
142 }
143 
144  }
145 } //end of x for
146 
147 if(Xallevents.length==0){
148 xnoevent++
149 events.SetReconstructionOK(iEv, false)
150 continue
151 //core.print("x")
152 //core.print(Xallevents)
153 }
154 
155 
156 if(Xallevents.length>0){
157  var passth = []
158  var eventsumsig = []
159  var sumsig = 0
160 
161  for(index=0;index<Xallevents.length;index++){
162 var sumsig = 0
163 var idsignal=Xallevents[index][0]
164 for(j=0; j<idsignal.length; j++){
165   xlogical = logicalXs[idsignal[j]]
166   sumsig += sig[xlogical]
167 
168 }
169 if(sumsig > thsumsig){
170    passth.push(index)
171 
172 
173 }
174  }
175  if(passth.length>1){//multievent
176 xmultievent++
```

```
177
178 events.SetReconstructionOK(iEv, false)
179 continue
180  }
181  if(passth.length<1){//belowth events
182 blwthevent++
183 events.SetReconstructionOK(iEv, false)
184 continue
185  }
186  if(passth.length==1){//Event
187  var Xrealevent = Xallevents[passth[0]][0]
188  //core.print(Xrealevent)
189 var versig = 0
190  var presentsig = 0
191  var picos = 0 //contagem do numero de picos
192  var pickreference = 0
193  for(i=0;i<Xrealevent.length;i++){ //encontrar duplos picos
194 xlogical = logicalXs[Xrealevent[i]]
195 presentsig = sig[xlogical]
196
197 if(versig>presentsig  ){
198    pickreference = 1
199    //firstpeak = Xpos[Xrealevent[i]]
200 }
201 if(pickreference>=1 && versig<presentsig && presentsig>100){
202 picos++
203    }
204 versig=presentsig
205   }
206
207  if(picos == 0) {findx = 1}
208
209  else{ // duplo picos
210 doublepick++
211 events.SetReconstructionOK(iEv, false)
212 continue
213  }
214  }
215 }
216
217
218
```

```
219
220
221 //analize y signals
222 maxsig = 0
223 for(iysig = 0; iysig<logicalYs.length; iysig++){
224  var ylogical = logicalYs[iysig]
225  var ysig = sig[ylogical]
226  if(ysig > minsig){
227 yevent.push(iysig)
228 if(maxsig<ysig){
229    maxsig = ysig
230    ycenter = yevent.length-1
231 }
232
233   }
234
235  else if(ysig<minsig && yevent.length<2){
236 //no event
237  yevent = []
238  ycenter = 0
239  maxsig = 0
240   }
241
242  else if(ysig<minsig && yevent.length>=2){
243 //possible event
244 if(sig[logicalYs[yevent[ycenter]]]>pickmin){
245    //event in y!
246    Yallevents.push([yevent, ycenter])
247    yevent = []
248    ycenter = 0
249    maxsig = 0
250 }
251 else{
252    yevent = []
253    ycenter = 0
254    maxsig = 0
255 }
256  }
257
258  else if(iysig==(logicalYs.length -1)){ //last strip
259 if(sig[logicalYs[yevent[ycenter]]]>pickmin){
260    //event in y!
```

```
261     Yallevents.push([yevent, ycenter])
262     yevent = []
263     ycenter = 0
264     maxsig = 0
265 
266 }
267 else{
268     yevent = []
269     ycenter = 0
270     maxsig = 0
271 }
272  }
273 }//end if y for
274 
275 if(Yallevents.length==0){
276     ynoevent++
277     events.SetReconstructionOK(iEv, false)
278     continue
279     //core.print("y")
280     //core.print(Yallevents)
281 }
282 
283 
284 if(Yallevents.length>0){
285  var passth = []
286  var eventsumsig = []
287  var sumsig = 0
288  for(index=0;index<Yallevents.length;index++){
289 var sumsig = 0
290 var idsignal=Yallevents[index][0]
291 for(j=0; j<idsignal.length; j++){
292   ylogical = logicalYs[idsignal[j]]
293   sumsig += sig[ylogical]
294 
295 }
296 if(sumsig > thsumsig){
297     passth.push(index)
298 }
299  }
300  if(passth.length>1){//multievent
301 ymultievent++
302 
```

```
events.SetReconstructionOK(iEv, false)
continue
 }
 if(passth.length<1){//belowth events
blwthevent++
events.SetReconstructionOK(iEv, false)
continue
 }
 if(passth.length==1){//Event
 var Yrealevent = Yallevents[passth[0]][0]
 var versig = 0
 var presentsig = 0
 var picos = 0 //contagem do numero de picos
 var pickreference = 0
 var fisrtpeak = 0
 var peakspacing = 0
 for(i=0;i<Yrealevent.length;i++){ //encontrar duplos picos
ylogical = logicalYs[Yrealevent[i]]
presentsig = sig[ylogical]

if(versig>presentsig){
   pickreference = 1
   //firstpeak = Ypos[Yrealevent[i]]
}
if(pickreference==1 && versig<presentsig){
picos++

  }
versig=presentsig
  }

 if(picos == 0) {findy =1}

 else{ // duplo picos
doublepick++

events.SetReconstructionOK(iEv, false)
continue
 }
 }


```

```
345 }
346
347
348
349 if(findx==1 && findy==1){
350
351   eventcount++
352
353   hist.Fill("Mx",Xrealevent.length,1)
354   hist.Fill("My",Yrealevent.length,1)
355   //reconstru  o
356
357   var Sx = 0
358   var Sy = 0
359   var X = 0
360   var Y = 0
361   var xi = 0
362   var yi = 0
363   var si = 0
364   var nx = 0
365   var ny = 0
366   for(i=0; i<Xrealevent.length;i++){
367  xi = Xpos[Xrealevent[i]]
368  xlogical = logicalXs[Xrealevent[i]]
369  si = sig[xlogical]
370  if(si>100){
371 X = X +xi*si
372 Sx = Sx + si
373 nx++
374   }
375   }
376   X = X/Sx
377   hist.Fill("SumX",Sx,1)
378   //hist.Fill("Mx",nx,1)
379   for(i=0; i<Yrealevent.length;i++){
380  yi = Ypos[Yrealevent[i]]
381  ylogical = logicalYs[Yrealevent[i]]
382  si = sig[ylogical]
383  if(si>100){
384 Y= Y + yi*si
385 Sy = Sy + si
386 ny++
```

```
 }
  }
  Y = Y/Sy
  hist.Fill("SumY",Sy,1)
  //hist.Fill("My",ny,1)
  events.SetReconstructed(iEv, X, Y, 0, 0)
  hist.Fill2D( "2DSumsignal",  Sx,  Sy,  1 )
  if(Sx>Sy)gap1++
  else gap2++

}

 }
  else{
 events.SetReconstructionOK(iEv, false)
  }
 }

//Diagn stico

core.print("cathode signals: "+cathevent)
core.print("total events: " + eventcount)
core.print("No xclusters: " + xnoevent/cathevent*100 + "%")
core.print("No yclusters: " + ynoevent/cathevent*100 + "%")
core.print("multievent in x: " + xmultievent/cathevent*100 + "%")
core.print("multievent in y: " + ymultievent/cathevent*100 + "%")
core.print("clusters below th: " + blwthevent/cathevent*100 + "%")
core.print("double picks: " + doublepick/cathevent*100 + "%")
core.print("false chopper triggers: " + falsechopper/cathevent*100 + "%")
core.print("gap1: " + gap1)
core.print("gap2: " + gap2)
var tudo = cathevent - eventcount-xnoevent-ynoevent-xmultievent-ymultievent-
    blwthevent-doublepick - falsechopper
core.print(tudo)


//Gr fico da reconstru  o

events.SetReconstructionReady()
grwin.PlotDensityXY(); grwin.AddToBasket("Dens")

//Other Utility tools
```

```
428
429
430 /*
431 hist.SetFillColor( "2DSumsignal",  1 )
432 hist.Draw("2DSumsignal","colz")
433 grwin.AddToBasket("2DSumsignal")
434 */
435 /*
436
437
438 hist.SetLineProperties("Mx", 4, 1, 1)
439 hist.Draw("Mx","")
440 grwin.AddToBasket("Mx Run 6")
441 hist.SetLineProperties("My", 6, 1, 1)
442 hist.Draw("My","")
443 grwin.AddToBasket("My Run 6")
444
445
446
447 hist.SetLineProperties("SumX", 4, 1, 1)
448 hist.Draw("SumX","")
449 grwin.AddToBasket("SumX Run 6")
450 hist.SetLineProperties("SumY", 4, 1, 1)
451 hist.Draw("SumY","")
452 grwin.AddToBasket("SumY Run 6")
453
454
455
456 */
```

References

[1] John M. Carpenter and Gerry H. Lander. 40 years of neutron scattering: A perspective. *Neutron News*, 21(1):10–12, 2010.

[2] Colin Carlile, Ryoichi Miyamoto, A. Pahlsson, M. Trojer, J.G. Weisend II, Marie-Louise Ainalem, Ken Andersen, K. Batkov, Patrik Carlsson, D. Ene, B. Heden, K. Hedin, Andrew Jackson, P. Jacobsson, Oliver Kirstein, Giobatta Lanfranco, Yongjoong Lee, Mats Lindroos, J. Rebec, and A. Zugazaga. *European Spallation Source Technical Design Report*. 04 2013.

[3] Johannes Baggemann, Sarah Böhm, Pau-Emmanuel Doege, J. Fenske, M. Feygenson, A. Glavic, O. Holderer, S. Jaksch, M. Jentschel, S. Kleefisch, Harald Kleines, Jingjing Li, K. Lieutnant, P. Mastinu, Eric Mauerhofer, O. Meusel, S. Pasini, H. Podlech, M. Rimmler, Ulrich Rücker, T. Schrader, W. Schweika, M. Strobl, E. Vezhlev, J. Voigt, Paul Zakalek, and O. Zimmer. *Conceptual Design Report Jülich High Brilliance Neutron Source (HBS)*, volume 8 of *Schriften des Forschungszentrums Jülich. Reihe Allgemeines / General*. Forschungszentrum Jülich GmbH Zentralbibliothek, Verlag, Jülich, 2020.

[4] Karl Zeitelhack. Search for alternative techniques to helium-3 based detectors for neutron scattering applications. *Neutron News*, 23(4):10–13, 2012.

[5] Dana Shea and D. Morgan. The helium-3 shortage: Supply, demand, and options for congress. *Congressional Research Service*, page R41419, 01 2011.

[6] Thomas Wilpert. Boron trifluoride detectors. *Neutron News*, 23(4):14–19, 2012.

[7] N. J. Rhodes. Scintillation detectors. *Neutron News*, 23(4):26–30, 2012.

[8] Carina Höglund, Jens Birch, Ken Andersen, Thierry Bigault, Jean-Claude Buffet, Jonathan Correa, Patrick van Esch, Bruno Guerard, Richard Hall-Wilton, Jens Jensen, Anton Khaplanov, Francesco Piscitelli, Christian Vettier, Wilhelmus Vollenberg, and Lars Hultman. B4C thin films for neutron detection. *Journal of Applied Physics*, 111(10):104908, 05 2012.

[9] D. Pfeiffer, F. Resnati, J. Birch, M. Etxegarai, R. Hall-Wilton, C. Höglund, L. Hultman, I. Llamas-Jansa, E. Oliveri, E. Oksanen, L. Robinson, L. Ropelewski, S. Schmidt, C. Streli, and P. Thuiner. First measurements with new high-resolution gadolinium-gem neutron detectors. *Journal of Instrumentation*, 11(05):P05011, may 2016.

[10] N.J. Rhodes. Scientific reviews: Status and future development of neutron scintillation detectors. *Neutron News*, 17(1):16–18, 2006.

[11] F. Piscitelli, F. Messi, M. Anastasopoulos, T. Bryś, F. Chicken, E. Dian, J. Fuzi, C. Höglund, G. Kiss, J. Orban, P. Pazmandi, L. Robinson, L. Rosta, S. Schmidt, D. Varga, T. Zsiros, and R. Hall-Wilton. The multi-blade boron-10-based neutron detector for high intensity neutron reflectometry at ess. *Journal of Instrumentation*, 12(03):P03013, mar 2017.

[12] K. Andersen, T. Bigault, J. Birch, J.C. Buffet, J. Correa, R. Hall-Wilton, L. Hultman, C. Höglund, B. Guérard, J. Jensen, A. Khaplanov, O. Kirstein, F. Piscitelli, P. Van Esch, and C. Vettier. 10b multi-grid proportional gas counters for large area thermal neutron detectors. *Nuclear Instruments and Methods in Physics Research Section A: Accelerators, Spectrometers, Detectors and Associated Equipment*, 720:116–121, 2013. Selected papers from the 2nd International Conference Frontiers in Diagnostic Technologies (ICFDT2).

[13] Christian J. Schmidt and Martin Klein. Scientific reviews: The cascade neutron detector: A system for 2d position sensitive neutron detection at highest intensities. *Neutron News*, 17(1):12–15, 2006.

[14] D. Pfeiffer, F. Resnati, J. Birch, M. Etxegarai, R. Hall-Wilton, C. Höglund, L. Hultman, I. Llamas-Jansa, E. Oliveri, E. Oksanen, L. Robinson, L. Ropelewski, S. Schmidt, C. Streli, and P. Thuiner. First measurements with new high-resolution gadolinium-gem neutron detectors. *Journal of Instrumentation*, 11(05):P05011, may 2016.

[15] L.M.S. Margato and A. Morozov. Boron-10 lined rpcs for sub-millimeter resolution thermal neutron detectors: conceptual design and performance considerations. *Journal of Instrumentation*, 13(08):P08007, aug 2018.

[16] L.M.S. Margato, A. Morozov, A. Blanco, P. Fonte, L. Lopes, K. Zeitelhack, R. Hall-Wilton, C. Höglund, L. Robinson, S. Schmidt, and P. Svensson. Multilayer 10b-rpc neutron imaging detector. *Journal of Instrumentation*, 15(06):P06007, jun 2020.

[17] Nikolay Kardjilov, Ingo Manke, Robin Woracek, André Hilger, and John Banhart. Advances in neutron imaging. *Materials Today*, 21(6):652–672, 2018.

[18] L.M.S. Margato, G. Canezin, A. Morozov, A. Blanco, J. Saraiva, L. Lopes, and P. Fonte. Timing resistive plate chambers for thermal neutron detection with 3d position sensitivity. *Nuclear Instruments and Methods in Physics Research Section A: Accelerators, Spectrometers, Detectors and Associated Equipment*, 1052:168267, 2023.

[19] H. Bethe. Zur Theorie des Durchgangs schneller Korpuskularstrahlen durch Materie. *Annalen der Physik*, 397(3):325–400, January 1930.

[20] F. Bloch. Bremsvermögen von Atomen mit mehreren Elektronen. *Zeitschrift fur Physik*, 81(5-6):363–376, May 1933.

[21] W.H. Bragg M.A. and R. Kleeman. Lxxiv. on the ionization curves of radium. *The London, Edinburgh, and Dublin Philosophical Magazine and Journal of Science*, 8(48):726–738, 1904.

[22] Robert R. Wilson. Radiological use of fast protons. *Radiology*, 47:487–491, 1946.

[23] Francesc Salvat. Bethe stopping-power formula and its corrections. *Phys. Rev. A*, 106:032809, Sep 2022.

[24] G.F. Knoll. *Radiation Detection and Measurement*. Number v. 415 in Radiation Detection and Measurement. Wiley, 1979.

[25] Albert Einstein. Concerning an heuristic point of view toward the emission and transformation of light. *Annalen Phys.*, 17:132–148, 1905.

[26] Auger, Pierre. Sur l'effet photoélectrique composé. *J. Phys. Radium*, 6(6):205–208, 1925.

[27] Ervin B. Podgoršak. *Interactions of Photons with Matter*, pages 277–375. Springer Berlin Heidelberg, Berlin, Heidelberg, 2010.

[28] Arthur H. Compton. A Quantum Theory of the Scattering of X-rays by Light Elements. *Phys. Rev.*, 21:483–502, 1923.

[29] Vinay Venugopal and Piyush Bhagdikar. de broglie wavelength and frequency of scattered electrons in the compton effect. *Physics Education*, 29:35, 03 2013.

[30] O. Klein and T. Nishina. Über die Streuung von Strahlung durch freie Elektronen nach der neuen relativistischen Quantendynamik von Dirac. *Zeitschrift fur Physik*, 52(11-12):853–868, November 1929.

[31] Wikimedia Commons. File:pair production.png — wikimedia commons, the free media repository, 2023. [Online; accessed 11-September-2023].

[32] Beer. Bestimmung der Absorption des rothen Lichts in farbigen Flüssigkeiten. *Annalen der Physik*, 162(5):78–88, January 1852.

[33] Francesco Piscitelli. *Boron-10 layers, Neutron Reflectometry and Thermal Neutron Gaseous Detectors*. PhD thesis, 01 2014.

[34] Alfred Klett. *Neutron Detection*. Springer Berlin Heidelberg, Berlin, Heidelberg, 2012.

[35] R. Santonico and R. Cardarelli. Development of resistive plate counters. *Nuclear Instruments and Methods in Physics Research*, 187(2):377–380, 1981.

[36] Yu.N. Pestov. Status and future developments of spark counters with a localized discharge. *Nuclear Instruments and Methods in Physics Research*, 196(1):45–47, 1982.

[37] R. Cardarelli, R. Santonico, A. Di Biagio, and A. Lucci. Progress in resistive plate counters. *Nuclear Instruments and Methods in Physics Research Section A: Accelerators, Spectrometers, Detectors and Associated Equipment*, 263(1):20–25, 1988.

[38] R. Cardarelli, A. Di Ciaccio, and R. Santonico. Performance of a resistive plate chamber operating with pure cf3br. *Nuclear Instruments and Methods in Physics Research Section A: Accelerators, Spectrometers, Detectors and Associated Equipment*, 333(2):399–403, 1993.

[39] M. Abbrescia, A. Colaleo, G. Iaselli, F. Loddo, M. Maggi, B. Marangelli, S. Natali, S. Nuzzo, G. Pugliese, A. Ranieri, F. Romano, S. Altieri, G. Belli, G. Bruno, R. Guida, S. P. Ratti, C. Riccardi, P. Torre, and P. Vitulo. The RPC system for the CMS experiment at the LHC. *Nuclear Instruments and Methods in Physics Research A*, 508(1-2):137–141, August 2003.

[40] S. Vernetto. Results from the argo-ybj experiment. *Nuclear Instruments and Methods in Physics Research Section A: Accelerators, Spectrometers, Detectors and Associated Equipment*, 630(1):22–27, 2011. Proceedings of the 2nd Roma International Conference on Astroparticle Physics (RICAP 2009).

[41] G Bari, A Candela, M De Deo, M D'Incecco, M Garbini, P Giusti, C Gustavino, M Lindozzi, H Menghetti, G Sartorelli, G Satta, and M Selvi. Analysis of the performance of the monolith prototype. *Nuclear Instruments and Methods in Physics Research Section A: Accelerators, Spectrometers, Detectors and Associated Equipment*, 508(1):170–174, 2003. Proceedings of the Sixth International Workshop on Resistive Plate Chambers and Related Detectors.

[42] Milind Datar, Satyajit Jena, Suresh Kalmani, Naba Mondal, P. Nagaraj, L. Reddy, M. Saraf, Satyanarayana Bheesette, R. Shinde, and Pankhuri Verma. Development of glass resistive plate chambers for ino experiment. *Nuclear Instruments and Methods in Physics Research Section A: Accelerators, Spectrometers, Detectors and Associated Equipment*, 602:744–748, 05 2009.

[43] João Saraiva, Carlos Alemparte, Daniel Belver, Alberto Blanco, Juan Callón, Jose Collazo, Alfredo Iglesias, and Luís Lopes. A large-area rpc detector for muography, 2022.

[44] Paulo Fonte, Luís Lopes, Rui Alves, Nuno Carolino, Paulo Crespo, Miguel Couceiro, Orlando Cunha, Nuno Dias, Nuno C. Ferreira, Susete Fetal, Ana L. Lopes, Jan Michel, Jorge Moreira, Américo Pereira, João Saraiva, Carlos Silva, Magda Silva, Michael Traxler, Antero Abrunhosa, Alberto Blanco, Miguel Castelo-Branco, and Mário Pimenta. An rpc-pet brain scanner demonstrator: First results. *Nuclear Instruments and Methods in Physics Research Section A: Accelerators, Spectrometers, Detectors and Associated Equipment*, 1051:168236, 2023.

[45] Christian Lippmann. *Detector Physics of Resistive Plate Chambers*. PhD thesis, Frankfurt U., 2003.

[46] F. Sauli. Principles of Operation of Multiwire Proportional and Drift Chambers. 5 1977.

[47] Sir Townsend, John. *The theory of ionization of gases by collision*. London, Constable, 1910. https://www.biodiversitylibrary.org/bibliography/22810.

[48] A. J. Davies and C. J. Evans. THE THEORY OF IONIZATION GROWTH IN GASES UNDER PULSED AND STATIC FIELDS. 9 1973.

[49] Christian Lippmann and Werner Riegler. Space charge effects in resistive plate chambers. *Nuclear Instruments and Methods in Physics Research Section A: Accelerators, Spectrometers, Detectors and Associated Equipment*, 517(1):54–76, 2004.

[50] Manuel Alejandro Del Rio Viera. Charge studies on multigap resistive plate chambers. Master's thesis, Benemerita Universidad Autonoma de Puebla, 2020.

[51] P. Fonte. Applications and new developments in resistive plate chambers. *IEEE Transactions on Nuclear Science*, 49(3):881–887, 2002.

[52] Vladimir Peskov, Marcello Abbrescia, and P. Fonte. *Resistive Gaseous Detectors: Designs, Performance, and Perspectives*. 04 2018.

[53] S. Ramo. Currents induced by electron motion. *Proceedings of the IRE*, 27(9):584–585, 1939.

[54] Werner Riegler. Induced signals in resistive plate chambers. *Nuclear Instruments and Methods in Physics Research Section A: Accelerators, Spectrometers, Detectors and Associated Equipment*, 491(1):258–271, 2002.

[55] W. Riegler. Extended theorems for signal induction in particle detectors vci 2004. *Nuclear Instruments and Methods in Physics Research Section A: Accelerators, Spectrometers, Detectors and Associated Equipment*, 535(1):287–293, 2004. Proceedings of the 10th International Vienna Conference on Instrumentation.

[56] H. Raether. *Electron Avalanches and Breakdown in Gases*. Butterworths advanced physics series. Butterworths, 1964.

[57] J.P. Saraiva, A. Blanco, J.A. Garzón, D. Garcìa-Castro, L. Lopes, and V. Villasante-Marcos. The tristan detector—2018–2019 latitude survey of cosmic rays. *Journal of Instrumentation*, 15(09):C09024, sep 2020.

[58] P. Baesso, D. Cussans, C. Thomay, and J. Velthuis. Toward a rpc-based muon tomography system for cargo containers. *Journal of Instrumentation*, 9(10):C10041, oct 2014.

[59] Sine2020-h2020 project. https://www.sine2020.eu/index.html.

[60] A. Muraro and G. Croci. Review of MPGD applications for neutron detection. *JINST*, 14(04):C04005, 2019.

[61] Oliver Kirstein, Richard Hall-Wilton, Irina Stefanescu, Maddi Etxegarai, Michail Anastasopoulos, Kevin Fissum, Anna Gulyachkina, Carina Hoglund, Mewlude Imam, Kalliopi Kanaki, Anton Khaplanov, Thomas Kittelmann, Scott Kolya, Björn Nilsson, Luis Ortega, Dorothea Pfeiffer, Francesco Piscitelli, Judith Ramos, Linda Robinson, and Julius Scherzinger. Neutron position sensitive detectors for the ess. *Proc. Sci.*, 11 2014.

[62] M. Anastasopoulos, R. Bebb, K. Berry, J. Birch, T. Bryś, J.-C. Buffet, J.-F. Clergeau, P.P. Deen, G. Ehlers, P. van Esch, S.M. Everett, B. Guerard, R. Hall-Wilton, K. Herwig, L. Hultman, C. Höglund, I. Iruretagoiena, F. Issa, J. Jensen, A. Khaplanov, O. Kirstein, I. Lopez Higuera, F. Piscitelli, L. Robinson, S. Schmidt, and I. Stefanescu. Multi-grid detector for neutron spectroscopy: results obtained on time-of-flight spectrometer cncs. *Journal of Instrumentation*, 12(04):P04030, apr 2017.

[63] M. Köhli, F. Allmendinger, W. Häußler, T. Schröder, M. Klein, M. Meven, and U. Schmidt. Efficiency and spatial resolution of the cascade thermal neutron detector. *Nuclear Instruments and Methods in Physics Research Section A: Accelerators, Spectrometers, Detectors and Associated Equipment*, 828:242–249, 2016.

[64] R. Nikolic, Chin Li Cheung, C. Reinhardt, and T. Wang. Roadmap for high efficiency solid-state neutron detectors. *Proc SPIE*, 6013, 10 2005.

[65] A Blanco, P Fonte, L Lopes, P Martins, J Michel, M Palka, M Kajetanowicz, G Korcyl, M Traxler, and R Marques. Toftracker: gaseous detector with bidimensional tracking and time-of-flight capabilities. *Journal of Instrumentation*, 7(11):P11012, nov 2012.

[66] S. Agostinelli, J. Allison, K. Amako, J. Apostolakis, H. Araujo, P. Arce, M. Asai, D. Axen, S. Banerjee, G. Barrand, F. Behner, L. Bellagamba, J. Boudreau, L. Broglia, A. Brunengo, H. Burkhardt, S. Chauvie, J. Chuma, R. Chytracek, G. Cooperman, G. Cosmo, P. Degtyarenko, A. Dell'Acqua, G. Depaola, D. Dietrich, R. Enami, A. Feliciello, C. Ferguson, H. Fesefeldt, G. Folger, F. Foppiano, A. Forti, S. Garelli, S. Giani, R. Giannitrapani, D. Gibin, J.J. Gómez Cadenas, I. González, G. Gracia Abril, G. Greeniaus, W. Greiner, V. Grichine, A. Grossheim, S. Guatelli, P. Gumplinger, R. Hamatsu, K. Hashimoto, H. Hasui, A. Heikkinen, A. Howard, V. Ivanchenko, A. Johnson, F.W. Jones, J. Kallenbach, N. Kanaya, M. Kawabata, Y. Kawabata, M. Kawaguti, S. Kelner, P. Kent, A. Kimura, T. Kodama, R. Kokoulin, M. Kossov, H. Kurashige, E. Lamanna, T. Lampén, V. Lara, V. Lefebure, F. Lei, M. Liendl, W. Lockman, F. Longo, S. Magni, M. Maire, E. Medernach, K. Minamimoto, P. Mora de Freitas, Y. Morita, K. Murakami, M. Nagamatu, R. Nartallo, P. Nieminen, T. Nishimura, K. Ohtsubo, M. Okamura, S. O'Neale, Y. Oohata, K. Paech, J. Perl, A. Pfeiffer, M.G. Pia, F. Ranjard, A. Rybin, S. Sadilov, E. Di Salvo, G. Santin, T. Sasaki, N. Savvas, Y. Sawada, S. Scherer, S. Sei, V. Sirotenko, D. Smith, N. Starkov, H. Stoecker, J. Sulkimo, M. Takahata, S. Tanaka, E. Tcherniaev, E. Safai Tehrani, M. Tropeano, P. Truscott, H. Uno, L. Urban, P. Urban, M. Verderi, A. Walkden, W. Wander, H. Weber, J.P. Wellisch, T. Wenaus, D.C. Williams, D. Wright, T. Yamada, H. Yoshida, and D. Zschiesche. Geant4—a simulation toolkit. *Nuclear Instruments and Methods in Physics Research Section A: Accelerators, Spectrometers, Detectors and Associated Equipment*, 506(3):250–303, 2003.

[67] A. Morozov, V. Solovov, R. Martins, F. Neves, V. Domingos, and V. Chepel. Ants2 package: simulation and experimental data processing for anger camera type detectors. *Journal of Instrumentation*, 11(04):P04022, apr 2016.

[68] A. Morozov, L.M.S. Margato, and I. Stefanescu. Simulation-based optimization of a multilayer 10b-rpc thermal neutron detector. *Journal of Instrumentation*, 15(03):P03019, mar 2020.

[69] Electrically conductive adhesive transfer tape type 9703 from 3m. https://www.digikey.com/en/product-highlight/3/3m/electrically-conductive-adhesive-transfer-tape-9703.

[70] Amphenol aorora 0.30mm pitch fpc right angle zif flex connectors. https://pt.mouser.com/new/amphenol/amphenol-030mm-fpc-zifflex-connectors/?_gl=1*m9n0nk*_ga*dW5kZWZpbmVk*_ga_15W4STQT4T*dW5kZWZpbmVk*_ga_1KQLCYKRX3*dW5kZWZpbmVk.

[71] Multi-cb. https://www.multi-circuit-boards.eu/en/index.html.

[72] Trb3 documents. http://trb.gsi.de/.

[73] L.M.S. Margato, A. Morozov, A. Blanco, P. Fonte, L. Lopes, J. Saraiva, K. Zeitelhack, R. Hall-Wilton, C. Höglund, L. Robinson, P. Svensson, L. Naumann, K. Roemer, D. Stach, and Th. Wilpert. Towards high-rate rpc-based thermal neutron detectors using low-resistivity electrodes. *Journal of Instrumentation*, 16(07):P07009, jul 2021.

[74] A. Morozov, L.M.S. Margato, V. Solovov, A. Blanco, J. Saraiva, T. Wilpert, K. Zeitelhack, K. Roemer, C. Höglund, L. Robinson, and R. Hall-Wilton. Statistical position reconstruction for rpc-based thermal neutron detectors. *Journal of Instrumentation*, 16(08):P08032, aug 2021.

[75] Jacopo Valsecchi, Ralph Harti, Marc Raventós, Muriel Siegwart, M. Morgano, Pierre Boillat, Markus Strobl, Patrick Hautle, Lothar Holitzner, Uwe Filges, Wolfgang Treimer, Florian Piegsa, and Christian Grünzweig. Visualization and quantification of inhomogeneous and anisotropic magnetic fields by polarized neutron grating interferometry. *Nature Communications*, 10:1–9, 08 2019.